Normal zone and resistive domain in thin-film superconducting bridges: nonlinearity effects

I. L. Maksimov and D. Yu. Vodolazov

Nizhniĭ Novgorod State University, Nizhniĭ Novgorod
(Submitted December 16, 1997; resubmitted May 7, 1998)
Pis'ma Zh. Tekh. Fiz. **24**, 1–8 (November 12, 1998)

An investigation was made of the propagation of a normal-state switching wave and the establishment of a resistive domain in thin-film superconducting bridges. It was observed that the nonlinearity of the current–voltage characteristic of the material, using the density of the superconducting condensate as the parameter, strongly influences the characteristics of dissipative structures. © *1998 American Institute of Physics.* [S1063-7850(98)00111-6]

A superconductor carrying a current greater than a certain critical level is in a metastable state with respect to fairly strong perturbations which lead to the formation and subsequent propagation of a normal zone.[1] In addition, a resistive (or normal) domain consisting of a localized dissipative structure may form in the superconductor.[1]

Studies of the existence conditions and characteristics of dissipative structures in thin-film high-temperature superconducting (HTSC) systems must take into account a specific feature of low-dimension superconductors. This shows up as significant nonlinearity of the current–voltage characteristic in high-temperature superconducting bridges[2] caused, for example, by the presence of the Berezinskiĭ–Kosterlitz–Thouless phase[2,3] in the system. In this case, the coefficient of nonlinearity is proportional to the density of the Berezinskiĭ–Kosterlitz–Thouless condensate.

Here we investigate the influence of the transport current on the propagation velocity of the switching wave in a high-temperature superconducting film, allowing for a nonlinear dependence $E(j)$. We examine the influence of the condensate density on the shape and dimensions of the normal and resistive domains and determine the current–voltage characteristic of a superconducting bridge containing a domain.

MODEL

The heat conduction equation for a superconducting bridge has the form

$$D_s C_s \frac{\partial T}{\partial t} = D_s \frac{\partial}{\partial x} k_s \frac{\partial T}{\partial x} + d_f Q(T) - W(T), \tag{1}$$

where D_s is the substrate thickness, C_s and k_s are the specific heat and thermal conductivity of the substrate material, d_f is the thickness of the HTSC film, and $W(T)$ is the heat transfer from the surface of the substrate to a coolant at temperature T_0:

$$W(T) = h(T - T_0); \tag{2}$$

$h = k_s / D_s$ is the effective coefficient of heat transfer.

The specific thermal power released in the film is $Q(T) = \rho(j,T) j^2$, where $\rho(j,T)$ is the effective resistivity:

$$\rho(j,T) = \begin{cases} \rho_n & T > T_c, \\ \rho_n \left(1 - \dfrac{j_c(T)}{j} \right)^{a(T)} & T_r < T < T_c, \\ 0 & T < T_r, \end{cases} \tag{3}$$

ρ_n is the normal-state resistivity of the superconductor, j is the current density, T_c is the critical temperature of the superconductor, and T_r is the temperature of the transition to the resistive state, which is determined from the condition $j_c(T_r) = j$. The coefficient for the nonlinearity of the current–voltage characteristic is expressed in the form $a(T) = K(T_c/T - 1)$, where K is the parameter of the Berezinskiĭ–Kosterlitz–Thouless condensate. For simplicity we shall assume that the temperature dependence of the critical current density caused by bulk vortex pinning is linear:

$$j_c(T) = j_{c0} \left(1 - \frac{T}{T_c} \right). \tag{4}$$

The phenomenological parameter $K = \varepsilon_0 d / (k_B T_c)$ is expressed in terms of the vortex energy $\varepsilon_0 d$ in a layer of thickness d, where $\varepsilon_0 = \Phi_0^2 / (16 \pi^2 \lambda(0)^2)$ is a quantity proportional to the density of the superconducting condensate at zero temperature (Φ_0 is the magnetic flux quantum and $\lambda(0)$ is the London penetration depth at $T = 0$). An estimate of K for the typical layered HTSC material BiSCCO ($d \approx 15$ Å, $\varepsilon_0 d \approx 3000\ \mathrm{K} = 0.25\ \mathrm{eV}$, $T_c = 80\ \mathrm{K}$) gives a value of order 30 (Ref. 4). It is difficult to estimate K for weakly anisotropic materials such as YBaCuO because the thickness of the current-carrying layer d is unknown.

The equilibrium states of the system are described by the balance equation for the released and transferred heat:[1,2]

$$Q^*(T) = W(T),$$

where $Q^*(T) = d_f Q(T)$ is the heat release per unit area. This equation in the approximation (3) has three roots which correspond to three equilibrium positions, two stable and one unstable. The stable states are those for which $\partial W / \partial T > \partial Q / \partial T$.

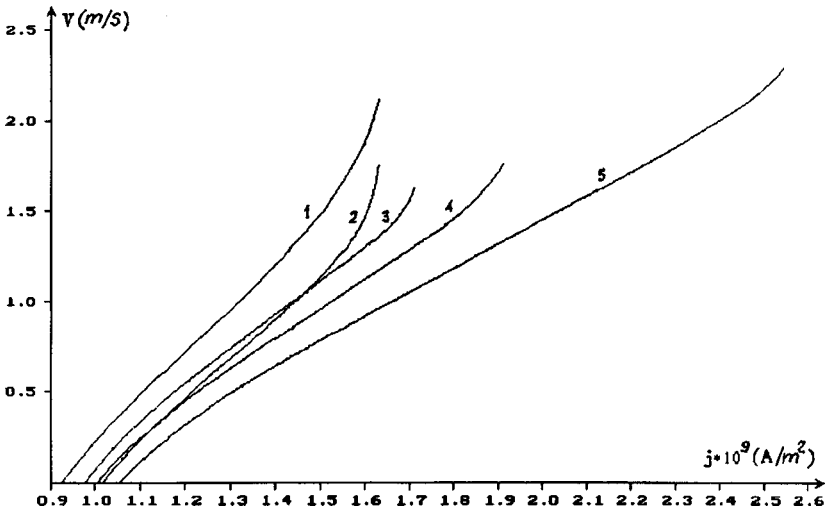

FIG. 1. Propagation velocity of switching wave versus current for various values of the parameter K: *1* — $K=5$; *2* — $a=1$; *3* — $K=10$; *4* — $K=15$; *5* — $K=30$.

Below we present the main results obtained from numerical analysis of Eq. (1) with conditions (2)–(4). In the calculations we used the following values of the superconductor and substrate parameters:

$$C_s=1\times10^5\ \mathrm{J/(m^3\cdot K)},\quad k_s=340\ \mathrm{W/(m\cdot K)},$$

$$d_f=10^{-7}\ \mathrm{m},$$

$$D_s=5\times10^{-4}\ \mathrm{m},\quad T_c=92\ \mathrm{K},$$

$$T_0=77\ \mathrm{K},\quad j_{c0}=10^{10}\ \mathrm{A/m^2}.$$

SWITCHING AUTOWAVES

We shall seek a solution of Eq. (1) in the form $T(x,t)=T(x-Vt)$ (switching autowave) with the boundary conditions $T(x=+\infty, t=0)=T_0$, $T(x=-\infty, t=0)=T_1$ (here T_0 and T_1 are the temperatures of the first and second stable equilibrium positions, respectively) and $\partial T/\partial x(x=\pm\infty, t=0)=0$, with the constraint that the heat fluxes are continuous at temperatures T_r and T_c.

Figure 1 gives the autowave propagation velocity as a function of the transport current (for various K and also for the case $a=1$ which corresponds to the linear current–voltage characteristic of hard superconductors[1] in the resistive region). It can be seen that as K increases, the range of currents within which a switching wave can propagate broadens appreciably. This situation arises because as K increases, the heat release near T_r becomes a weakly increasing function of temperature. As a result, the first equilibrium state characterized by the temperature $T=T^*(j,K)>T_0$ disappears at a higher current density $j_{\max}$. The establishment of a normal state at $j>j_{\max}$ is not described by the autowave regime.

Note that unlike the model with a stepwise heat release, $V_{\max}$ is finite and varies strongly as the parameter K varies. Figure 2 gives $V_{\max}$ as a function of K.

It can be seen from Fig. 2 that the dependence $V_{\max}(K)$ has a minimum for $K=K^*$. The calculations indicate that this occurs when $a(T_0)\approx1$ holds, which gives $K^*\approx T_0/(T_c-T_0)\approx5$ (for $T_0=77\ \mathrm{K}$ and $T_c=92\ \mathrm{K}$). In the range $K<K^*$ $V_{\max}$ increases abruptly and for $K\to0$ we find $V_{\max}\to\infty$. Mathematically, this is because for $K\to0$ our problem is equivalent to one with a stepwise heat release, for which an accurate solution exists, giving $V_{\max}\to\infty$ (Ref. 3). Note that typical values of $V_{\max}$ lie in the range $1\ \mathrm{m/s}<V_{\max}<20\ \mathrm{m/s}$ (for $1<K<K^*$).

Numerical analysis of the system (1)–(3) reveals the

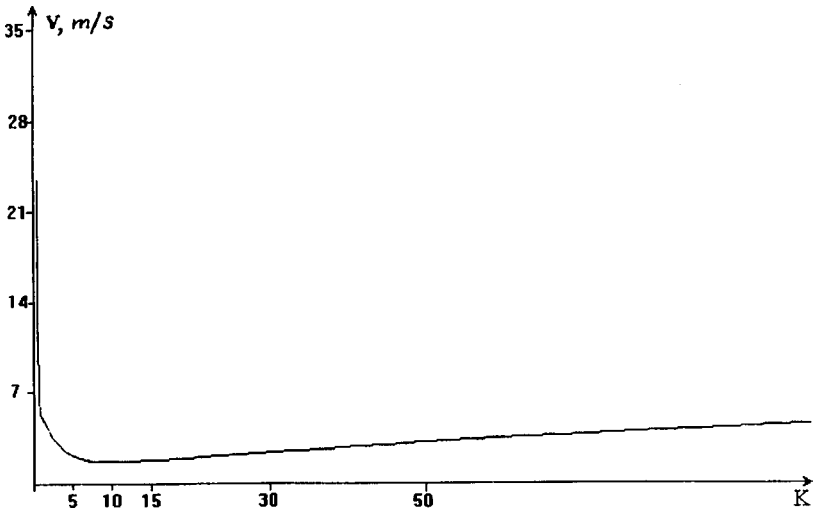

FIG. 2. Maximum propagation velocity $V_{\max}$ of switching wave versus parameter K.

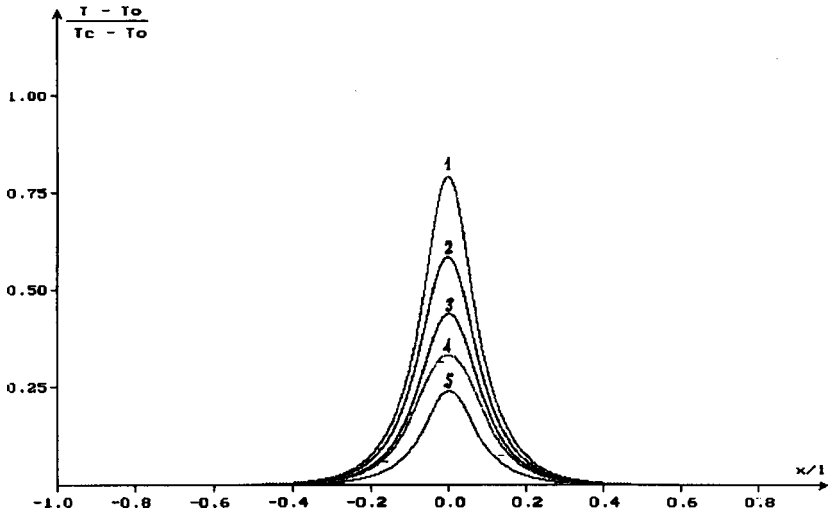

FIG. 3. Temperature distribution in sample with resistive domain for various values of K: *1* — $K=30$; *2* — $K=15$; *3* — $K=10$; *4* — $a=1$; *5* — $K=5$.

existence (for $K<K^*$) of a new type of switching wave, a superconducting state–resistive state (S–R) wave. For $K>50$ R–R' switching waves may also exist. We note that the possible appearance of R–S and R–R' waves is attributable to the strong temperature nonlinearity of the heat release, which allows $W(T)$ and $Q(T)$ to have a triple intersection even when $T<T_c$.

CURRENT–VOLTAGE CHARACTERISTIC OF A SUPERCONDUCTOR WITH A STEADY-STATE DOMAIN

In the steady-state case, after dropping the term containing the time derivative in Eq. (1), we can express this in the form of an ordinary first-order differential equation:[1]

$$\left(k_s\frac{dT}{dx}\right)^2=S(T), \tag{5}$$

where the integral

$$S(T)=\int_{T_{\min}}^{T}k_s\left[W(T')-\frac{d_f}{D_s}Q(T')\right]dT' \tag{6}$$

characterizes the degree of imbalance between the heat release and the heat transfer, $T_{\min}=\max(T_0,T^*)$. Equations (5) and (6) were derived assuming the boundary conditions $T(x=\pm\infty)=T_0$, $\partial T/\partial x(x=\pm\infty)=0$, which are satisfied if the finite dimensions of the sample are neglected.

Figure 3 gives the temperature distribution in the domain obtained resulting from numerical solution of Eq. (5) for various values of the parameter K and the same current.

The increase in the maximum domain temperature T_m with increasing coefficient of nonlinearity K is easily understood on the basis of the following reasoning. As K increases, the ''area rule'' $S(T_m)=0$ which determines T_m is satisfied at higher temperature. This can be attributed to the more gently sloping dependence $Q(T)$ for $K\geqslant K^*$. Note that for $K<K^*$ the shape of the domain is almost independent of K.

Since the domain is a dissipative structure (with finite resistivity), its presence is accompanied by the appearance of a voltage at the superconductor. The voltage drop at a superconductor with a domain is given by:[1]

$$U=\sqrt{2}\int_{T_r}^{T_c}\rho_n k_s j\left(1-\frac{j_c(T)}{j}\right)^{a(T)}\frac{dT}{\sqrt{S(T)}}+\rho_n j l, \tag{7}$$

where l is the size of the normal zone of the domain.

The results of numerical calculations of Eq. (7) for various K are plotted in Fig. 4. The kink clearly visible on the

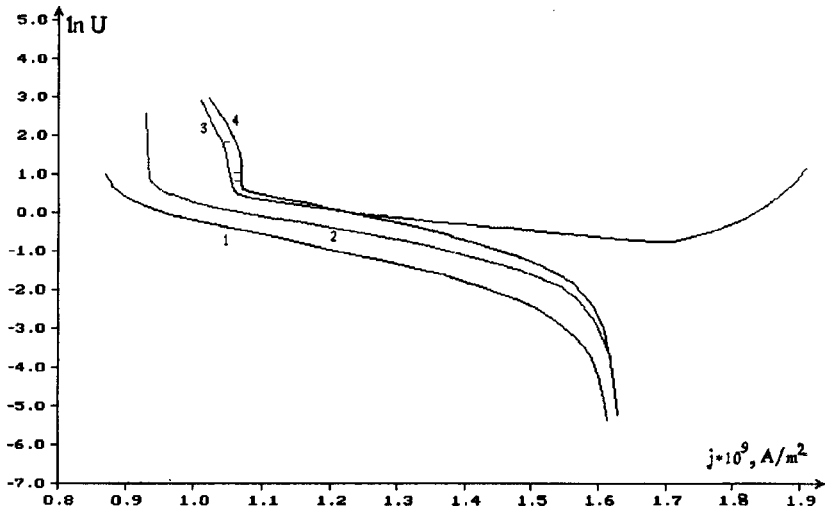

FIG. 4. Current–voltage characteristic of superconductor with domain for various values of K: *1* — $K=1$; *2* — $K=5$; *3* — $K=15$; *4* — $a=1$.

logarithmic scale corresponds to the appearance of a normal zone in the domain which is accompanied by an abrupt increase in voltage (note that this kink is not observed on curve *1*, since for $K \leqslant 1$ the domain has no normal zone over the entire range of currents).

For $K > K^*$ the current–voltage characteristic typically exhibits a section with a positive differential resistance. This occurs because above the current j^* ($j^* = j_c(T_0)$) the entire superconductor goes over to the resistive state with the temperature $T^*(j,K) > T_0$, on which the domain will be superposed. As the current increases further, the size of the domain decreases but T^* increases. As a result U will increase, since for $j > j^*$ the voltage drop will be mainly attributable to the resistive region of the superconducting bridge. We emphasize that the appearance of a section with a positively sloping current–voltage characteristic is unrelated to the bounded length of the superconducting bridge.[1,6]

This work was supported by the Ministry of Science of the Russian Federation (Project No. 95–057), State Education of the Russian Federation (Grant No. 95–0–7.3–178), and also by the International Center for Potentially Useful Research (Nizhniĭ Novgorod, Grant No. 97–2–10).

[1] A. V. Gurevich and R. G. Mints, *Thermal Autowaves in Normal Metals and Superconductors* [in Russian], IVTAN, Moscow (1987), 168 pp.
[2] A. Sh. Fix, I. L. Maksimov, K. V. Morozov, and V. V. Osipov, IEEE Trans. Appl. Supercond. **3**, 168 (1993).
[3] P. Minnhagen, Rev. Mod. Phys. **59**, 1001 (1987).
[4] G. Blatter, M. V. Feigel'baum, V. B. Geshkenbein *et al.*, Rev. Mod. Phys. **66**, 1125 (1994).
[5] M. O. Lutset and S. V. Klimov, Sverkhprovodimost' KIAE **7**, 1372 (1994).
[6] V. N. Skokov and V. P. Koverda, Sverkhprovodimost' KIAE **6**, 1646 (1993).

Translated by R. M. Durham

Acceleration of Brownian particle diffusion parallel to a fast random field with a short spatial period

A. N. Malakhov

Nizhniĭ Novgorod State University
(Submitted April 21, 1998)
Pis'ma Zh. Tekh. Fiz. **24**, 9–15 (November 12, 1998)

It is shown that a spatially periodic random field fluctuating rapidly near zero with a fairly small spatial period may substantially accelerate the diffusion of Brownian particles parallel to this field. [S1063-7850(98)00211-0]

The diffusive spreading of the mean square of the coordinate $x(t)$ of a Brownian particle $\langle x^2\rangle = 2Dt$ undergoing free diffusion in a viscous medium parallel to the x axis with zero initial conditions is well-known. The diffusion coefficient D determines the temporal rate of spreading of a Gaussian probability density $W(x,t)$ with zero average and variance $\langle x^2\rangle$. The corresponding Langevin equation has the form $dx(t)/dt = \xi(t)$, where $\xi(t)$ is stationary Gaussian white noise with $\langle \xi(t)\rangle = 0$ and $\langle \xi(t)\xi(t+\tau)\rangle = 2D\delta(\tau)$.

The diffusion coefficient $D = kT/h$, where k is the Boltzmann constant, is determined by the equivalent temperature T and viscosity h of the medium.

Let us now assume that the spreading of Brownian particles from the initial distribution $W(x,0) = \delta(x)$ takes place in this medium under the action of additional forces attributable to the random potential field $\Phi(x)\zeta(t)$, where $\zeta(t)$ is a dimensionless Gaussian delta-correlated process with $\langle \zeta(t)\rangle = 0$, $\langle \zeta(t)\zeta(t+\tau)\rangle = 2D_\zeta \delta(\tau)$, which is statistically independent of the thermal noise $\xi(t)$. In this case we can write the Langevin equation as

$$\frac{dx(t)}{dt} = -\frac{d\Phi(x)}{h dx}\zeta(t) + \xi(t) = -D\frac{d\varphi(x)}{dx}\zeta(t) + \xi(t), \tag{1}$$

where we introduce the dimensionless potential profile $\varphi(x) = \Phi(x)/kT$. We note that the random process $x(t)$ is a continuous Markov process.

The Fokker–Planck equation for $W(x,t)$ has the standard form (see, e.g., Ref. 1):

$$\frac{\partial W(x,t)}{\partial t} = \frac{\partial}{\partial x}[K_1(x,t)W(x,t)] + \frac{1}{2}\frac{\partial^2}{\partial x^2}[K_2(x,t)W(x,t)], \tag{2}$$

where $K_1(x,t)$ and $K_2(x,t)$ are the drift and diffusion coefficients which can be found from the Langevin equation.

The general evolution equations for the first two moments of the continuous Markov random process $x(t)$ have the form (Ref. 2, § 10.6)

$$\frac{d\langle x\rangle}{dt} = \langle K_1(x,t)\rangle, \quad \frac{d\langle x^2\rangle}{dt} = 2\langle xK_1(x,t)\rangle + \langle K_2(x,t)\rangle, \tag{3}$$

where statistical averaging is performed over the probability density $W(x,t)$ determined by the Fokker–Planck equation (2).

We can easily find (see Ref. 1 and Ref. 2, p. 367) the following values of the drift and diffusion coefficients corresponding to the Langevin equation (1):

$$K_1(x) = \frac{D^2 D_\zeta}{2l^2}\frac{d}{dx}\psi^2(x), \quad K_2(x) = 2D\left[1 + \frac{DD_\zeta}{l^2}\psi^2(x)\right]. \tag{4}$$

Here we introduce the dimensionless function $\psi(x) = l d\varphi(x)/dx$, where l is some scale. Thus, for an arbitrary profile $\varphi(x)$ the evolution equations for the moments have the form

$$\frac{d\langle x\rangle}{dt} = \frac{D^2 D_\zeta}{2l^2}\left\langle \frac{d}{dx}\varphi^2(x)\right\rangle,$$

$$\frac{d\langle x^2\rangle}{dt} = \frac{D^2 D_\zeta}{l^2}\left\langle x\frac{d\varphi^2(x)}{dx}\right\rangle + 2D\left[1 + \frac{DD_\zeta}{l^2}\langle \varphi^2(x)\rangle\right]. \tag{5}$$

If the potential function $\varphi(x)$ is even, by virtue of the symmetry of the situation, the probability density is also an even function $W(-x,t) = W(x,t)$. In this case, we find $K_1(x) = 0$ (and therefore $\langle x\rangle \equiv 0$) and only the second equation (5) for the mean square of the Brownian particle coordinates remains.

As a first example, consider the even sawtooth potential profile $\varphi(x)$ with the spatial period l shown in Fig. 1. We can easily see that $\varphi(x) = 2bx/l$ holds for $0 \leqslant x \leqslant l/2$ and find $\psi^2(x) = 4b^2$ for all x.

We therefore obtain $K_2(x) = 2D[1 + 4DD_\zeta(b/l)^2]$. Thus, for zero initial conditions the spreading law for the mean square of the coordinate of Brownian particles has the diffusion form $\langle x^2\rangle = 2D_{\text{eff}}t$, where the effective diffusion coefficient is given by

$$D_{\text{eff}} = D\left[1 + 4DD_\zeta\left(\frac{b}{l}\right)^2\right] > D. \tag{6}$$

We note that this result is exact. If there is no fluctuating field ($D_\zeta = 0$), we arrive at $D_{\text{eff}} = D$, as should be the case.

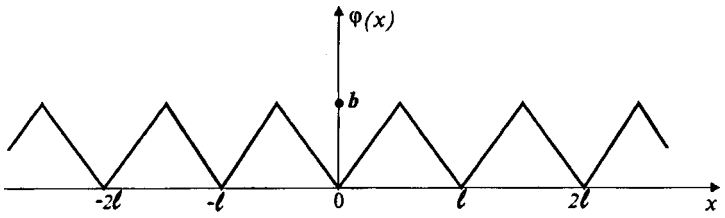

FIG. 1. Sawtooth potential profile.

We also note that for a sawtooth field, as for free diffusion, $W(x,t)$ is a strictly Gaussian probability density.

Thus, a periodic, sawtooth, rapidly fluctuating random field acting on Brownian particles accelerates their diffusion and this acceleration increases with increasing b/l, i.e., with increasing absolute value of the field slope per period.

Since this potential profile $\varphi(x)$ is even and the diffusion is symmetric in both directions, the probability flux at the point $x=0$ is zero and so a reflecting boundary can be sited at this point and diffusion from the reflecting boundary can be considered only in the direction of positive x. The result (6) remains unchanged. From this it follows that diffusion can be accelerated in one direction (away from the reflecting boundary).

Let us now discuss the physical mechanism for the acceleration of diffusion, confining our analysis to the motion of Brownian particles over a single period of the field in the direction of increasing x. For simplicity we shall give the field profile for two cases: $\zeta=+1$ and $\zeta=-1$ (Fig. 2a).

If $\zeta=+1$ holds, the particles diffuse up the slope and this motion is slower than that along the horizontal axis. We shall estimate this time with an absorbing boundary (a potential going vertically downward) situated at the point $l/2$. In this case, the Brownian particles should overcome a potential barrier of height b. It can be shown that the time taken to overcome the barrier (see Ref. 3, for instance), i.e., the time taken for the particles to move up the slope by the distance $l/2$ is

$$T_{\mathrm{up}}=\frac{l^2}{4Db^2}(e^b-1-b). \tag{7}$$

For $\zeta=-1$ the particles diffuse down the slope and the time taken for them to cover the distance $l/2$ is

$$T_{\mathrm{down}}=\frac{l^2}{4Db^2}(e^{-b}-1+b)<T_{\mathrm{up}}. \tag{8}$$

It follows from these formulas that for $b=0.5$ the diffusion velocity of the Brownian particles down the slope is 1.5 times higher than the upward diffusion velocity, for $b=2$ the downward diffusion velocity is almost four times higher, and for $b\leqslant 4$ the velocity ratio is $e^b/b\gg 1$.

Since the average of the random function $\zeta(t)$ is zero, its sign varies continuously and the particles move up the slope half the time and downward half the time. The difference in the velocities has the result that the particles cover most of the path between $x=0$ and $x=l/2$ in the ''downsloping'' state and this proportion increases with increasing b/l. The motion of the Brownian particles between $l/2$ and l is exactly the same, the only difference being that they now move down the slope for $\zeta(t)>0$ and up the slope for $\zeta(t)<0$.

Thus, the changes in the sign of $\zeta(t)$ make it possible for the Brownian particles to cover most of the path in the downsloping state (Fig. 2b) and they therefore move faster along the x axis than under free diffusion, which accelerates the diffusion process in accordance with the effective diffusion coefficient (6).

Let us now consider a second example, a harmonic even field $\varphi(x)=b\cos(2\pi x/l)/$ with the same period l. In this case, we have $\varphi^2(x)=4\pi^2b^2\sin^2(2\pi x/l)$. However, the second equation (5) cannot be solved accurately because $W(x,t)$ is non-Gaussian. Using a Gaussian approximation for $W(x,t)$ with zero average and unknown variance, we can obtain the following nonlinear equation for $\langle x^2\rangle$ from the second equation (5):

$$\frac{d\langle x^2\rangle}{dt}=4D^2D_\zeta\left(\frac{b}{l}\right)^2 a\langle x^2\rangle\exp(-a\langle x^2\rangle)+2D \times\left\{1+2\pi^2DD_\zeta\left(\frac{b}{l}\right)^2[1-\exp(-a\langle x^2\rangle)]\right\}, \tag{9}$$

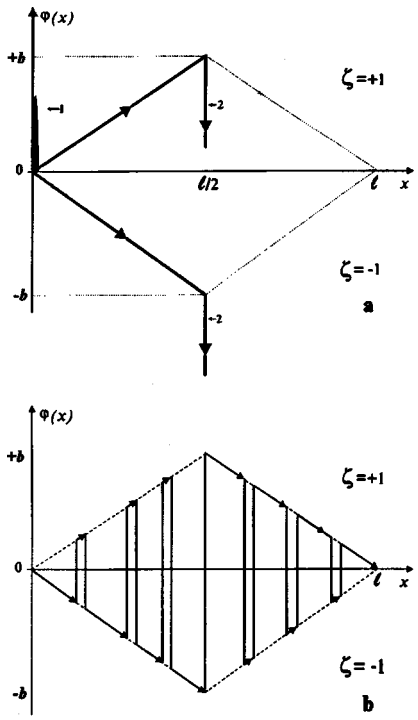

FIG. 2. Diffusion of Brownian particles from the initial probability distribution: a — slow motion up the slope and fast motion down the slope: *1* — initial distribution, *2* — absorbing boundaries; b — general motion of Brownian particles over a field period.

where $a=8\pi^2/l^2$. An analysis of this nonlinear equation shows that for times such that $\langle x^2\rangle^{1/2}$ exceeds the half-period of the field ($a\langle x^2\rangle \gg 1$) we have

$$\langle x^2\rangle = 2D_{\text{eff}}\, t, \quad D_{\text{eff}} = D\left[1+2\pi^2 D D_\zeta \left(\frac{b}{l}\right)^2\right]. \qquad (10)$$

Thus, for a cosinusoidal fluctuating field this approximate effective diffusion coefficient has the same order of magnitude as that for the sawtooth field (6), maintaining an acceleration of the diffusion which increases with increasing b/l.

Analysis shows that the diffusion acceleration effect described above is not related to the sawtooth or cosinusoidal profile of the field fluctuating rapidly about zero. The effect will evidently occur for any periodic or aperiodic field consisting of fairly steep up- and downsloping elements of arbitrary profile.

The so-called molecular motor mechanism or stochastic ratchet has recently been studied intensively (see Refs. 4–8 and the literature cited therein). This effect essentially involves the existence of a directional diffusion flux of Brownian particles caused by the formation of asymmetric diffusion conditions as a result of some type of modulation of a periodic (asymmetric) field at a frequency determined by the diffusion time on scales of the field period. The proposed diffusion acceleration effect is merely externally similar to the molecular motor effect. The difference is that a general directional transfer of material is observed in the case of a molecular motor whereas in our case, the effective coefficient of ''ordinary'' diffusion increases as a result of fast modulation of the field, which is unrelated to the temporal characteristics of the spreading of the probability density on scales of the field period.

This work was supported by the Russian Fund for Fundamental Research (Grants Nos. 96–02–16772-a and 96–15–96718).

[1] H. Risken, *The Fokker-Planck Equation* (Springer-Verlag, Berlin 1989), 472 pp.
[2] A. N. Malakhov, *Cumulative Analysis of Random Non-Gaussian Processes and Their Transformations* [in Russian], Sovetskoe Radio, Moscow (1978), 376 pp.
[3] N. V. Agudov and A. N. Malakhov, Izv. Vyssh. Uchebn. Zaved. Radiofiz. **36**(2), 148 (1993).
[4] A. P. Nikitin and D. É. Postnov, Pis'ma Zh. Tekh. Fiz. **24**(2), 47 (1998) [Tech. Phys. Lett. **24**, 61 (1998)].
[5] D. É. Postnov, A. P. Nikitin, and V. S. Anishchenko, Pis'ma Zh. Tekh. Fiz. **22**(9), 24 (1996) [Tech. Phys. Lett. **22**, 352 (1996)].
[6] M. Bier and R. D. Astumian, Phys. Rev. Lett. **76**, 4277 (1996).
[7] M. Bier, Phys. Lett. **211**, 12 (1996).
[8] J. Luczka, R. Bartussek, and P. Hänggi, Europhys. Lett. **31**, 431 (1995).

Translated by R. M. Durham

Relation between the domain dynamics and the shape of the cathode ''notch'' in a Gunn diode

A. I. Mikhaĭlov and D. M. Lerner

N. G. Chernyshevskiĭ State University, Saratov
(Submitted September 1, 1997; resubmitted March 16, 1998)
Pis'ma Zh. Tekh. Fiz. **24**, 16–22 (November 12, 1998)

Results are presented of a mathematical modeling of the influence of the shape of the cathode ''notch'' in the semiconductor structure of a Gunn diode on the characteristics of the domain dynamics. It is shown that processes whereby the domain escapes from the notch into the active region and its leading edge approaches the highly doped region near the anode play a major role in the formation of the second harmonic component in the spectrum of the Gunn diode current. © *1998 American Institute of Physics.* [S1063-7850(98)00311-5]

At present, the maximum frequencies of Gunn oscillators with *n*-type gallium arsenide (*n*-GaAs) diodes operated at the fundamental drift frequency do not exceed 60–70 GHz. Experience gained in recent years suggests that the most preferable method of increasing the operating frequency of Gunn diode oscillators involves separating the power into harmonics of the fundamental frequency.[1,2] The characteristic s of the domain formation process, the dynamics of its propagation through the active region and drift to the anode, and ultimately the profile of the Gunn diode current depend to a considerable extent on the doping profile of the semiconductor structure. This dependence shows up particularly strongly in diodes with short (less than 5 μm) active regions where the times taken for formation of the domain and its drift to the anode become comparable with the period of the drift oscillations.

The characteristics of Gunn diodes and oscillators have been investigated as a function of the doping profile in various studies.[3–10] Most of these were concerned with oscillators operating at the fundamental frequency. The influence of the doping profile on the operation of harmonic oscillators was only examined in a few cases,[6–10] and this aspect cannot be considered to be sufficiently well studied.

Here we use mathematical modeling to investigate the relationship between the carrier dynamics in the semiconductor structure of a Gunn diode and the shape of the cathode ''notch,'' a narrow region near the cathode where the doping level is lower than the active region. The doping profile $N_D(x)$ of the semiconducting structure of an $n^+-n^--n-n^+$-GaAs Gunn diode (where n^- is the notch) shown schematically in Fig. 1a was approximated by a piecewise linear function. The donor density in the highly doped cathode and anode n^+ regions was 2×10^{16} cm^{-3} and that in the active *n*-region was 3.6×10^{15} cm^{-3}. The doping level in the notch N_N (the notch depth) was varied between 10^{15} and 2.6×10^{15} cm^{-3} in the calculations and the notch width W was varied between 0.1 and 1.5 μm. These ranges of variation of the width and doping level in the notch were selected to ensure that stable drift oscillations were always achieved. The sum of the length of the active *n*-region and the notch width was 3 μm in all the calculations and the total length of the entire semiconductor structure L was 5 μm. The dc voltage U_0 was chosen as 4 V. In order to eliminate the influence of the external circuit and also to simplify the calculations, we used a regime which shorted the ac signal, i.e., the voltage on the diode was assumed to be constant and equal to U_0.

The calculations were based on the local field model in which, for the one-dimensional case, the electron dynamics in the semiconductor structure are described by the equation of continuity, the Poisson equation, and the total current equation:

$$q\partial n(x,t)/\partial t = -\partial j_k(x,t)/\partial x, \tag{1}$$

$$\partial E(x,t)/\partial x = q[n(x,t)-N_D(x)]/\varepsilon\varepsilon_0, \tag{2}$$

$$j(t) = j_k(x,t)+\varepsilon\varepsilon_0\partial E(x,t)/\partial t, \tag{3}$$

where $j_k(x,t)=qn(x,t)v(E(x,t))-qD\partial n(x,t)/\partial x$ is the convection current density, $n(x,t)$ and q are the electron density and the absolute value of the electron charge, ε_0 is the dielectric constant, and x and t are thespatial coordinate and the time. The relative permittivity of GaAs is $\varepsilon=12.5$. The electron drift velocity $v(E(x,t))$ was assumed to be a local and instantaneous function of the electric field $E=E(x,t)$ and was given by the analytic expression

$$v(E)=[\mu_a E+v_a(E/E_a)^4]/[1+(E/E_a)^4], \tag{4}$$

where $\mu_a=9000$ cm^2/V·s, $v_a=0.8\times10^7$ cm/s, and $E_a=3.8$ kV/cm are the parameters of the approximation of $\nu(E)$ at 300 K. The diffusion coefficient D was assumed to be constant, 300 cm^2/s.

The model equations were approximated using finite-difference schemes and were solved numerically under the following boundary and initial conditions:

$$n(0,t)=N_D(0), \quad n(L,t)=N_D(L), \quad \int_0^L E(x,t)dx=U_0,$$

$$n(x,0)=N_D(x), \quad E(x,0)=U_0/L. \tag{5}$$

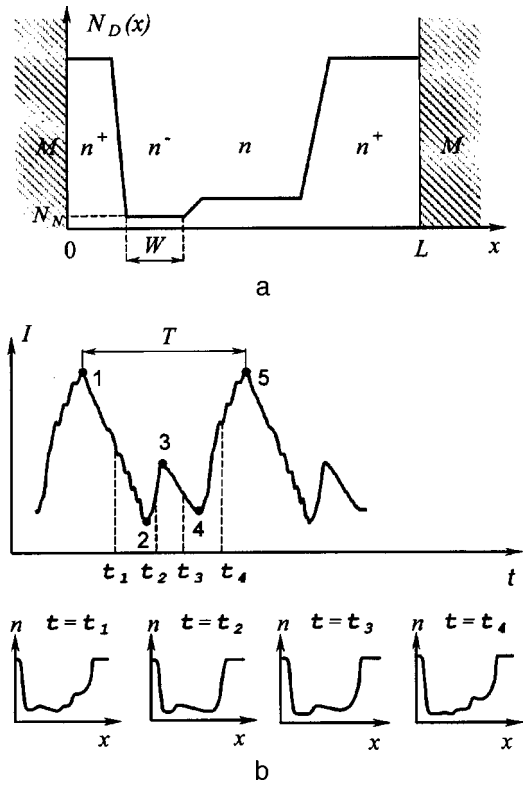

FIG. 1. a — Doping profile $N_D(x)$ of semiconductor structure in Gunn diode; b — current I versus time t and distribution of electron density $n(x)$ in semiconductor structure of Gunn diode at times $t=t_1$, t_2, t_3, and t_4.

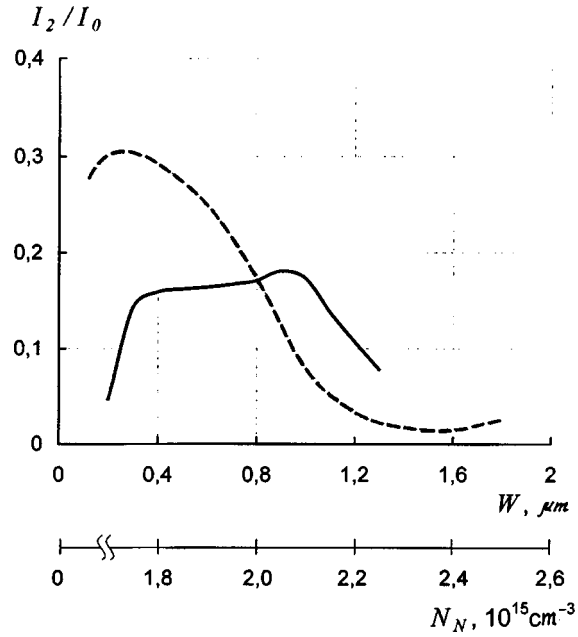

FIG. 2. Relative amplitude of the second harmonic component of the current I_2/I_0 as a function of the notch width W and depth N_N: solid curve — I_2/I_0 versus W for $N_N=2\times10^{15}$ cm^{-3}; dashed curve — I_2/I_0 versus N_N for $W=1$ μm.

The first two conditions model the contacts between the highly doped n^+ regions and the metal contacts of the structure and in fact imply that the layers of the n^+ regions in contact with the metals, directly adjacent to the metals, are neutral and have no space charge.

The problem was solved for a given voltage U_0. The timestep and mesh spacing were selected to give a mathematically stable solution and were smaller than the corresponding characteristic quantities, the Maxwellian relaxation time and the Debye length. The results of the modeling are plotted in Figs. 1 and 2.

Figure 1b gives the profile of the current I and the distribution of the electron density $n=n(x,t)$ over the structure of the Gunn diode at various times t during a single period of the drift oscillations T obtained for a notch depth of 2×10^{15} cm^{-3} and width 1 μm. Analysis of the domain dynamics and the profile of the Gunn diode currents reveals that the following main processes can be identified in the semiconductor structureof the Gunn diode during a single period of the oscillations:

a) a domain forms at the notch, i.e., the current decreases (section 1–2 on the time dependence of the current);

b) the electron-enriched rear part of the domain escapes from the notch into the active region with an enhanced donor density; in this case, the velocity of the heavy electrons increases since the electric field in the active region is lower than that in the notch and thus the current increases (section 2–3);

c) as the front electron-depleted part of the domain approaches the highly doped n^+ region near the anode, the field in the Gunn diode structure becomes redistributed and increases in the active n-region, which ultimately causes a drop in the current (section 3–4);

d) as the electron-enriched part of the domain drifts into the highly doped n^+ region near the anode, the current increases to a principal maximum (section 4–5).

All these processes are then repeated. Analysis revealed that the formation of the second harmonic component of the current was directly related to the dynamic processes in the Gunn diode structure which are responsible for the appearance of a local maximum in section 2–3–4 of the $I(t)$ curve i.e., escape of the domain from the notch and the beginning of the drift of its leading edge into the anode. Figure 2 gives the relative amplitude of the second harmonic component of the Gunn diode current as a function of the width (solid curve) and depth (dashed curve) of the cathode notch. The reasoning put forward above indicates that when the depth of the notch is small and thus there is little difference between the field in the notch and in the active region, the velocity of the heavy electrons in the rear enriched part of the domain increases less on entering the active region compared with when the depth is large. Thus, the amplitude of the second harmonic caused by escape of the domain into the active region increases as the notch depth increases. At large depths the amplitude of the second harmonic decreases since a transition takes place to a regime with a static domain at the cathode and the drift oscillations cease.

As the notch width varies, the difference between the field in the notch and that in the active region varies slightly. However, as the width decreases, a transition is observed to a regime with a static domain at the anode and consequently, the amplitude of the second harmonic decreases. As the

notch width increases, a time may arise when the domain length and the length of the active region become approximately the same and the process of escape of the enriched part of the domain from the notch may take place almost simultaneously with the onset of the drift of its leading edge into the anode. The coincidence of these two processes in time leads to a reduction in the amplitude of the second harmonic. The modeling showed that for semiconductor structures with the selected dimensions and doping, the maximum relative amplitude of the second harmonic is observed when the notch width is approximately half the length of the active region.

Thus, the optimum notch profile for Gunn diodes used in oscillators emitting at the second harmonic should be selected with allowance for at least the following two points. First, the notch should be deep enough to produce the largest possible electric field drop on transition from the notch to the active region. However, the depth should not be so large that a transition takes place to a regime where a static domain is established at the cathode. Second, the notch width should not be so small so that no transition takes place to a regime with a static domain at the cathode; but it should also be no more than half the length of the active region of the Gunn diode, because if it is greater than this the drift of the depleted part of the domain into the anode and the escape of its enriched part into the active region may take place simultaneously.

[1] N. A. Vasil'ev, V. S. Lukash, V. V. Murav' ev *et al.*, Izv. Vyssh. Uchebn. Zaved. Radioélektron. **28**(10), 42 (1985).
[2] A. S. Kosov and V. G. Elenskiĭ, Zarub. Radioélektron. No. 2, 54 (1987).
[3] Ş. B. Poresh, A. S. Tager, and A. A. Kal'fa, Élektron. Tekh. Ser. 1, Élektron. SVCh **10**, 19 (1976).
[4] A. A. Kal'fa, S. N. Konoplyannikov, S. B. Poresh, and A. S. Tager, Fiz. Tekh. Poluprovodn. **15**, 1359 (1981) [Sov. Phys. Semicond. **15**, 784 (1981)].
[5] Yu. V. Arkusha, A. M. Popov, and É. D. Prokhorov, Radiotekh. Elektron. **35**, 1552 (1990).
[6] J. Ondria and R. I. Ross, in *Gathering World Through Microwaves, Proceedings of the SBMO International Microwave Symposium*, Rio de Janeiro, 1987, Vol. 1 (San Paulo, 1987), p. 173.
[7] A. I. Mikhaĭlov and V. B. Panfilov, in *Interaction of Electromagnetic Waves with Solids, Proceedings of the Third All-Union School-Seminar*, Saratov [in Russian], Saratov University Press, Saratov (1991), p. 132.
[8] A. I. Mikhaĭlov, and V. B. Panfilov, in *Abstracts of the Seminar ''Nonlinear High-Frequency Phenomena in Semiconductors and Semiconducting Structures and Problems of Using Them in Microwave Electronics''*, Navoi, 1991, p. 52 [in Russian].
[9] A. I. Mikhaĭlov and V. B. Panfilov, Izv. Vyssh. Uchebn. Zaved. Radioélektron. **35**(1), 76 (1992).
[10] N. A. Zubovich and Yu. A. Tsvirko, Élektron. Tekh. Ser. 1, Élektron. SVCh. **1**, 31 (1990).

Translated by R. M. Durham

Influence of the size effect on the permittivity of potassium tantalate forming part of a film capacitor

S. P. Zubko

St. Petersburg State Electrotechnical University
(Submitted April 20, 1998)
Pis'ma Zh. Tekh. Fiz. **24**, 23–29 (November 12, 1998)

Calculations are made of the parameters of a phenomenological model of the permittivity of bulk and film samples of potassium tantalate as a function of the applied field and temperature. The correlation parameter needed to allow for the influence of the size effect is also calculated. Good agreement is obtained between the theoretical calculations and the experimental results. © *1998 American Institute of Physics.* [S1063-7850(98)00411-X]

INTRODUCTION

Many experimental studies of the virtual ferroelectric potassium tantalate $KTaO_3$ have appeared quite recently.[1–4] This material has lower microwave losses than the widely used strontium titanate $SrTiO_3$, which has been modeled fairly accurately. However, no reliable model description has yet been obtained for single-crystal or thin-film potassium tantalate. When the thickness of a ferroelectric film is comparable with its correlation radius, the permittivity of the film is a function of its thickness. This phenomenon is described as the size effect and is a consequence of the correlation of the ferroelectric polarization.

The aim of the present study is to develop mathematical models for a reliable description of the permittivity of potassium tantalate films forming part of a film capacitor, allowing for the influence of the size effect.

1. PERMITTIVITY OF THIN-FILM $KTaO_3$ SAMPLES. SIZE EFFECT

The dependence of the permittivity on the applied electric field and temperature is modeled using the Ginzburg–Devonshire equation[5,6] for the ferroelectric polarization obtained from a series expansion of the free energy.

A modified form of the fundamental differential equation for the ferroelectric polarization is[7]

$$-2\lambda_1 \frac{d^2P(x)}{dx^2} + \frac{D(x)}{\varepsilon(T)} + \frac{D^3(x)}{D_N^2} = \varepsilon_0 E(x). \tag{1}$$

The boundary conditions for metal electrodes are

$$P(x)|_{x=\pm h/2} = 0, \tag{2}$$

where h is the thickness of the ferroelectric field.

After solving Eq. (1) with the boundary conditions (2) (the solution of this equation and the derivation of the formula for ε_{eff} are given in Refs. 8–10, which also refer to previous studies), we obtain an expression for the permittivity allowing for correlation effects:

$$\varepsilon_{\text{eff}} = \varepsilon_{00}\{[(\xi^2+\eta^3)^{1/2}+\xi]^{2/3} + [(\xi^2+\eta^3)^{1/2}-\xi]^{2/3} - \eta + a^2\}^{-1}, \tag{3}$$

$$\eta(T) = (\theta_F/4T_c)\sqrt{1+(4T/\theta_F)^2} - 1,$$

$$\xi(E) = \sqrt{\xi_S^2 + (E/E_N)^2},$$

$$a = \sqrt{\frac{2\varepsilon_{00}}{\alpha h}}, \quad \alpha = \frac{1}{2\lambda_1}, \tag{4}$$

where h is the thickness of the ferroelectric layer.

The function $\eta(T)$ is an approximation of the Debye integral and reflects the temperature dependence of ε_{eff}. The function $\xi(E)$ is introduced when averaging the ferroelectric polarization.

The values of the model parameters are given in Table I. Figure 1 illustrates the experimental and model dependence $\varepsilon_{\text{eff}}(E,T)$ of single-crystal potassium tantalate.[2]

The parameter a introduced in formula (3) describes the measure of influence of the size effect on the effective permittivity of the material. The size effect suppresses the permittivity of the material. Numerical values of the model parameters for the experimental data from Ref. 3 are given in Table I. It can be seen that the values of the parameters are similar for the bulk samples and the film samples except for the Curie–Weiss constant $C=\varepsilon_{00}T_c$. For the bulk sample we have $C=4.96\times10^4$ and for the film $C=13.26\times10^4$. For strontium titanate the Curie–Weiss constant for the single crystal and the film also differs.[8–10] Figure 2 gives the experimental points and theoretical dependence of the permittivity of the thin film (film thickness[3] $h=300$ nm) on the temperature and applied field. The error of the approximation calculated using the formula

$$\delta = \sqrt{\sum_{j=0}^{n}\sum_{i=0}^{m}[(\varepsilon(T_j,E_i)-\varepsilon_{j,i})^2\,\varepsilon_{j,i}^{-2}]/nm},$$

where $\varepsilon_{j,i}$ are the experimental values of the permittivity, and $\varepsilon(T_j,E_i)$ are the calculated values for the same temperature and field, is $\delta=2\%$ for $U=0$ and $\delta=3.7\%$ for $U=2$ V. The theoretical curves were calculated using Eqs. (3) and (4) for the values of the parameters given in Table I.

TABLE I. Values of model parameters.

Sample	Parameters						
	T_c, K	θ_F, K	ε_{00}	ξ_S	E_N, kV/cm	a	$\delta\|_{E=0}$, %
Bulk (Ref. 2)	32.5	170	1390	0	15.6	–	3
Bulk (Ref. 11)	31.6	187	1706	0	–	–	7
Film (Ref. 3)	34	200	3900	3	16.5	7	2

2. CALCULATION OF THE CORRELATION PARAMETER λ_1

The numerical values of the correlation parameter λ_1 can be determined by analyzing the phonon spectra obtained by inelastic neutron scattering in the soft mode of a potassium tantalate crystal.

The dispersion equation for a cubic medium has the form[12,13]

$$\{[\omega_{0T}^2(0,T)-\omega^2+s_t](a_t k^2-\omega^2)-k^4 v_t^2\}^2$$
$$\times\{[\omega_{0L}^2(0,T)-\omega^2+s_L](a_L k^2-\omega^2)-k^4 v_L^2\}=0, \quad (5)$$

where

$$s_t=\frac{1}{A(T)}\lambda_3\omega_{0T}^2(0,T),$$

$$s_L=\frac{3\varepsilon_\infty(\varepsilon_s(T)-\varepsilon_\infty)}{\varepsilon_s(T)(\varepsilon_\infty+2)}\lambda_1\omega_{0L}^2(0,T),$$

$$v_t^2=\frac{1}{A(T)}\frac{\varepsilon_0}{\rho}\omega_{0T}^2(0,T)\theta_3^2,$$

$$v_L^2=\frac{3\varepsilon_\infty(\varepsilon_s(T)-\varepsilon_\infty)}{\varepsilon_s(T)(\varepsilon_\infty+2)}\frac{\varepsilon_0}{\rho}\omega_{0L}^2(0,T)\theta_1^2, \quad (6)$$

$$A(T)=(\varepsilon_\infty+2)/3(\varepsilon_s(T)-\varepsilon_\infty), \quad (7)$$

ε_s and ε_∞ are the values of the permittivity corresponding to the frequencies $\omega\ll\omega_i$ and $\omega\gg\omega_i$, where ω_i is the natural frequency of the ionic component of the polarization. For $KTaO_3$ we find $\varepsilon_\infty\cong 30$; s_t is a parameter having the dimensions of velocity, which for $KaTO_3$ is $s_t=(4.5\pm 0.3)\times 10^{11}\,\mathrm{cm}^2/\mathrm{s}^2$ (Ref. 13).

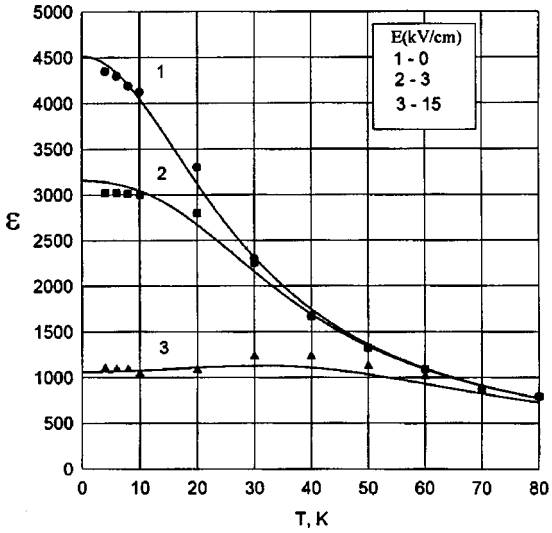

FIG. 1. Temperature dependence of the permittivity of single-crystal $KTaO_3$ for various values of the applied field E, and experimental points from Ref. 2.

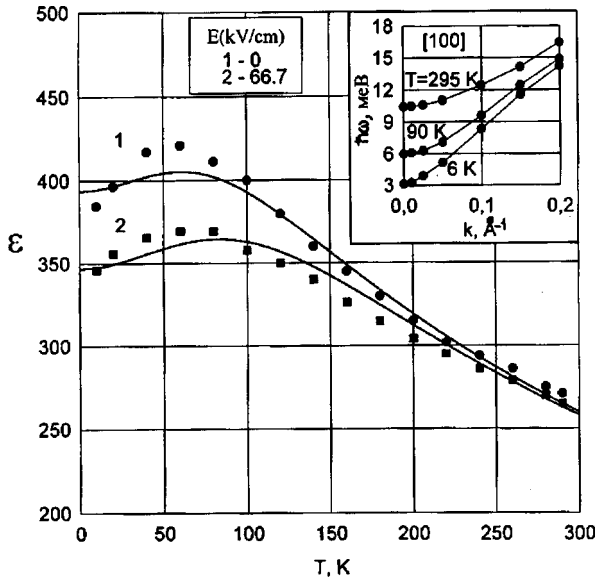

FIG. 2. Temperature dependence of the permittivity of thin-film $KTaO_3$ for various values of the applied field E, and experimental points from Ref. 3. Inset: dependence of the frequency of the transverse optical mode on the wave vector[14] at various temperatures.

By solving Eq. (5), we obtain transverse mode equations for the three directions of the wave vector:[13]

$$k[100]:\ \frac{\omega^2(k,T)}{\omega_{0T}^2(0,T)}=1+\frac{\lambda_3 k^2}{A(T)};$$

$$k[110]:\ \frac{\omega^2(k,T)}{\omega_{0T}^2(0,T)}=1+\frac{\lambda_1-\lambda_2}{2A(T)}k^2;$$

$$k[111]:\ \frac{\omega^2(k,T)}{\omega_{0T}^2(0,T)}=1+\frac{\lambda_1-\lambda_2+\lambda_3}{3A(T)}k_2. \quad (8)$$

An analysis of the experimental data[14] on the frequency of the transverse optical mode as a function of the wave vector (inset to Fig. 2) and the temperature dependence of the permittivity of single-crystal potassium tantalate[2] using Eqs. (7) and (8) yields the following values of the parameters:

$$\lambda_1\cong 53.7\times 10^{-20}\,\mathrm{m}^2,\quad \lambda_2\cong 50.4\times 10^{-20}\,\mathrm{m}^2,$$

$$\lambda_3\cong 0.47\times 10^{-20}\,\mathrm{m}^2.$$

Since no data are available on the dispersion of the optical mode in the [110] and [111] directions, the values of λ_1 and λ_2 were estimated. Since potassium tantalate and strontium titanate belong to the same group of ferroelectrics their properties are similar, so it may be postulated that the depen-

dence of the transverse mode frequency on the wave vector for different directions of propagation should show the same behavior in $KTaO_3$ as in $SrTiO_3$.

Thus, the contribution of the size effect to the permittivity can be determined by two methods: by analyzing the dependence of the permittivity on the temperature and the controlling action (experimentally); or by calculating this, knowing the correlation parameter λ_1. The value of the parameter a calculated using Eq. (4) ($\lambda_1 \cong 53.7 \times 10^{-20}\,\mathrm{m}^2$ and $h = 300\,\mathrm{nm}$, $a = 5.2$), is similar to that obtained by minimizing the approximation error (see Table I).

CONCLUSIONS

To sum up, the significant difference between the permittivity of bulk[2,12] and film samples[3] of potassium tantalate is determined by the influence of the size effect when zero boundary conditions are satisfied for the ferroelectric polarization at the electrodes of a thin-film sandwich capacitor.

These quantitative characteristics can be used to model controlled potassium tantalate devices operating in the microwave range.

The author is grateful to Professor O. G. Vendik for assistance with the implementation and discussions of this work.

[1] G. V. Belokopytov, I. V. Ivanov, and I. Yu. Syromyatnikov, Fiz. Tverd. Tela (Leningrad) **32**, 1795 (1990) [Sov. Phys. Solid State **32**, 1045 (1990)].
[2] G. V. Belokopytov, Ferroelectrics **168**, 69 (1995).
[3] Yu. A. Boikov, Z. G. Ivanov, A. L. Vasiliev *et al.*, Appl. Phys. Lett. **67**, 2708 (1995).
[4] R. S. Klein, G. E. Kugel, and B. Hennion, J. Phys.: Condens. Matter **8**, 1109 (1996).
[5] V. L. Ginzburg, Zh. Éksp. Teor. Fiz. **19**, 36 (1949).
[6] A. F. Devonshire, Philos. Mag. **40**, 1040 (1949).
[7] O. G. Vendik and L. T. Ter-Martirosyan, Fiz. Tverd. Tela (St. Petersburg) **36**, 3343 (1994) [Phys. Solid State **36**, 1778 (1994)].
[8] O. G. Vendik and S. P. Zubko, Zh. Tekh. Fiz. **67**(3), 29 (1997) [Tech. Phys. **42**, 278 (1997)].
[9] O. G. Vendik, S. P. Zubko, and L. T. Ter-Martirosyan, Fiz. Tverd. Tela (St. Petersburg) **38**, 3654 (1996) [Phys. Solid State **38**, 1991 (1996)].
[10] O. G. Vendik and S. P. Zubko, J. Appl. Phys. **82**, 4475 (1997).
[11] W. R. Abel, Phys. Rev. B **4**, 2696 (1971).
[12] V. G. Vaks, *Introduction to the Microscopic Theory of Ferroelectrics* [in Russian], Nauka, Moscow (1973), 328 pp.
[13] O. G. Vendik and I. G. Mironenko, Fiz. Tverd. Tela (Leningrad) **16**, 3445 (1974) [Sov. Phys. Solid State **16**, 2230 (1974)].
[14] J. D. Axe, Phys. Rev. B **1**, 1227 (1970).

Translated by R. M. Durham

Adsorption-stimulated bifurcation transition in a silicon–porous-silicon system

V. M. Demidovich, G. B. Demidovich, V. R. Karib'yants, and S. N. Kozlov

M. V. Lomonosov State University, Moscow
(Submitted April 20, 1998)
Pis'ma Zh. Tekh. Fiz. **24**, 30–34 (November 12, 1998)

It is shown that after a porous layer has been formed electrochemically on a silicon surface at elevated anode currents, the silicon–porous-silicon system is in a quasisteady nonequilibrium state from which it may be transferred under the influence of fairly weak adsorption effects. © *1998 American Institute of Physics.* [S1063-7850(98)00511-4]

A silicon–porous-silicon system has recently attracted close attention among researchers because of the extremely encouraging prospects for using it in optoelectronics[1,2] and in chemical sensor technology.[3,4] Here we draw attention to characteristics of this system which are attributable to the manner in which it forms, that is the strong nonequilibrium of the anodization process, the nanocrystalline fractal structure of porous silicon, and also the presence of a developed mechanically stressed interface.[1] As a result, strongly nonequilibrium quasisteady states may be established in the Si–porous-silicon system with substantially enhanced sensitivity to external influences.

For the experiments we employed structures fabricated using *p*-Si with resistivity 1 $\Omega\cdot$cm. Layers of porous silicon 1 μm thick with 60–70% porosity were prepared on an Si(100) surface by anodization using a 1:1 mixture of 48% HF solution and 96% ethanol at current densities $i_a = 1-50$ mA/cm^2. In order to conserve the nonequilibrium state of the Si–porous-silicon system as well as possible, after anodization electrolytic contact was established on the porous silicon side using an aqueous 0.01 N KBr solution. The electrode potential φ_e of the silicon was varied in a sawtooth fashion relative to a platinum reference electrode at a frequency 0.005 Hz and the differential capacitance of the semiconductor–electrolyte system C_s was recorded. The capacitance C_s was measured by a pulsed method with charging pulses of length 40 μs, repetition frequency 10 Hz, and pulse current density of at most 5 μA/cm^2. The range of variation of φ_e was selected so that the current density across the silicon–electrolyte interface was less than a few μA/cm^2. To stimulate transfer of the system from the nonequilibrium quasisteady state we used alizarin molecules, which, because of their structure, could act as either electron donors or acceptors. All the measurements were made at room temperature.

Figure 1 shows typical dependences $C_s(\varphi_e)$ for two structures with porous silicon layers of the same thickness, obtained at different anode currents. Also plotted for comparison is the $C_s(\varphi_e)$ curve for the initial Si–electrolyte system without a porous silicon layer. The similar values of the minimum capacitance for all the structures indicate that in accordance with published data,[5] the nanocrystalline matrix of the porous silicon does not participate in the electrical transport because of the carrier depletion, and the charge transfer current C_s flows exclusively through the ''bottoms'' of the pores.

At high positive φ_e, C_s increases rapidly as a result of the formation of a strong accumulation layer in the *p*-Si. In this range of φ_e the capacitance C_s is mainly determined by the capacitance of the silicon space charge region. Figure 1 shows that the initial structure and also the Si–porous-silicon structure formed at low anode current with the same potential φ_e have approximately the same values of C_s. It has been shown that the broad $C_s(\varphi_e)$ maximum observed in the range $-0.7\text{ V} < \varphi_e < 0.7$ V for an Si–electrolyte system without a porous silicon layer is attributable to defects at the Si–oxide interface. The absence of a C_s maximum for the structures with a porous silicon layer indicates that no oxide phase is present at the ''active'' Si–electrolyte interface (near the bottoms of the pores). This promotes closer contact between the adsorbed molecules and the ''active'' surface of the silicon and is responsible for the high adsorption sensitivity of the Si–porous-silicon–electrolyte system.

In those cases where the current i_a exceeded 10–15 mA/cm^2 during the preparation of the porous silicon layer, the dependence $C_s(\varphi_e)$ revealed a substantial (more than 0.1 V) shift to the left along the φ_e axis. Thus, under these conditions negative charge builds up on the silicon surface. The magnitude of this charge increases with the current density during the preparation of the porous silicon increases. In particular, for $i_a = 40-50$ mA/cm^2 the shift of the $C_s(\varphi_e)$ curve along the φ_e axis was 0.7–0.75 V (Fig. 1, curve *3*).

Quite clearly, the strong nonequilibrium of the anodization process at elevated i_a gives rise to structures with many strained and broken bonds in the Si-porous silicon transition layer. Some of these defects function as acceptor electron traps at which negative charge is localized. This state of the system is quasisteady (it may persist for a few days) but nonequilibrium. After 0.2 mmol/l alizarin is added to the electrolyte solution, the system leaves this state and the $C_s(\varphi_e)$ curve gradually shifts 1.2 V into the anode region (Fig. 2). The slowed kinetics of the process is evidently attributable to the impeded diffusion of the alizarin molecules in the porous silicon layer. We stress that when alizarin was adsorbed on a structure formed at low i_a, the shift of the $C_s(\varphi_e)$ curve under the same conditions was several times smaller.

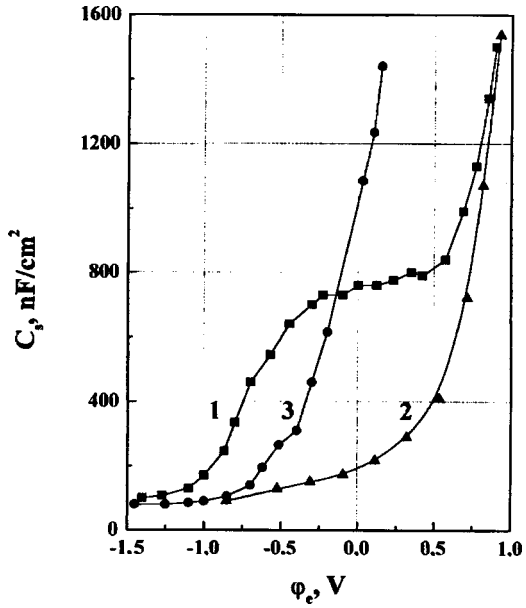

FIG. 1. Differential capacitance of Si–electrolyte (*1*) and Si–porous-silicon–electrolyte systems (*2*, *3*), as a function of electrode potential. Anode current density during preparation of porous layer: 1 mA/cm^2 (*2*) and 50 mA/cm^2 (*3*).

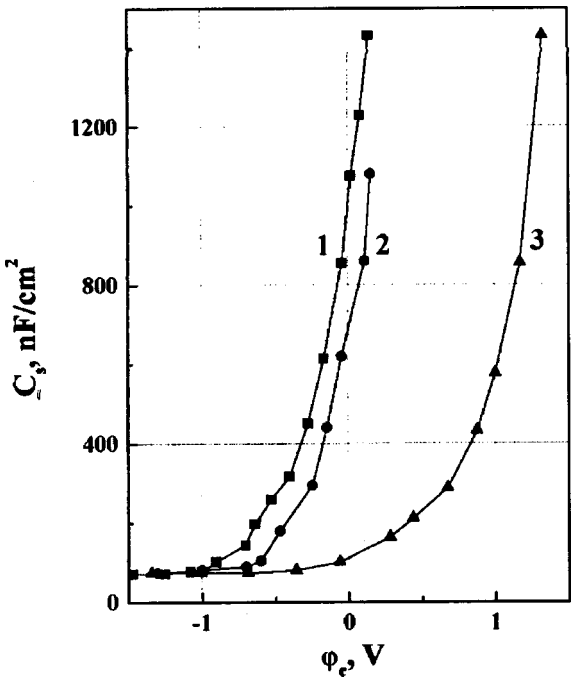

FIG. 2. Differential capacitance of Si–porous-silicon–electrolyte system as a function of electrode potential in initial nonequilibrium state (*1*), and also 1 h (*2*) and 25 h(*3*) after adding alizarin to the electrolyte solution.

Two mechanisms may be responsible for the influence of adsorption on the charge state of an Si–porous-silicon system. The first is a purely electrophysical mechanism involving the charging of donor trapping centers created by the alizarin molecules. The energy levels of these states at a negatively charged surface are substantially higher than those in the absence of this charge. Thus, the magnitude of the adsorption effect is appreciably higher in the first case. A second possible mechanism for this effect is a change in the mechanical stresses in the Si–porous-silicon transition region induced by the adsorption,[5] which stimulates structural rearrangements, modification of the energy spectrum, and charge transfer of the silicon surface.

[1] A. G. Cullis, L. T. Canham, and P. D. J. Calcott, J. Appl. Phys. **2**, 909 (1997).
[2] Y. Kanemitsu, Phys. Rep. **263**, 1 (1995).
[3] V. M. Demidovich, G. B. Demidovich, E. I. Dobrenkova, and S. N. Kozlova, Pis'ma Zh. Tekh. Fiz. **18**(14), 57 (1992) [Sov. Tech. Phys. Lett. **18**, 459 (1992)].
[4] G. M. O'Halloran, M. Kuhl, and P. J. Trimp, Sens. Actuators A **61**, 415 (1997).
[5] G. Dolimo, D. Bellet, and C. Faivre, Phys. Rev. B **54**, 17 919 (1996).

Translated by R. M. Durham

Investigation of the degradation of silane molecules in a pulsed volume discharge

A. K. Shuaibov, L. L. Shimon, A. I. Dashchenko, and A. I. Minya

Uzhgorod State University
(Submitted June 4, 1998)
Pis'ma Zh. Tekh. Fiz. **24**, 35–39 (November 12, 1998)

Results are presented of an investigation of the electrical and optical characteristics of a pulsed transverse discharge ignited in a $54\times2.0\times0.7$ cm volume of an $Ar+4\%SiH_4$ mixture. Studies were made of general spectra of the plasma radiation and the temporal and service-life characteristics of the radiation from the degradation products of the silane molecules. This type of discharge is of interest for obtaining porous silicon coatings over large areas.
 [S1063-7850(98)00611-9]

When pulsed volume discharges in Freon (CF_4) are used in plasma chemistry to etch photoresist films,[1] the chemically active degradation products of Freon molecules exhibit high efficiency. It is also of interest to use these discharges to obtain semiconducting silicon-based porous coatings. Thin silicon films are usually obtained using low-current silane discharges ($[SiH_4]\leqslant10^{15}\,cm^3$) with a low electron density ($n_e\leqslant10^9\,cm^3$) (Ref. 2), or by deposition of Si atoms from a gas onto a substrate heated to 300–400 °C, using a high-power excimer laser.[3,4] The use of a pulsed volume discharge can increase n_e by five or six orders of magnitude and the silane concentration by more than one order of magnitude. This is important to speed up the deposition of silicon-containing coatings. It is particularly interesting to study the conditions for obtaining large silicon-containing clusters, including fullerene-like ones ($Si_{60}H_{60}$), in a transverse discharge plasma, which is important for the development of optoelectronic devices based on porous silicon luminescence.

Here we present results of an investigation of the degradation of silane molecules in a pulsed volume discharge ignited in an $Ar+4\%SiH_4$ mixture at pressure $P = 1$–10 kPa.

Experiments to study the degradation of silane molecules were carried out in the emitter of an excimer laser pumped by a transverse discharge with automatic spark preionization.[5,6] The discharge volume was $54\times2.0\times0.7$ cm. The main storage capacitance of the pulse voltage generator was 40 nF and the peaking capacitance was 34 nF. The switch was a TGI1 1000/25 thyratron. The system used to record the discharge characteristics was similar to that used in Ref. 7. The residual pressure in the discharge chamber was $\leqslant10$ Pa. Before admission of the mixture, the chamber was repeatedly flushed with helium and an Ar/SiH_4 mixture.

In the general spectrum of the discharge plasma radiation the broad-band radiation of the ArH* molecules in the 250–400 nm range with $\lambda_{max}=300$ nm (Ref. 8) and the $N_2(C-B)$ bands exhibited the highest intensity. Among the atomic degradation products of SiH_4 the $\lambda=288.2$ nm SiI line ($3p^2\,{}^1D_2$–$4s^1P_1^0$) exhibited the highest intensity.[9] Hydrogen is represented by the $\lambda=486.1$ nm H_β line in the discharge radiation spectrum with isolated weak ArI and SiII lines also being observed. At the initial instants of discharge ignition, emission lines of excited silicon atoms predominated. Figure 1 gives the emission intensity of the 288.2 nm SiI line and the H_β line as a function of the number of discharge pulses for a pulsed volume discharge in an Ar/SiH_4 mixture. The $\lambda=288.2$ nm SiI line can be used for diagnostics of the excited silicon atoms in the discharge plasma. Its dependence on the number of discharge pulse has two peaks. The first was always observed at the beginning of discharge ignition in the freshly prepared mixture ($n=0$) and the second was observed after $n=(2$–$3)\times10^3$ pulses. When the energy deposited in the discharge increased by a factor of four, the magnitude of the peaks increased, their width decreased, and the peaks were shifted toward lower n. The first intensity peak of the SiI radiation as a function of n was caused by degradation of the initial SiH_4 molecule and the second was caused by degradation of silane derivatives, Si_2H_4 or Si_2H_6, which form efficiently in a silane molecular plasma.[2] The H_β line typically showed an increase in intensity with increasing n, which indicated that H* atoms formed as a result of the degradation of silane molecules and their derivatives. The saturation of the H_β radiation intensity also depends on the energy deposited in the discharge and indicates that SiH_4 molecules and more complex compounds of silicon atoms with hydrogen present in the bulk of the discharge are almost completely decomposed.

Figure 2 shows oscilloscope traces of the current and discharge radiation at different stages in the degradation of an Ar/SiH_4 plasma. At low active-medium pressures, an appreciable mismatch was observed between the impedances of the plasma and the pump generator, which resulted in the appearance of three or four current–pump waves with a half-wave duration of 50–100 ns. The width of the radiation pulses on the 288.2 nm SiI transition was greatest initially, but its maximum was reached only after the second current–pump half-wave. With time the duration of the leading edge of the Si*I radiation pulse decreased and the pulse became shorter. This behavior is consistent with the profile of the service-life characteristic of this SiI line. The emission on the H_β line was of $\geqslant500$ ns duration and exhibited the highest intensity for $n\geqslant10^3$ pulses. These temporal characteristics of the radiation indicate that different mechanisms are responsible for the formation of excited silicon atoms with increasing n. A reduction of the Ar/SiH_4 mixture pressure by a

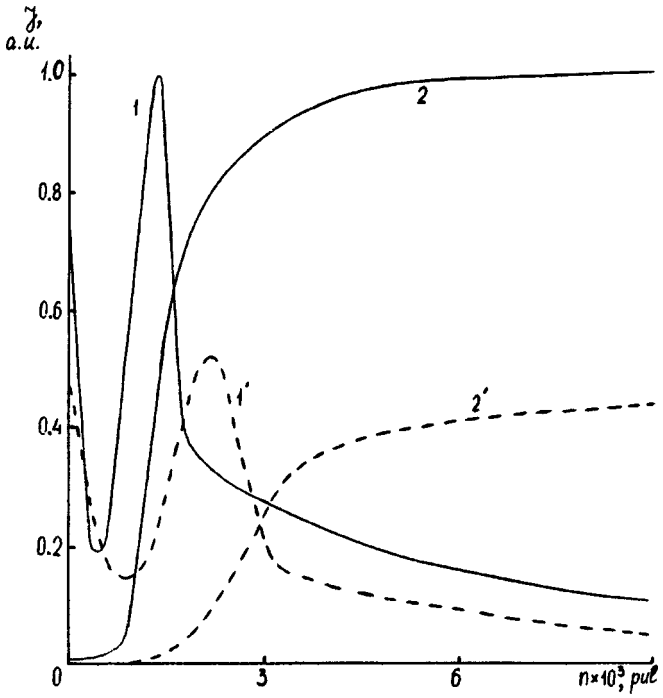

FIG. 1. Emission intensity of the degradation products of silane molecules as a function of the number of discharge pulses in an Ar/SiH_4 $=4.6/0.19$ kPa mixture at $U_3=15$ (*1, 2*) and 7.5 kV (*1′,2′*): *1, 1′* — 288.2 nm SiI ($3p-4s$); *2, 2′* — 486.1 nm H_β.

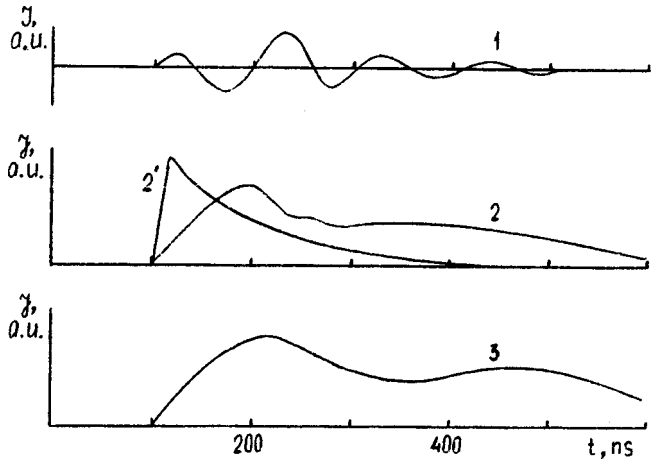

FIG. 2. Oscilloscope traces of the current (*1*) and emission of the degradation products of a pulsed volume discharge in an Ar/SiH_4 mixture at U_3 $=15$ kV at different stages in the operation of the transverse-discharge emitter: *2, 2′* — 288.2 nm SiI ($n\leqslant 10$; $n\geqslant 2\times 10^3$ pulses), *3* — H_β ($n\geqslant 4\times 10^3$ pulses).

factor of three did not cause any appreciable changes in the behavior of the SiI* and H_β radiation with time or increasing n. A reduction in the charging voltage to 7.5 kV resulted in the appearance of two or three peaks of 50 ns duration (for $n\geqslant 4\times 10^3$) on the trailing edge of the emission pulses of the Si* atoms. This emission on the Si*I transition may be attributed to the contribution of different channels for dissociative excitation of the silane degradation products Si_2H_4 and Si_2H_6.

After the emitter had been filled 10–15 times with Ar/SiH_4 mixture ($P=5$–10 kPa) and subjected each time to 10^4 ,pulses, the transverse discharge electrodes and the inner surface of the discharge chamber were coated with a porous layer (~ 0.5 mm) of brown silicon compounds. Batishche *et al.*[4] obtained similar products of silane synthesis (a porous brown film on a quartz substrate) using a laser spark in mixtures of rare gases and SiH_4 molecules ($P=1$–20 atm). An x-ray structural analysis of the coating made in the present study showed that its structure (d = 50–100 nm) is similar to that of silicon crystals.

To sum up, an investigation of the degradation of silane in a pulsed volume discharge has shown that at high SiH_4 pressures ($\geqslant 10^{16}$ cm^{-3}) and $n_e\geqslant 10^{14}$ cm^{-3} a homogeneous discharge is obtained suitable for preparing a porous silicon-containing coating on a working surface of large area (S $\leqslant 30\times 60$ cm). The 288.2 nm SiI line may be used for diagnostics of the degradation of silane molecules (and its derivatives) and to obtain a porous silicon-containing coating.

[1] Yu. D. Korolev, G. A. Mesyats, and A. M. Yarosh, Khim. Vys. Énerg. **21**, 464 (1987).
[2] A. F. Stekol'nikov, O. M. Ivanov, A. E. Pereverzev *et al.*, in *Proceedings of the Eighth All-Union Conference on Physics of Low-Temperature Plasmas*, Minsk, 1991, Part 1 [in Russian], p. 27.
[3] V. Yu. Baranov, V. M. Borisov, and Yu. Yu. Stepanov, *Electric-Discharge Excimer Lasers Using Rare Gas Halides* [in Russian], Énergoatomizdat, Moscow, 216 pp.
[4] S. A. Batishche, A. A. Kuz'muk, and N. A. Malevich, in *Laser Physics and Spectroscopy, Proceedings of the Third Conference on Laser Physics and Spectroscopy*, Minsk, 1997, Vol. 1 [in Russian], p. 59.
[5] Yu. Yu. Neĭmet, A. K. Shuaibov, V. S. Shevera *et al.*, Zh. Prikl. Spektrosk. **53**, 337 (1990).
[6] Yu. Yu. Neĭmet, A. K. Shuaibov, and V. S. Shevera, Prib. Tekh. Éksp., p. 203.
[7] A. K. Shuaibov, Pis'ma Zh. Tekh. Fiz. **24**(1), 85 (1998) [Tech. Phys. Lett. **24**, 38 (1998)].
[8] T. Moller, M. Beland, and G. Zimmerer, Chem. Phys. Lett. **136**, 551 (1987).
[9] A. R. Striganov and G. A. Odintsova, *Handbook of Tables of Spectral Lines of Atoms and Ions* [in Russian], Energoatomizdat, Moscow (1982), 312 pp.

Translated by R. M. Durham

Investigation of the influence of residual stresses on the thermophysical and thermoelastic properties of silicon nitride ceramic by photothermal and photoacoustic methods

K. L. Muratikov, A. L. Glazov, D. N. Rose, and J. E. Dumar

A. F. Ioffe Physicotechnical Institute, Russian Academy of Sciences, St. Petersburg
(Submitted June 19, 1998)
Pis'ma Zh. Tekh. Fiz. **24**, 40–48 (November 12, 1998)

Photodeflection and photoreflection microscopy have been used to show that residual stresses do not influence the thermophysical parameters of silicon nitride ceramic. It was demonstrated that photoreflection microscopy can provide information on the thermophysical properties of ceramics at the level of individual grains. It was established that the theory of photoacoustic signal formation with a piezoelectric recording method based on the Murnaghan model with allowance for the stress dependence of the thermoelastic coupling coefficient can qualitatively explain these experimental data and can be used to estimate the thermoelastic parameters of the ceramic. © *1998 American Institute of Physics.* [S1063-7850(98)00711-3]

Studies of residual stresses in various materials and the development of methods of recording them have attracted considerable attention. Among the most important methods used to solve this problem, mention may be made of ultrasound,[1] Raman spectroscopy,[2,3] x-ray[4] and neutron diffraction,[5,6] magnetic methods,[7] and also methods based on holographic interferometry.[8–10] Such methods have proved highly efficient for the recording of residual stresses, although each has specific limitations associated with the nature of the physical processes used.

In view of this, serious attention has recently been paid to studying the possibility of using the thermoelastic effect for the diagnostics of mechanical stresses in solids.[11–16] An important advantage of the thermoelastic method is that it is universally applicable and can be used for objects of various types. Various experimental data have already been obtained for metals[11,14,15] and ceramics,[12,13,16] which confirm this possibility. However, the mechanism responsible for the influence of mechanical stresses on the results of thermoelastic measurements has not been sufficiently well explained. In Ref. 14, for example, Qian proposed a model for the formation of the thermoelastic signal which essentially attributes its dependence on the mechanical stresses to a dependence of the thermophysical parameters of the material on these stresses. In Ref. 17, however, Muratikov explained the behavior of the thermoelastic signal using the nonlinear mechanical model of a solid proposed by Murnaghan,[18] taking into account a possible dependence of the coefficient of thermoelastic coupling on the mechanical stresses.[19]

In this context, the main aim of the present study is to identify the nature of the formation of the thermoelastic signal in solid-state objects with internal stresses. A complex approach based on using several photothermal and photoacoustic methods at the same time was used to make an experimental determination of the mechanism responsible for the formation of the thermoelastic signal. The photothermal methods used included photodeflection and photoreflection methods and we also used a photoacoustic method where the signal was recorded with a gas microphone. A distinguishing feature of these methods is that they are only sensitive to the thermophysical parameters of the object.[20] In addition, the sample was investigated by a photoacoustic method with a piezoelectric method of recording the signal, which is also sensitive to the elastic parameters and the coefficient of thermoelastic coupling of the material.

The experimental investigations were carried out using silicon nitride ceramic prepared by hot pressing.[1)] Fields of residual stresses were created in the ceramic by means of Vickers indentation using loads between 5 and 15 kg. An image of the part of the ceramic being studied was obtained by scanning the sample along two coordinates with a 5 μm step. Thermal waves and acoustic vibrations were excited in the sample using LGN-503 argon laser radiation modulated with an ML-201 acoustooptic modulator. Radiation from a Meles Griot 05-LHP-151 He–Ne laser was used for readout in the photodeflection and photoreflection methods.

Figures 1 and 2 show images of the region near the indentation zone in silicon nitride ceramic obtained by the photodeflection and photoreflection methods. It can be seen that the image formed using the normal component of the photodeflection signal accurately reproduces the structure of the subsurface lateral cracks and is basically similar to the images obtained by the gas microphone method. In the image obtained by the photoreflection method the granular nature of the ceramic structure shows up much more clearly, although both images were obtained at the same exciting radiation frequencies. We note that this characteristic is not caused by optical differences when the readout radiation is reflected from different grains in the photoreflection method, since the optical image of this part of the ceramic formed at the same time as the photoreflection image was fairly homogeneous. The ceramic inhomogeneities shown in Fig. 2 are therefore of a thermal nature and may be caused by a spread of the thermophysical parameters of the grains and grain

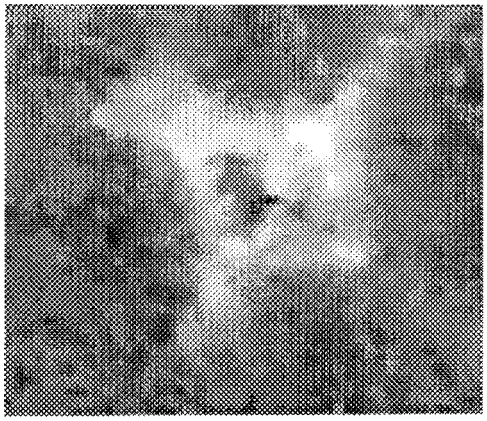

FIG. 1. Image of area of silicon nitride ceramic near Vickers indentation zone obtained by recording the amplitude of the normal component of the photodeflection signal. Load, 10 kg; size of image, 240×240 μm; modulation frequency of exciting radiation, 10 kHz.

boundaries. This characteristic of the images obtained by the two thermal wave methods is attributable to the different resolution of the thermal wave microscopy systems.[21,22]

Figure 3 shows an image of the region near the same indentation zone as in Figs. 1 and 2 obtained by the photoacoustic method with the signal recorded by a piezoelectric technique. The most characteristic feature of this image is the presence of bright regions near the ends of the vertical cracks which correspond to a substantial increase in the photoacoustic signal. In Ref. 23, Cantrell *et al.* noted similar characteristics in images of Vickers indentation zones obtained by electron acoustic microscopy and showed that these bright regions near the ends of vertical cracks correspond to zones of residual stresses. It can be seen from Figs. 1 and 2, and also from the photoacoustic images obtained using a gas microphone method of signal recording,[24] that similar characteristics are not observed on any of these images. This suggests that the photoacoustic signal in silicon nitride ceramic is not formed as a result of a dependence of the thermophysical parameters on the mechanical stresses and is mainly attributable to the dependence of the elastic parameters and the coefficient of thermal expansion on these stresses.

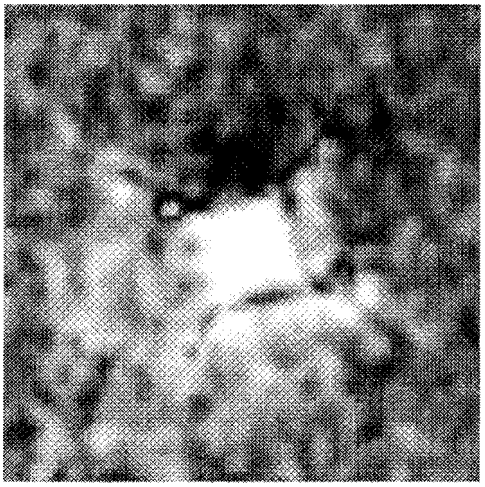

FIG. 2. Image of area of silicon nitride ceramic near Vickers indentation zone obtained by recording the amplitude of the normal component of the photoreflection signal. Load, 10 kg; size of image, 320×320 μm; modulation frequency of exciting radiation, 10 kHz.

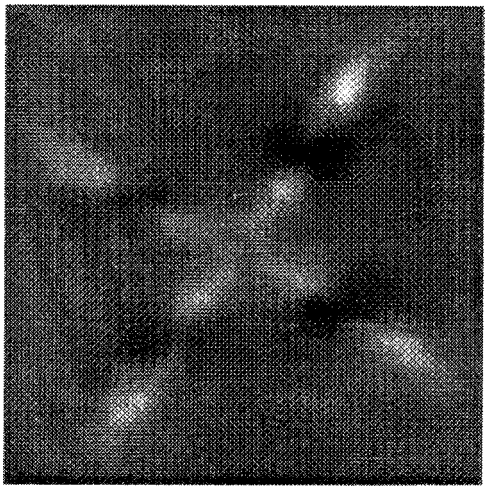

FIG. 3. Image of area of silicon nitride ceramic near Vickers indentation zone obtained by a photoacoustic method with the signal amplitude recorded by a piezoelectric method. Load, 10 kg; size of image, 320×320 μm; modulation frequency of exciting radiation, 113 kHz.

In Ref. 17, Muratikov derived the following expression for the piezoelectric signal for moderately high modulation frequencies of the exciting laser radiation and no nonlinear geometric distortions of the sample under deformation:

$$V(\omega) = i\, C \kappa \rho_0^{3/2} \omega^2 \times \frac{\gamma_0 (1+\beta U_{33}) \Delta T_s}{\left\{ K + \frac{4}{3}\mu + [t_{33}^{(0)} + (2lU_{pp} + (4m+n)U_{33})] \right\}^{3/2}}, \quad (1)$$

where C is the proportionality factor determined by the parameters of the piezoelectric element, ω is the angular modulation frequency of the exciting radiation, ρ_0 is the density of the solid, κ is the thermal diffusivity, γ_0 is the coefficient of thermoelastic coupling for the undeformed solid, β is a coefficient which determines the dependence of the thermoelastic coupling on the initial deformation, U_{ik} is the initial deformation tensor of the solid, K and μ are the bulk modulus and the shear modulus, respectively, l, m, and n are the Murnaghan constants, $t_{33}^{(0)}$ is the component of the stress tensor associated with the initial deformation, and ΔT_s are the temperature fluctuations of the sample surface. Expression (1) can be used to estimate the influence of the internal stresses on the piezoelectric signal. In particular, we can use the dependence of the amplitude of the piezoelectric signal on the indentation load.

Figure 4 shows typical behavior of the photoacoustic signal as a function of the load. The values plotted in Fig. 4 are the maxima in the bright regions averaged over the four regions near the ends of the vertical cracks and normalized to the average signal from the sample. It can be seen that in the range being studied the dependence of the photoacoustic signal on the load is fairly close to linear. In accordance with

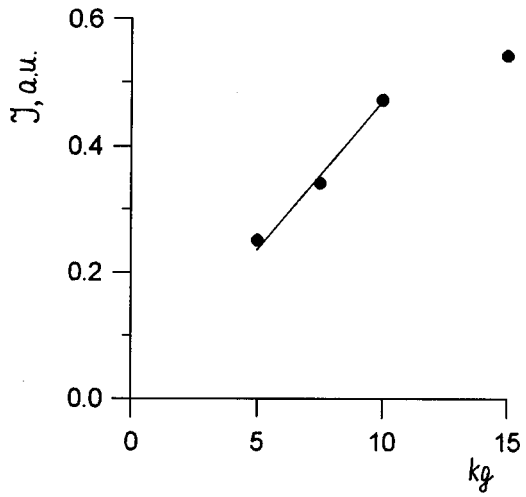

FIG. 4. Behavior of maximum photoacoustic signal recorded by a piezoelectric method as a function of the load. The modulation frequency of the exciting radiation was 98 kHz.

expression (1), a similar situation may occur if the influence of the residual strains and stresses is exerted mainly via the quantities contained in the numerator of expression (1). Under these conditions. expression (1) can be used to draw some conclusions as to the value of the coefficient β for silicon nitride ceramic. For ceramics the strains corresponding to fracture of the material are usually less than 1% (Ref. 25). For a 15 kg indentation load the maximum photoacoustic signal for this sample was 47% higher than the average signal level from the ceramic. Then, assuming that the maximum strain of the ceramic does not exceed 1%, on the basis of expression (1) the value of β for this sample should be around 10^2, which is substantially higher than that for metals.[19] Expression (1) and the data plotted in Fig. 4 show that the photoacoustic measurements can also be used to determine the Murnaghan constants, since, in accordance with expression (1), at high loads the signal increases more slowly than linear. For this purpose, however, it is advisable to use model tension or compression experiments because the stress field created by Vickers indentation is fairly complex.

To sum up, these results show that the combined use of photothermal and photoacoustic methods can yield important conclusions on the influence of internal stresses on the thermophysical and thermoelastic properties of ceramics. They also show that the theory of the photoacoustic effect proposed in Ref. 17 agrees qualitatively with the experimental results for silicon nitride ceramic.

[1)]We used NC 132 silicon nitride ceramic fabricated by Norton Ceramic Corporation.

[1] Y. H. Pao and W. Sachse, in *Physical Acoustics XVII* (Academic Press, New York, 1984), pp. 61–143.
[2] T. Iwaoka, S. Yokogama, and Y. Osaka, Jpn. J. Appl. Phys., Part 1 **24**, 112 (1984).
[3] M. Bowden and D. J. Gardiner, Appl. Spectrosc. **51**, 1405 (1997).
[4] B. Eigenmann, B. Scholtes, and E. Macherauch, Mater. Sci. Eng., A **118**, 1 (1989).
[5] M. R. Daymond, M. A. M. Bourke, R. B. Von Dreele, B. Clausen, and T. Lorentzen, J. Appl. Phys. **82**, 1554 (1997).
[6] M. Ceretti, C. Braham, J. L. Lebrun, J. P. Bonnafe, M. Perrin, and A. Lodini, Exp. Tech. **20**(3), 14 (1996).
[7] É. S. Gorkunov and M. V. Tartachnaya, Zavod. Labor. **59**(7) 22 (1993).
[8] G. N. Chernyshev, A. L. Popov, V. M. Kozintsev, and I. I. Ponomarev, *Residual Stresses in Deformable Solids* [in Russian], Nauka, Moscow (1996), 240 pp.
[9] M. J. Pechersky, R. F. Miller, and C. S. Vikram, Opt. Eng. **34**, 2964 (1995).
[10] C. S. Vikram, M. J. Pechersky, C. Feng, and D. Engelhaupt, Exp. Tech. **20**(6), 27 (1996).
[11] M. Kasai and T. Sawada, *Photoacoustic and Photothermal Phenomena II*, Springer Series in Optical Sciences Vol. 62 (Springer-Verlag, Berlin, 1990), p. 33.
[12] R. M. Burbelo, A. L. Gulyaev, L. I. Robur, M. K. Zhabitenko, B. A. Atamanenko, and Ya. A. Kryl, J. Phys. (Paris), Colloq. **4**, Colloq. 7, 311 (1994).
[13] H. Zhang, S. Gissinger, G. Weides, and U. Netzelmann, J. Phys. (Paris), Colloq. **4**, Colloq. 7, 603 (1994).
[14] M. Qian, Chin. J. Acoust. **14**(2), 97 (1995).
[15] R. M. Burbelo and M. K. Zhabitenko, *Progress in Natural Science* (Taylor and Francis, Washington, 1996), Supplement 6, p. 720.
[16] K. L. Muratikov, A. L. Glazov, D. N. Rose, J. E. Dumar, and G. H. Quay, Pis'ma Zh. Tekh. Fiz. **23**(5), 44 (1997) [Tech. Phys. Lett. **23**, 188 (1997)].
[17] K. L. Muratikov, Pis'ma Zh. Tekh. Fiz. **24**(13), 82 (1998) [Tech. Phys. Lett. **24**, 536 (1998)].
[18] A. I. Lur'e, *Nonlinear Theory of Elasticity*, North-Holland, Amsterdam (1990); Russian orig., Nauka, Moscow (1980), 512 pp.
[19] R. I. Garber and I. A. Gindin, Fiz. Tverd. Tela (Leningrad) **3**, 176 (1961) [Sov. Phys. Solid State **3**, 127 (1961)].
[20] A. C. Tam, Rev. Mod. Phys. **58**, 381 (1986).
[21] A. L. Glazov and K. L. Muratikov, Zh. Tekh. Fiz. **57**, 2184 (1987) [Sov. Phys. Tech. Phys. **32**, 1320 (1987)].
[22] A. L. Glazov and K. L. Muratikov, Zh. Tekh. Fiz. **60**(2), 164 (1990) [Sov. Phys. Tech. Phys. **35**, 233 (1990)].
[23] J. H. Cantrell, M. Qian, M. V. Ravichandran, and K. W. Knowles, Appl. Phys. Lett. **57**, 1870 (1990).
[24] D. N. Rose, D. C. Bryk, G. Arutunian, J. E. Dumar, and M. J. Slavin, J. Phys. (Paris), Colloq. **4**, Colloq. 7, 599 (1994).
[25] T. J. Mackin and T. E. Purrell, Exp. Tech. **20**(2), 15 (1996).

Translated by R. M. Durham

Influence of gas compressibility on the critical conditions for instability in the electrostatic field of a bubble in a dielectric liquid

A. N. Zharov

Yaroslavl State University
(Submitted April 20, 1998)
Pis'ma Zh. Tekh. Fiz. **24**, 49–54 (November 12, 1998)

It is shown that unlike the case of a liquid droplet, the critical strength of a uniform electrostatic field required for instability of a gas bubble in a liquid dielectric decreases as the compressibility of the gas in the bubble increases. © *1998 American Institute of Physics.*
[S1063-7850(98)00811-8]

The problem of instability of a gas bubble in a uniform electrostatic field $\mathbf{E}_0$ is of interest in connection with studies of the electrical breakdown of liquid dielectrics since, at the instant of breakdown, a region of reduced density forms at the cathode, which is taken as being the appearance of a gas (vapor) microbubble.[1] The electrical breakdown of the dielectric may be caused by the buildup of electrostatic instability of this bubble in the field $\mathbf{E}_0$.

Like the instability of a droplet,[2] the instability of a bubble may be caused by its splitting into two daughter bubbles[3] or by the ejection of a large number of highly charged daughter bubbles from the tips of the parent bubble, two orders of magnitude smaller than it.[4,5] The establishment of a particular type of instability is determined by the physical properties of the liquid and the gas, such as the conductivity, permittivity, temperature, compressibility, and so on.

The following analysis will focus on the second type of instability, which may occur when a bubble has highly conducting walls. The bubble walls may exhibit good conductivity as a result of ionization of the gas in the bubble (formation of a plasma bubble in the presence of local breakdown) and also because carriers (both positive and negative ions) from the liquid, whose surface mobility may appreciably exceed the bulk mobility, are deposited on the walls.

Let us assume that a spherical gas bubble of initial radius r_0 is formed in the absence of an electric field $\mathbf{E}_0$ in a dielectric with permittivity ε. The free surface of the dielectric is exposed to the action of atmospheric pressure P_{at}. The gas in the bubble is characterized by the isothermal coefficient of compressibility χ and the initial gas pressure exceeds atmospheric by a factor of μ_0. The phase interface has the surface tension σ. The dimensionless pressure μ_0 in the bubble is given by

$$\mu_0 = 1 + \frac{2\sigma}{P_{\text{at}} r_0}. \tag{1}$$

To estimate the maximum initial pressure we take $P_{\text{at}} \approx 10^6$ dyn/cm^2, $\sigma \approx 50$ dyn/cm, and $r_0 = 10^{-5}$ cm. Expression (1) then gives $\mu_0 \approx 11$.

In a uniform electrostatic field $\mathbf{E}_0$, the bubble is pulled along $\mathbf{E}_0$ into a spheroid of revolution with the square of the eccentricity e^2. This is accompanied by a change in the volume of the bubble. We shall assume that as a result of the bubble being pulled into a spheroid, the radius r of the equivalent bubble is greater by a factor of $(1+K)$ than the initial radius r_0, i.e.,

$$r = r_0(1+K). \tag{2}$$

The gas pressure, in accordance with the basic equation of molecular kinetic theory, will be determined by the volume of the system and the temperature. Assuming that the temperature of the liquid does not change and taking account of Eq. (2), we find the dimensionless gas pressure μ in the bubble using the definition of the isothermal coefficient of compressibility χ (Ref. 6):

$$\mu = \mu_0 - \frac{1}{(\chi P_{\text{at}})}((1+K)^3 - 1). \tag{3}$$

With a suitable choice of χ, Eq. (3) can describe either a gas or a liquid. For a gas we have $\chi P_{\text{at}} \approx 1$, and for liquids $\chi P_{\text{at}} \approx 10^{-4}$.

Although the bubble changes shape and volume, the pressure balance condition should be satisfied at every point on its walls, especially at the pole point and on the equator line of the bubble.[4,6]

We write expressions for the Laplacian pressure at the equator P_σ^{eq} and pole P_σ^p of a spheroidal bubble which has changed its volume as given by Eq. (2) (Refs. 4 and 7):

$$P_\sigma^{\text{eq}} = \frac{\sigma(1-e^2)^{5/6}}{r_0(1+K)}\left(1 + \frac{1}{(1-e^2)}\right),$$

$$P_\sigma^p = \frac{2\sigma}{r_0(1+K)(1-e^2)^{2/3}}. \tag{4}$$

The electrical pressure at the equator P_E^{eq} and pole P_E^p of a spheroidal bubble with conducting walls may be written as[6]

$$P_E^{\text{eq}} = 0, \quad P_E^p = \frac{\varepsilon E_0^2 e^6}{8\pi(1-e^2)^2(\operatorname{arctanh} e - e)^2}. \tag{5}$$

Using expressions (1) and (3)–(5), we can easily write two equations which express the pressure balance conditions at the equator and pole of a spheroidal bubble. Solving these

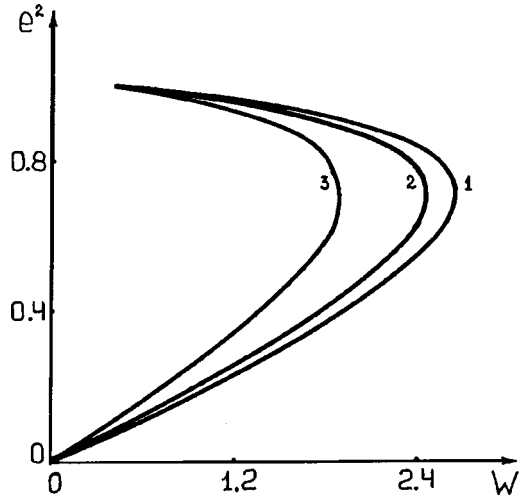

FIG. 1. Square of the eccentricity e^2 versus the Taylor parameter W for a dimensionless initial pressure in the bubble $\mu_0=2$ for various situations: *1* — droplet $\chi P_{at}=10^{-4}$; *2* and *3* — gas bubble with $\chi P_{at}=1$ and $\chi P_{at}=4$, respectively.

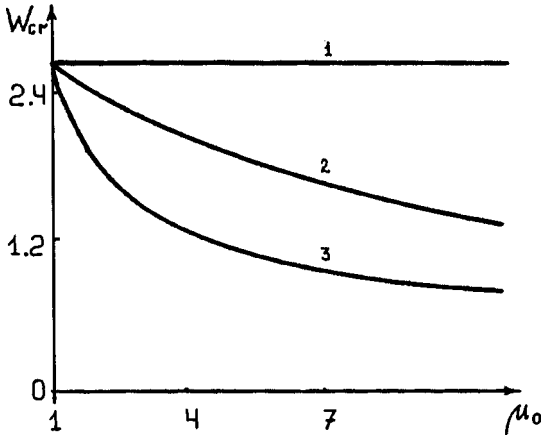

FIG. 2. Critical value of the Taylor parameter W_{cr} versus dimensionless initial pressure μ_0 in bubble for *1* — droplet $\chi P_{at}=10^{-4}$; *2* and *3* — gas bubble with $\chi P_{at}=1$ and $\chi P_{at}=4$, respectively.

equations jointly, we obtain a system of equations which can be used to determine the square of the eccentricity e^2 and the value of K as a function of the Taylor parameter $W=(\varepsilon E_0^2 r_0)/\sigma$ for the bubble:

$$\frac{We^6}{16\pi(1-e^2)^2(\operatorname{arctanh}(e)-e)^2}=\frac{1}{(1+K)}\left\{\frac{1}{(1-e^2)^{2/3}}-\frac{(1-e^2)^{5/6}}{2}\left[1+\frac{1}{(1-e^2)}\right]\right\}, \quad (6)$$

$$\left[\mu_0-1+\frac{1}{\chi P_{at}}\right](1+K)-\frac{(1+K)4}{\chi P_{at}}-\frac{(\mu_0-1)(1-e^2)^{5/6}}{2}\left[1+\frac{1}{(1-e^2)}\right]=0. \quad (7)$$

Calculations using Eqs. (6) and (7) show that for a certain value of W the derivative $\partial e^2/\partial W$ becomes infinite (Fig. 1). It was noted in Refs. 4 and 7 that when a bubble is elongated to an eccentricity corresponding to the maximum Taylor parameter W_{cr}, it becomes unstable.

Figure 2 gives W_{cr} as a function of the dimensionless initial pressure in the bubble μ_0. It can be seen that for a droplet the critical value of the Taylor parameter does not depend on the initial pressure in the droplet. The value obtained, $W_{cr}=2.64$, shows good agreement with that obtained by Taylor, $W_{cr}=2.63$ (Ref. 7). Figure 2 also shows that the increased compressibility for a gas reduces W_{cr}. We shall qualitatively compare the process of elongation of a liquid droplet and a bubble in order to explain this behavior.

We assume that the strength of the electric field in which the bubble (droplet) is situated has increased by $\Delta\mathbf{E}_0$. This leads to an increase in the electric field pressure at the walls of the conducting bubble (droplet) by $\Delta P_E\sim(\varepsilon\mathbf{E}_0\cdot\Delta\mathbf{E}_0)/(4\pi)$. However, for an equilibrium bubble (droplet) this increase should reduce the internal gas pressure in the bubble or the droplet liquid by $\Delta P_g\sim-(\varepsilon\mathbf{E}_0\cdot\Delta\mathbf{E}_0)/(4\pi)$. This reduction of the internal pressure in the bubble (droplet) is caused by a relative increase in the volume of the bubble (droplet) by

$$\frac{\Delta V}{V_0}\sim\chi\frac{\varepsilon\mathbf{E}_0\cdot\Delta\mathbf{E}_0}{4\pi}. \quad (8)$$

Equation (8) shows that the relative increase in the volume of a liquid droplet is approximately four orders of magnitude less than that for a gas bubble because of the different values of χ for liquid and gas, i.e., the bubble expands substantially. In this case, the Laplacian pressure decreases by $\Delta P_\sigma\sim-[\sigma/(V_0)^{1/3}]\ (\Delta V/V_0)$. Thus, as the electrical pressure increases, the internal pressure of the droplet liquid or the gas in the bubble decreases as a result of an increase in volume, which is infinitely small for a droplet. However, as a result of the increase in volume, the Laplacian pressure only decreases for the gas bubble. This factor reduces the critical value of the Taylor parameter W_{cr} for a gas bubble compared with a droplet.

[1] V. V. Glazkov, O. A. Sinkevich, and P. V. Smirnov, Teplofiz. Vys. Temp. **29**, 1095 (1991).
[2] J. D. Sherwood, J. Fluid Mech. **188**, 133 (1988).
[3] A. I. Grigor'ev, V. A. Koromyslov, and A. N. Zharov, Pis'ma. Zh. Tekh. Fiz. **23**(19), 60 (1997) [Tech. Phys. Lett. **23**, 760 (1997)].
[4] C. G. Garton and Z. Krasucki, Trans. Faraday Soc. **60**, 211 (1964).
[5] A. I. Grigor'ev and S. O. Shiryaeva, Izv. Akad. Nauk SSSR. Ser. Mekh. Zhidk. Gaza No. 2, 3 (1994).
[6] L. D. Landau and E. M. Lifshitz, *Fluid Mechanics*, 2nd ed. (Pergamon Press, Oxford, 1969) [Russ. original, Nauka, Moscow, 1964, 568 pp.].
[7] G. I. Taylor, Proc. R. Soc. London, Ser. A **280**, 383 (1964).

Translated by R. M. Durham

New possibilities for x-ray diagnosis of atherosclerosis using a phase contrast method

V. A. Bushuev and A. A. Sergeev

M. V. Lomonosov State University, Moscow
(Submitted May 13, 1998)
Pis'ma Zh. Tekh. Fiz. **24**, 55–60 (November 12, 1998)

The internal structure of materials with a low scattering power and small density gradient was investigated using a new method of phase contrast x-ray introscopy. Model calculations were made of the contrast image using dynamic x-ray diffraction theory. The object of the investigation was a capillary containing a blood clot, which modeled a blood vessel with a thrombus. As a result, it was shown that the new method has distinct advantages over the conventionally used absorption method in obtaining completely satisfactory images.
 [S1063-7850(98)00911-2]

One of the most important problems in modern medicine is the early diagnosis of atherosclerosis. It is known that when the body's equilibrium is disturbed and the blood contains an increased concentration of lipoproteins, cholesterol deposits (atherosclerotic patches, blood clots or thrombi) begin to form at the walls of the blood vessels (arteries, veins) and their growth leads to narrowing of the vessels, resulting in stenocardia, myocardial infarction, and thrombophlebitis.

At present, the main methods of studying the internal structure of noncrystalline objects, including biomedical ones, are radiography and tomography based on the absorption of x-rays.[1] However, for objects with a fairly uniform density distribution there is the problem that the image obtained has a very low contrast. This is attributable to the low absorption coefficient μ in the soft tissue of biological specimens and to the small $\mu(\mathbf{r})$ difference in different parts of the specimen ($\Delta\mu \leqslant 0.1-0.5\,\mathrm{cm}^{-1}$ for radiation at wavelengths $\lambda \approx 0.5-1$ Å). The contrast obtained for an image of an object having the dimensions $r \leqslant 1-10$ mm is only a few percent, which reduces the efficiency of absorption methods almost to zero. A barium or iodine-based contrast solution is usually introduced into the blood to improve the contrast,[1] subjecting the body to an additional, not completely safe, load.

A new method of phase contrast imaging, based on the refraction of x-rays, has appeared comparatively recently and can substantially improve the image contrast.[2–4] The basic principle of the method is shown in Fig. 1. As a result of passing an x-ray wave through an object having the refractive index $n(\mathbf{r})=1-\delta(\mathbf{r})$, the phase of the wave changes, causing the radiation to be deflected from its initial direction of propagation through angles $\beta \sim \delta$. Since $\delta \sim 10^{-6}$, we find $\beta \approx 0.1''-0.6''$. The angular distribution of the x-rays behind the object is investigated by diffraction reflection from a high-quality crystal analyzer. Since the width $\Delta\vartheta_B$ of the diffraction reflection curve from single crystals is comparable with the angles of deflection of the refracted rays, their reflection from the analyzer at different points on the reflection curve can improve the contrast of the image by around 20–80% (Refs. 3–9). Ingal and Beliaevskaya[7] observed that the phase contrast of the image of arteries and veins in laboratory animals without fixing in formalin may attain 25% and 12%, respectively.

Here we use model calculations based on the dynamic theory of x-ray diffraction to demonstrate that phase contrast imaging is highly sensitive in detecting thrombus-like deposits on the walls of blood vessels.

Figure 1 shows the x-ray system of the phase contrast imaging method. An object *1* is placed in a quasiplane wave formed by preliminary reflection of the x-rays from a crystal monochromator. A crystal analyzer *2* is mounted behind the object in Bragg geometry. The image is recorded on photographic film or other coordinate-sensitive detector, using the reflected beam *3*.

We shall analyze the diffraction of a wave packet $E_0(\mathbf{r})=A_0(x)\exp(i\mathbf{k}\cdot\mathbf{r})$ at a crystal analyzer, where $k=2\pi/\lambda$. The field $E_0(\mathbf{r})$ is formed as a result of the x-rays passing through an object having a nonuniform distribution of absorption coefficient $\mu(\mathbf{r})$ and refractive index $\delta(\mathbf{r})$. The amplitude of the field may be given in the form $A_0(x)=\exp(-\sigma)\exp(l\Phi)$, where

$$\sigma(x)=0.5\int \mu(x,z)\,dS, \quad \Phi(x)=-k\int \delta(x,z)\,dS. \quad (1)$$

Here $\sigma(x)$ is the absorption factor, $\Phi(x)$ is the change in the phase of the wavefront relative to the medium in which the object is placed; integration is performed in the $\mathbf{k}$ direction and the x axis is directed along the surface of the crystal analyzer. The relations (1) are valid for $r \gg (\lambda L)^{1/2}$, where r is the transverse dimension of the object and L is the distance between the object and the analyzer. In this case the image is recorded in the geometric shadow of the object, and wave effects accompanying the diffraction of the x-rays from the object may be neglected.[9] In practice, this implies that $r \gg 10\,\mu$m.

The absorption image $I_a(x)=\exp[-2\sigma(x)]$ recorded when the detector is mounted directly behind the object is determined only by the absorption and by the size of the object, and does not depend on the phase of the wave. The amplitude of the wave reflected by the analyzer for an arbitrary distribution of the incident field $A_0(x)$ may be expressed in the following integral form:[6,9,10]

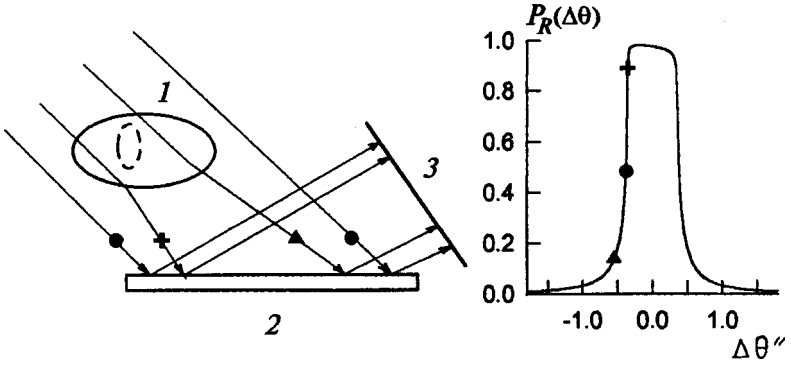

FIG. 1. Schematic of experiment to record phase-contrast image: *1* — object, *2* — crystal analyzer, *3* — photographic film (coordinate-sensitive detector), $P_R(\Delta\vartheta)$ — curve of symmetric diffraction reflection (422) of Ag K_α-radiation from silicon single crystal of width $\Delta\vartheta_B = 0.72''$.

$$A_h(x) = \int G(\xi)\, A_0(x-\xi)\exp(ik\gamma_0\Delta\vartheta\xi)/d\xi, \qquad (2)$$

where

$$G(\xi) = (k\gamma_0/2\pi)\int R(\alpha)\exp(-ik\gamma_0\alpha\xi)/d\alpha. \qquad (3)$$

Here $G(\xi)$ is the Green's function of the Bragg diffraction problem for bounded beams, $R(\alpha)$ is the amplitude coefficient of reflection of a plane wave incident on the analyzer at the angle α relative to the Bragg angle ϑ_B, $\gamma_0 = \sin(\vartheta_B + \psi)$, ψ is the angle of inclination of the reflecting planes to the surface of the crystal, and $\Delta\vartheta$ is the fixed angle of rotation of the analyzer. The explicit form of the Green's function (3) for a thick single crystal is given in Ref. 10.

It follows from Eq. (2) that the distribution of the reflected intensity in the phase contrast imaging method $I(x) = |A_h(x)|^2$ is determined not only by the amplitude of the incident wave but also by its phase $\Phi(x)$, given by (1). If the transverse dimension of the object is $r \gg \Delta\xi = \lambda/\pi\gamma_0\Delta\vartheta_B$ and the angles of refraction $\beta(x) = (1/k\gamma_0)d\Phi/dx$ satisfy the condition $d\beta/dx \ll k\gamma_0\Delta\vartheta_B^2$, it can be shown[6,9] from Eqs. (2) and (3) that the change in the phase of the wave shows up in the dependence of the reflection intensity on the angles $\beta(x)$: $I(x) \approx I_a(x)P_R(\Delta\vartheta - \beta)$, where $P_R = |R|^2$ is the curve of the diffraction reflection from the analyzer. Typical values of $\Delta\xi$ are 5–30 μm.

In order to estimate the sensitivity of phase contrast imaging to the presence of a thrombus in a blood vessel, we shall consider a model object in the shape of a capillary, where r_1 and r_2 are the outer and inner radii of the capillary, δ_1, μ_1 and δ_2, μ_2 are the coefficients of refraction and absorption of the capillary walls and the interior liquid (blood), respectively. We represent a thrombus-like formation on the inner wall of the blood vessel as the common (thrombus radius) and r_2, with the maximum thrombus thickness d. We shall characterize the thrombus material by the refraction coefficient δ_3 and the absorption coefficient μ_3.

Results of calculations of the phase contrast images $I(x)$ (curves *1* and *2*) and the absorption images $I_a(x)$ (curves *3* and *4*) are plotted in Fig. 2 for two cases where a thrombus is present in the right (Fig. 2a) and lower (Fig. 2b) parts of the blood vessel. For comparison curves *2* and *4* give the intensity distributions in the absence of a thrombus. The calculations were made for the following values of the parameters: $r_1 = 2$ mm, $r_2 = r_3 = 1.6$ mm, $d = 1.2$ mm; density of vessel walls, blood, and thrombus $\rho = 1.1$, 1.056, and 1.15 g/cm^3, respectively;[7,8,11] refraction coefficients (in units of 10^{-6}): $\delta_1 = 0.52$, $\delta_2 = 0.496$, $\delta_3 = 0.57$; absorption coefficients: $\mu_1 = 0.69$, $\mu_2 = 0.66$, $\mu_3 = 0.76\,\text{cm}^{-1}$ (Ag K_α-radiation, $\lambda = 0.56$ Å) (Refs. 8 and 11). We shall assume that the blood vessel is in muscle of density 1 g/cm^3, $\delta_0 = 0.47\times10^{-6}$, and $\mu_0 = 0.63\,\text{cm}^{-1}$ (Refs. 8 and 11).

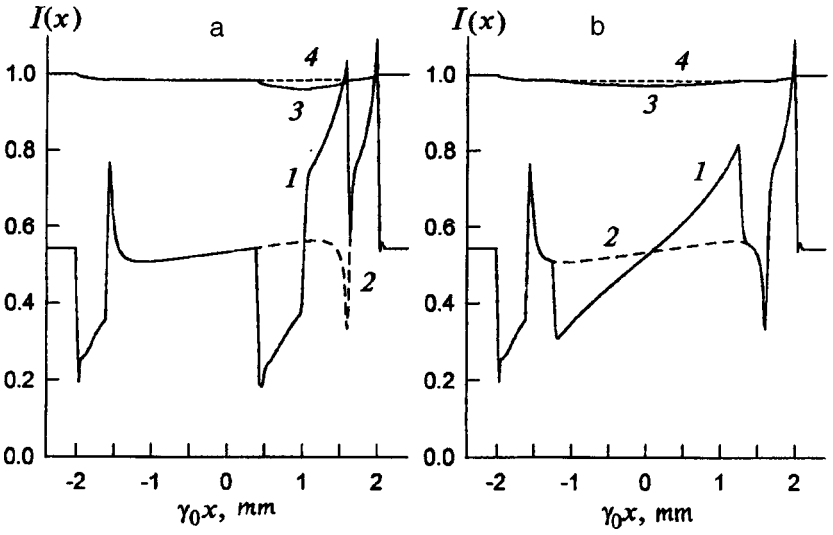

FIG. 2. Intensity distribution on phase contrast (curves *1* and *2*) and absorption (curves *3* and *4*) images of blood vessel with thrombus in right (a) and lower (b) parts of vessel. The dashed curves *2* and *4* show images of a blood vessel without a thrombus. Radiation — Ag K_α, Si(422) analyzer, angle of rotation of analyzer $\Delta\vartheta = 0.38''$, outer radius of blood vessel $r_1 = 2$ mm, inner radius $r_2 = 1.6$ mm, thrombus radius $r_3 = 1.6$ mm, and thickness 1.2 mm.

It can be deduced from Fig. 2 that the contrast of the absorption image $\eta=(I_{\max}-I_{\min})/I_{\max}$ is only 2–4% (curves *3* and *4*). At the same time, it is easy to see that a thrombus, almost unnoticeable in the preceding case, gives a very significant contrast in phase contrast imaging ($\eta\approx$ 50–70%). The outer and inner boundaries of the blood vessel and also the region of localization of the thrombus are also more clearly visible.

These possibilities for the detection of thrombus-like deposits on the walls of blood vessels by phase contrast imaging are important in medicine for the diagnosis of atherosclerosis, ischaemic disease, and insult. Moreover, the body is not exposed to the risks of introducing a contrast substance into the blood. If the incidence of thrombi can be detected in the early stages of formation, it will be possible to avoid not only the associated diseases but also surgical intervention. It is also important to note that the absorbed x-ray dose in the phase contrast method is one or two orders of magnitude lower[4] than that in the standard absorption technique.

[1] B. Swindel and S. Webb, in *The Physics of Medical Imaging*, edited by S. Webb (Adam Hilger, Philadelphia, 1988), p. 138.
[2] V. N. Ingal and E. A. Beliaevskaya, Phys. Medica **12**(2), 75 (1996).
[3] V. N. Ingal and E. A. Belyaevskaya, Zh. Tekh. Fiz. **67**(1), 68 (1997) [Tech. Phys. **42**, 59 (1997)].
[4] V. A. Bushuev, V. N. Ingal, and E. A. Belyaevskaya, Kristallografiya **41**, 808 (1996) [Crystallogr. Rep. **41**, 766 (1996)].
[5] V. A. Bushuev, E. A. Beliaevskaya, and V. N. Ingal, Nuovo Cimento D **19**, 513 (1997).
[6] T. E. Gureyev and S. W. Wilkins, Nuovo Cimento D **19**, 545 (1997).
[7] V. N. Ingal and E. A. Beliaevskaya, Nuovo Cimento D **19**, 553 (1997).
[8] V. N. Ingal and E. A. Beliaevskaya, Surf. Invest. **12**, 441 (1997).
[9] V. A. Bushuev, V. N. Ingal, and E. A. Belyaevskaya, Kristallografiya **43**, 586 (1998) [Crystallogr. Rep. **43** 538 (1998)].
[10] A. M. Afanas'ev and V. G. Kohn, Acta Crystallogr., Sect. A: Cryst. Phys., Diffr., Theor. Gen. Crystallogr. **27**, 421 (1971).
[11] F. M. Khan, *The Physics of Radiation Therapy*, 2nd ed. (Williams and Wilkins, Baltimore, 1994), 351 pp.

Translated by R. M. Durham

Multiwell laser heterostructures fabricated by liquid-phase epitaxy

A. Yu. Leshko, A. V. Lyutetskiĭ, A. V. Murashova, N. A. Pikhtin, I. S. Tarasov, I. N. Arsent'ev, B. Ya. Ber, Yu. A. Kudryavtsev, Yu. V. Il'in, and N. V. Fetisova

A. F. Ioffe Physicotechnical Institute, Russian Academy of Sciences, St. Petersburg
(Submitted February 10, 1998)
Pis'ma Zh. Tekh. Fiz. **24**, 61–67 (November 12, 1998)

A methodology has been developed for growing InGaAsP/InP multiwell laser heterostructures by liquid-phase epitaxy. Depth profiling using a secondary ion mass spectrometer was used to investigate the distribution profiles of the composition of multiwell laser heterostructures. Liquid-phase epitaxy was used to fabricate InGaAsP/InP multiwell laser heterostructures with active regions having emission wavelengths of 1.3 and 1.55 μm and their radiative characteristics were studied. © *1998 American Institute of Physics.* [S1063-7850(98)01011-8]

Fundamental results in terms of improving the parameters of laser diodes using InGaAsP/InP solid solutions have been achieved by utilizing the properties of InGaAs strained epitaxial layers in laser heterostructures fabricated by MOS hydride technology.[1,2] In these strained InGaAs layers, the band structure of the semiconductor changes as a result of elastic deformation, reducing the Auger recombination and optical absorption caused by transitions of holes to the spin–orbit split band,[3] which can improve the radiative characteristics of laser diodes.

The successful development of a technique for liquid-phase epitaxy of thin layers of InGaAsP solid solutions[4] has allowed this to be used to fabricate laser heterostructures. For laser heterostructures fabricated by liquid-phase epitaxy whose thickness and composition are less uniform, it is vital to maintain low internal optical losses as the cavity length increases. By using a multiwell active region[5] in the laser structure, it is possible to achieve an optimum combination of the properties of thin strained InGaAs layers and separate-confinement heterostructures with low optical losses.

Thus, the aim of the present study was to develop a technique for liquid-phase epitaxy of multiwell laser heterostructures and to study their properties.

One of the methods of fabricating thin epitaxial layers by liquid-phase epitaxy was taken as the basis of the technique for growing multiwell laser heterostructures.[6] The basic idea involves reducing the time of contact between the supercooled flux and the substrate by increasing the rate of displacement of the substrate relative to the fluxes using smaller cells. The essential feature of the proposed technical approach involves the formation of a multiwell heterostructure during a single pass of the substrate relative to the cells containing the fluxes, which gives a constant rate of displacement of the substrate relative to all the cells and thus produces quantum wells of the same thickness. The thicknesses of epitaxial layers of different compositions are varied by varying the size of the cells containing the fluxes.

With due allowance for the requirements of the technological process, we constructed a graphite cassette (Fig. 1) which can be used to fabricate the multiwell heterostructure whose band diagram is shown in Fig. 2. The depth distribution profile of the composition of the multiwell laser heterostructure was investigated by depth profiling using a CAMECA IMS-4f secondary-ion mass spectrometer.

For the primary beam we used 10 keV $^{133}Cs^+$ ions with a kinetic energy of 5.5 keV incident on the target at an angle of 42° measured from the normal to the target. The 20 nA primary beam swept a 400×400 μm crater on the target and the secondary ions were sampled from a central crater 60 μm in diameter. Ionized xCs (x=Ga, In, As, P) clusters were selected as the secondary ions, which substantially suppressed the matrix effect during quantitative analysis.[7,8] The ion etching rate was determined by measuring the crater depth using a DEKTAK mechanical profilometer.

A quantitative analysis was made using the relative sensitivity factors $RSF_{xCs^+/InCs^+}$ (x=In, Ga, As, P) normalized to the sensitivity factor for an $InCs^+$ cluster. The relative atomic concentration Cx (M) of species x for steady-state

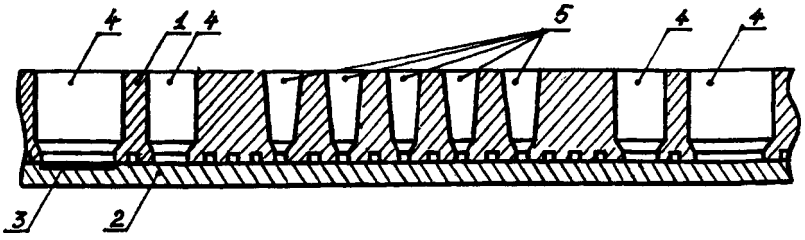

FIG. 1. Schematic of graphite cassette for liquid-phase epitaxy of multiwell laser heterostructures: *1* — fixed framework of cassette, *2* — movable slider, *3* — substrate, *4* — cells for fluxes of waveguide and emitter layers, and *5* — cells for fluxes of quantum-well layers.

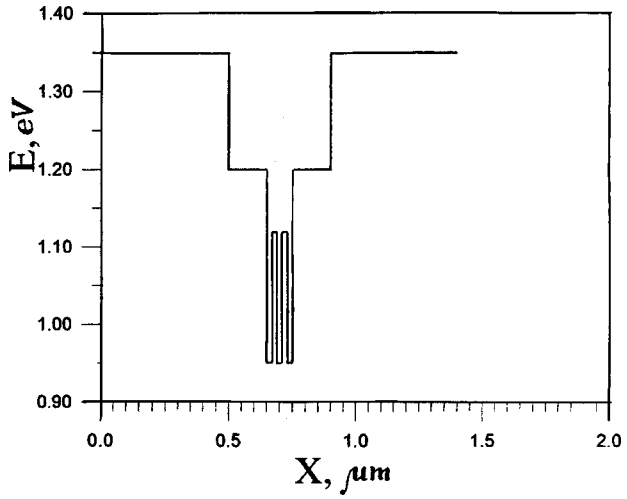

FIG. 2. Schematic band diagram of multiwell laser heterostructure.

sputtering of a matrix with composition M is given by

$$Cx(\mathrm{M})=\frac{I_{x\mathrm{Cs}^+}(\mathrm{M})/\mathrm{RSF}_{x\mathrm{Cs}^+/\mathrm{InCs}^+}(\mathrm{M})}{\Sigma I_{y\mathrm{Cs}^+}(\mathrm{M})/\mathrm{RSF}_{y\mathrm{Cs}^+/\mathrm{InCs}^+}(\mathrm{M})}, \tag{1}$$

where $x, y=$In, Ga, As, P, and $I_{x\mathrm{Cs}^+}(\mathrm{M})$ records the current of ionized $x\mathrm{Cs}^+$ clusters. Then, for an InP matrix, assuming that $C_{\mathrm{In}}=C_{\mathrm{P}}=0.5$, we have

$$\mathrm{RSF}_{\mathrm{PCs}^+/\mathrm{InCs}^+}(\mathrm{InP})=\frac{I_{\mathrm{PCs}^+}(\mathrm{InP})}{I_{\mathrm{InCs}^+}(\mathrm{InP})}. \tag{2}$$

Neglecting in a first approximation the dependence of the relative sensitivity factors on the matrix composition, we obtain the following relation for an M=(In, Ga)(As, P) solid solution:

$$\frac{C_{\mathrm{P}}(\mathrm{M})}{C_{\mathrm{In}}(\mathrm{M})}=\frac{I_{\mathrm{PCs}^+}(\mathrm{M})}{I_{\mathrm{InCs}^+}(\mathrm{M})}\,\frac{I_{\mathrm{InCs}^+}(\mathrm{InP})}{I_{\mathrm{PCs}^+}(\mathrm{InP})}. \tag{3}$$

We shall also assume that the condition for isoperiodicity of the (In, Ga)(As, P) solid solutions in the laser heterostructure imposes an additional relationship between the concentrations C_{In} and C_{P} (Ref. 9):

$$C_{\mathrm{P}}=\frac{1.9378\,C_{\mathrm{In}}-0.5162}{0.9676-0.1244\,C_{\mathrm{In}}}. \tag{4}$$

It can be seen that, when profiling an unstrained laser structure containing an InP layer, the two conditions (3) and (4) allow this to be used as an internal standard, and by measuring only the deviation of the currents of two analytic clusters PCs^+ and InCs^+, it is possible to estimate the depth distribution of all four atomic components.

The composition profile of an InGaAsP/InP laser heterostructure in relative atomic concentrations, measured using this technique, is shown in Fig. 3. The thickness of the epitaxial layers forming the quantum wells is 100–130 Å and the thickness of the intermediate layers is similar. The thickness of the transition layers is of the order of 40–50 Å, which is close to the limiting values for epitaxial layers grown by modified liquid-phase epitaxy.[6] Thus, it is difficult to obtain thinner epitaxial layers of a few tens of angstrom by liquid-phase epitaxy.

The photoluminescence properties of these multiwell heterostructures were also investigated. Figure 4 shows photoluminescence spectra of different types of multiwell heterostructures. In the first type of heterostructure the composition of the semiconducting solid solution in the quantum wells of the active region was the same. In the second type of heterostructure the band gap of the semiconducting solid solution in the quantum wells differed by $\Delta E\cong 15$ meV. In the third type of heterostructures two quantum wells were fabricated for which Eg differed by $\Delta E\cong 30$ meV depending on the composition. The profile of the photoluminescence spectra suggests that quantum wells with different solid-phase compositions are present.

The technique developed to fabricate multiwell heterostructures by liquid-phase epitaxy was used to fabricate laser

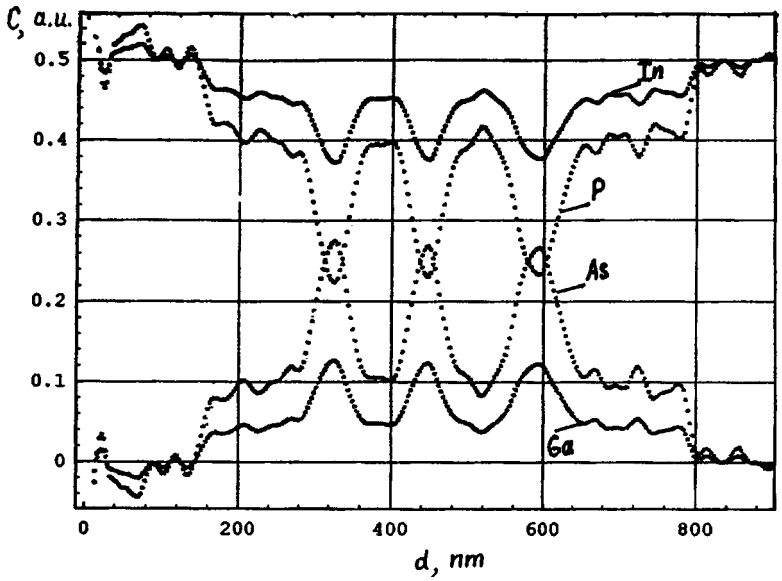

FIG. 3. SIMS profiles of the composition of an In–Ga–As–P multiwell photoluminescence heterostructure (d — etching depth).

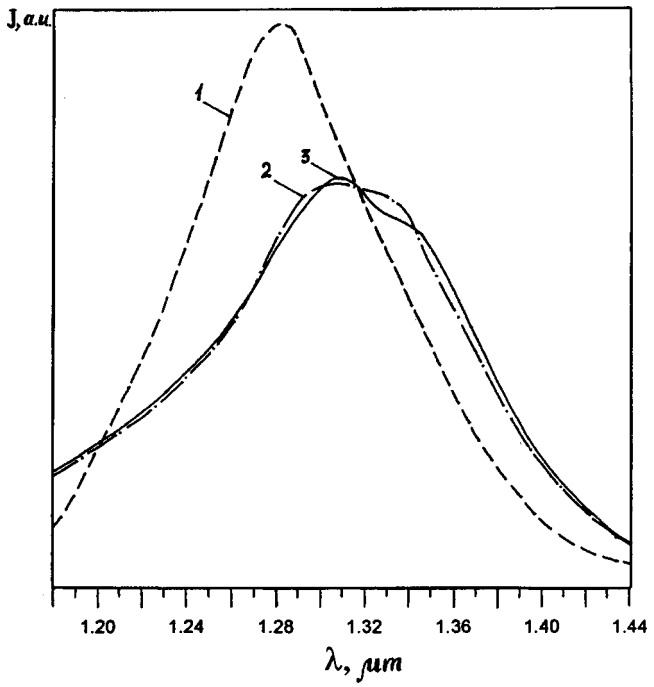

FIG. 4. Photoluminescence spectra of isotypic multiwell heterostructures: *1* — with the same solid-solution composition in the active region, *2* — with the composition differing by $\Delta Eg = 15$ meV, and *3* — differing by $\Delta Eg = 30$ meV.

multiwell heterostructures for which the band gap in the quantum wells was between 0.8 and 0.95 eV. These laser heterostructures were used to fabricate mesastripe lasers by a technique described in detail in Ref. 4. The width of the mesastripe contact was $\sim 5\ \mu$m which ensured lasing in a single zero-order transverse mode. The effective thickness of the active region consisting of three quantum wells was 600 Å. The characteristics of single-mode laser diodes with single active regions have been successfully reproduced in laser diodes formed by structures with lattice-matched epitaxial layers of active region.[4] From this it follows that a design modification of a laser heterostructure with additional heterojunctions inserted does not lead to increased internal optical losses. Thus, this technique developed for liquid-phase epitaxy of multilayer heterostructures can be used to fabricate laser heterostructures with between two and four wells.

To sum up, we have obtained the following results:

1. A technique has been developed to fabricate multiwell InGaAsP/InP heterostructures by liquid-phase epitaxy.

2. Single-mode mesastripe InGaAsP/InP laser diodes have been obtained with a multiwell active region.

The authors are grateful to T. N. Drokina, N. D. Il'inskaya, N. F. Kadoshchuk, and E. A. Kukhareva for assistance with preparing the samples.

This work was supported by Project No. 96-2005 under the Russian National Program ''Physics of Solid-State Nanostructures.''

[1] T. R. Chen, L. E. Eng, Y. H. Zhuang, Y. J. Xu, H. Zaren, and A. Yariv, Appl. Phys. Lett. **57**, 2762 (1990).
[2] C. E. Zah, R. Bhat, B. Pathak, C. Caneau, F. J. Favire, N. C. Andreadakis, D. M. Hwang, M. A. Koza, C. Y. Chen, and T. P. Lee, Electron. Lett. **27**, 1414 (1991).
[3] N. Yokouchi, N. Yamanaka, N. Iwai, and A. Kasukawa, Electron. Lett. **31**, 104 (1995).
[4] M. A. Ivanov, Yu. V. Il'in, N. D. Il'inskaya, Yu. A. Korsakova, A. Yu. Leshko, A. V. Lunev, A. V. Lyutetskiĭ, A. V. Murashova, N. A. Pikhtin, and I. S. Tarasov, Pis'ma Zh. Tekh. Fiz. **21**(5), 70 (1995) [Tech. Phys. Lett. **21**, 198 (1995)].
[5] C. E. Zah, R. Bhat, F. J. Favire, S. G. Yz. Menocal, N. C. Andreadakis, K. W. Cheung, D. M. Hwang, M. A. Koza, and T. P. Lee, IEEE J. Quantum Electron. **27**, 1440 (1991).
[6] Zh. I. Alferov, D. Z. Garbuzov, I. N. Arsent'ev, B. Ya. Ber, L. S. Vavilova, V. V. Krasovskiĭ, and A. V. Chudinov, Fiz. Tekh. Poluprovodn. **19**, 1108 (1985) [Sov. Phys. Semicond. **19**, 679 (1985)].
[7] H. Ghaser and H. Oechner, Fresenius J. Anal. Chem. **341**, 54 (1991).
[8] A. V. Abramov, B. Ya. Ber, N. G. Deryagin, A. V. Merkulov, and D. N. Tret'yakov, Pis'ma Zh. Tekh. Fiz. **21**(3), 34 (1995) [Tech. Phys. Lett. **21**, 103 (1995)].
[9] E. Kuphal, J. Cryst. Growth **7**, 441 (1984).

Translated by R. M. Durham

High-voltage optoelectronic voltage converter using a cascade of tunnel-coupled p^+-i-n^+ diodes

Yu. T. Rebane and Yu. G. Shreter

A. F. Ioffe Physicotechnical Institute, Russian Academy of Sciences, St. Petersburg
(Submitted March 25, 1998)
Pis'ma Zh. Tekh. Fiz. **24**, 68–73 (November 12, 1998)

The idea of a semiconductor electrical voltage converter with optical coupling between the primary and secondary circuits is proposed. Despite its poor efficiency, this converter may prove effective in various specific applications. © *1998 American Institute of Physics.* [S1063-7850(98)01111-2]

The idea of a semiconductor electrical voltage converter with optical coupling between the primary and secondary circuits is proposed. The primary circuit uses a semiconductor light-emitting diode or laser, or arrays of these. The secondary circuit comprises a cascade of p^+-i-n^+ diodes coupled via n^+p^+ tunnel junctions in which only the *i*-regions are illuminated. The voltage multiplication factor for this converter is $\sim N$, where N is the number of p^+-i-n^+ elements in the cascade. The converter output voltage may reach $>10^5$ V with currently attainable degrees of integration. The use of optical coupling allows the secondary and primary circuits to be electrically decoupled and makes the device capable of stepping up voltage over a wide range of frequency $f = 0$–100 MHz with a constant multiplication factor.

The converter is shown schematically in Fig. 1. The primary circuit consists of a semiconductor light-emitting diode or laser, or parallel arrays of these. The secondary circuit comprises a cascade of N vertical p^+-i-n^+-diodes integrated onto a single crystal wafer and connected in series. The primary and secondary circuits are coupled optically.

The converter operates on the following principle. By applying an input voltage to the light-emitting diode, we convert the electrical energy into optical energy, which is then absorbed in the *i* regions of the cascade of p^+-i-n^+-diodes and converted back into electrical energy at a higher voltage. The input voltage V_1 needed to supply the light-emitting diode is of the same order of magnitude as the band gap E_g/e and is 1–10 V depending on the semiconductor used, and the output voltage V_2 will be of order $N\ E_g/e$. Thus, the voltage multiplication factor k_u for this device will be $\sim N$ and at the currently attainable degrees of integration $>10^6$ cm^{-2} may reach $k_u > 10^6$.

The key element in this converter is the secondary circuit, which consists of a voltage step-up cascade of p^+-i-n^+-diodes. An essential feature for the operation of the cascade is the presence of *i*-regions which create asymmetry relative to current reversal in the cascade. This asymmetry is necessary for the operation of a cascade of any elements. Thus, for example, a simple series integration of $p-n$ regions does not step up the voltage in the cascade compared with an individual element. However, it is known that a cascade of series-connected $p-n$ junctions has been used in high-voltage solar cells.[1,2] In this case, the required asymmetry was achieved by means of metal joints between the $p-n$ junctions. The use of these joints is equivalent to connecting the isolated photoelements in series and can yield a fairly high voltage (hundreds of volts[2]). We note, however, that this type of integration produces additional opposing Schottky barriers at the metal contacts, which lowers the operating efficiency of the cascade.

Here we suggest using a cascade of p^+-i-n^+-diodes with highly doped n^+ and p^+ regions. When connected these diodes form low-resistivity n^+p^+ tunnel contacts. When the *i* regions are illuminated, the optically generated electrons and holes are separated by the built-in electric field in the *i*-region and the total current flows from left to right, from n^+ to p^+, in the direction opposite to the applied voltage (Fig. 2b). But in the tunnel junctions the direction of the built-in electric field is opposite to the field in the *i*-region and under illumination, and the current in these junction flows in the direction opposite that in the *i*-regions, reducing the total output voltage of the cascade. In order to ensure efficient operation of the cascade, the n^+ to p^+ regions must be protected from light by means of masks (Fig. 1). The carriers generated in the *i*-regions are pulled by the electric field to the p^+n^+ tunnel junctions and recombine there,

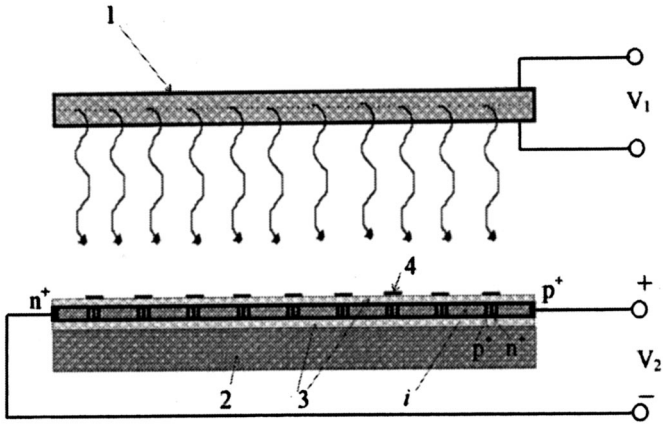

FIG. 1. Schematic diagram of converter: *1* — light source, *2* — substrate, *3* — insulating films, such as SiO_2, and *4* — mask.

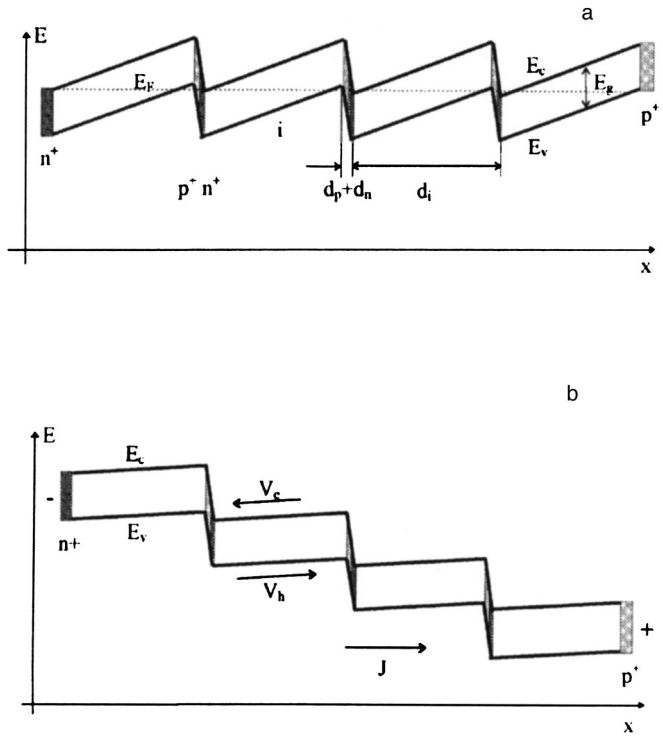

FIG. 2. Energy diagram of device without (a) and with illumination (b): E_c, E_v, and E_g ar the conduction band, valence band, and Fermi level, respectively; d_i, d_n, and d_p are the width of natural region and highly doped n^+- and p^+-regions, respectively; V_e, V_h, and J are the directions of average drift velocities of electrons and holes, and current through the structure, respectively.

thereby closing the complete cascade circuit. The entire cascade must be illuminated uniformly to achieve continuity of the current.

The current–voltage characteristic neglecting carrier recombination in the *i*-regions and the resistivity of the tunnel junctions has the form

$$J = S(\mu_n n_0 + \mu_p p_0)(\varepsilon_g - eV/N)\exp(-\varepsilon_g/kT) \times [\exp(eV/NkT) - 1]/d_i\{1 - \exp[(eV/N - \varepsilon_g)/kT)]\} - e(W\varepsilon_g)\{\{1 + \exp[(eV/N - \varepsilon_g)/kT)]\}/ \{1 - \exp[(eV/N - \varepsilon_g)/kT)]\} - 2kT/(\varepsilon_g - eV/N)\},$$

where n_0 and p_0 are the electron and hole concentrations in the *n*- and *p* regions, μ_n and μ_p are the electron and hole mobilities in the *i*-region, ε_g is the band gap, N is the number of elements in the cascade, d_i and S are the width and cross sectional area of the *i*-region, and W is the power of the radiation incident on the cascade.

Figure 3 gives the calculated current–voltage characteristic of a converter with $N = 10^6$ elements in a silicon cascade. It can be seen that in principle, the converter can produce high voltages up to 8×10^5 V.

The speed τ of the device is determined by the sum of the times, $\tau_1 + \tau_2$, where τ_1 is the carrier separation time in a single *i* region and τ_2 is the tunneling and recombination time in the p^+n^+ junction. Usually τ_1 is much greater than τ_2 and τ can be estimated as $\tau = \tau_1 \sim el^2/\mu E_g = 10^{-(6-8)}$ s, where l is the size of the *i*-region, μ is the carrier mobility in the *i*-region, and E_g is the band gap. Thus, the device can step up voltage in the frequency range $f = 0$–100 MHz with a constant conversion factor.

The efficiency of a real converter is determined by the product of the emitter efficiency, the efficiency of light absorption in the secondary circuit, and the efficiency of carrier

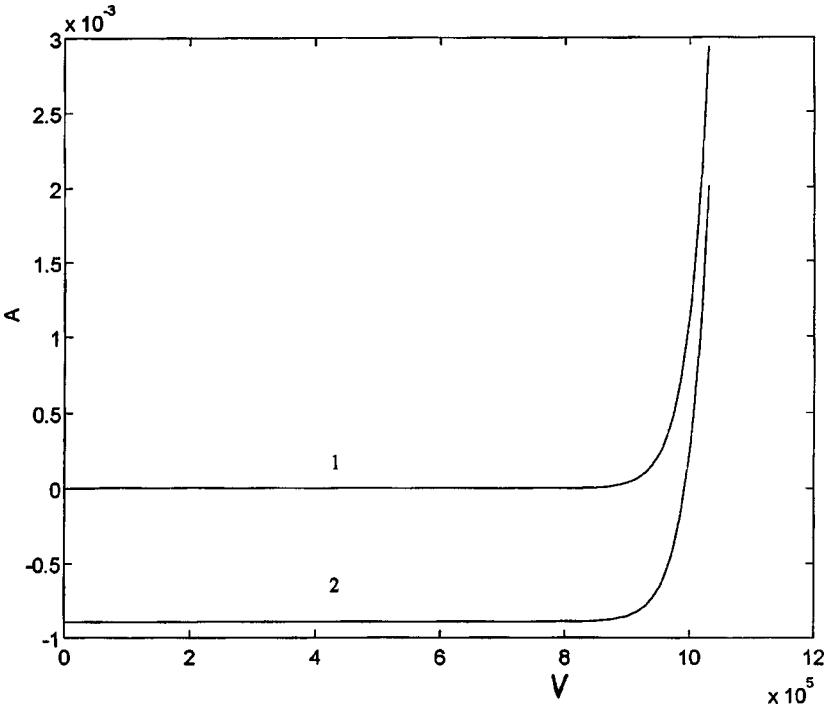

FIG. 3. Current–voltage characteristic of ideal Si cascade: *1* — without irradiation, *2* — with 1 kW irradiation. Cascade parameters: $N = 10^6$, $n_0 = p_0 = 10^{20}$ cm^{-3}, $d_i = 1\,\mu$m, $S = 10^{-8}$ cm^2, $T = 300$ K.

separation in the *i*-regions. A preliminary analysis of various methods of implementing this device suggests an efficiency of order 5%. One possible method involves using silicon films insulated from the substrate by SIMOX technology in the secondary circuit and using light-blue GaN light-emitting diodes to reduce the light absorption path.

Despite its low efficiency, this voltage converter may have various specific applications, such as in physics experiments, portable high-voltage detectors for ionizing radiation, interference-free fiber-optic fuel ignition devices for rockets and aircraft, and also in electronic ignition devices for cars.

This work was partially supported by the Russian Fund for Fundamental Research (Project No. 96–02–17825) and by the Program ''Physics of Solid-State Nanostructures'' (Project No. 1001).

[1] E. A. Andryushin and A. P. Silin, Usp. Fiz. Nauk **161**(8), 129 (1991) [Sov. Phys. Usp. **34**, 705 (1991)].
[2] A. P. Landsman and D. S. Strebkov, Fiz. Tekh. Poluprovodn. **4**, 1922 (1970) [Sov. Phys. Semicond. **4**, 1647 (1970)].

Translated by R. M. Durham

Influence of nonuniformity of the ion background on the oscillation frequency of a virtual cathode

V. G. Anfinogentov and A. E. Khramov

''Kolledzh'' State Educational-Scientific Center, Saratov State University
(Submitted May 12, 1998)
Pis'ma Zh. Tekh. Fiz. **24**, 74–80 (November 12, 1998)

The oscillation frequency of a virtual cathode in a diode gap is investigated as a function of the density of the anode ion layer. It is shown that when the densities of the ion layer are high, a stable electron bunch forms in the flux, which leads to an increase in the oscillation frequency. © *1998 American Institute of Physics.* [S1063-7850(98)01211-7]

It has been established that the generation of electromagnetic oscillations in a virtual cathode device (vircator) is caused by two mechanisms, that is to say, oscillations of electrons in the ''cathode–virtual cathode'' nonlinear potential well and oscillations of the virtual cathode as a single entity.[1–4] Suppression of the first mechanism as a result of electrons reflected from the virtual cathode being transferred from the interaction space back to the injection plane[1,5] can improve the quality of the spectrum and the efficiency of conversion of the flux energy into microwave radiation in the vircator. The frequency of the virtual cathode oscillations is determined by the plasma frequency $\omega_p=(\rho_0 e/m_e\epsilon_0)^{1/2}$ of the electron flux on entering the interaction space,[2–4,6,7] where ρ_0 is the unperturbed space charge density of the flux, e and m_e are the electron charge and mass, respectively, and ϵ_0 is the dielectric constant. Kadish, Faehl, and Snell[8] give the following estimate of the virtual cathode oscillations as a single entity:

$$1.93<\omega/\omega_p<2.31.$$

It is conventionally assumed that the oscillation frequency of a virtual cathode can only be varied by varying the frequency ω_p of the electron flux.

Here we consider a simple model of a virtual cathode–diode system penetrated by a multienergy electron flux with supercritical current. The grids confining the system are equipotential. Inside the system the density of the fixed ion background is distributed very nonuniformly, occupying a region near the injection plane (anode plasma). The control parameters of the system are the Pierce parameter

$$\alpha=\omega_p\frac{L}{v_0},$$

which is proportional to the injected beam current if L and v_0 are fixed, the ratio of the anode plasma density ρ_p to the space charge density ρ_0 of the electron beam, $n=\rho_p/\rho_0$, and the thickness of the anode plasma layer x_p (in this study x_p is fixed and $x_p/L=0.25$). Here L is the length of the interaction space and v_0 is the unperturbed flux velocity. When $\alpha>\alpha_{cr}$ holds, the single-flux state of the flux becomes unstable with respect to small perturbations of the charge density and a virtual cathode forms in the system.[9] Note that in the limiting cases $x_p/L=1$, $n=1$ (classical Pierce diode) we find $\alpha_{cr}=\pi$ (Ref. 10) and $n=0-\alpha_{cr}=4/3$ (Ref. 9).

This system is of considerable interest in connection with the possibility of describing the flux dynamics in microwave devices such as a plasma-anode vircator.[11] We note that the approximation of a fixed ion background quite satisfactorily describes the effects taking place in this system

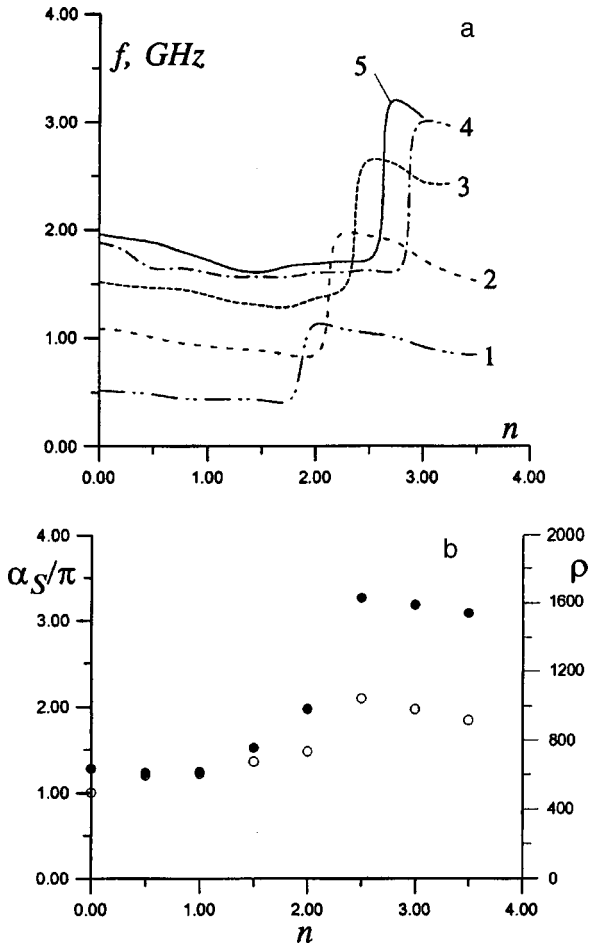

FIG. 1. a — Oscillation frequency versus ion layer density n for various beam currents α: *1* — $\alpha=0.75$, *2* — $\alpha=1.20$, *3* — $\alpha=1.75$, *4* — $\alpha=2.13$, *5* — $\alpha=2.25$: b —effective value of Pierce parameter α_S (●) and space charge density $\overline{\rho(n)}$ (○) versus ion layer density n.

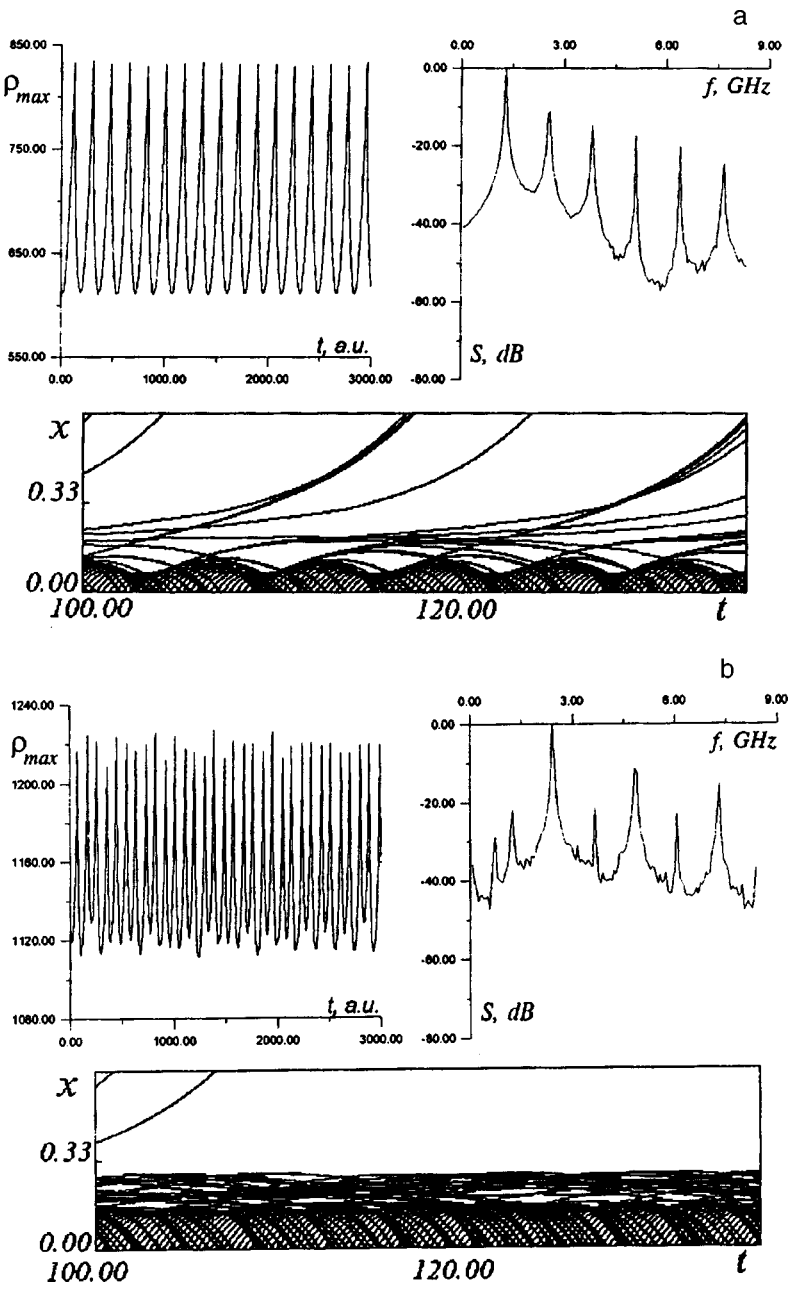

FIG. 2. Oscillations of maximum space charge density in drift space, power spectrum of electric field oscillations, and space–time diagram of electron flux for conditions with low ion layer density $n=0.25$ (a) and high ion layer density $n=2.5$ (b) for $\alpha=1.375$.

since the ion mass is $m_i \gg m_e$. The nuclear mass of hydrogen, for example, is $\approx 1800\ m_e$ so that the time over which the ion concentration becomes significantly perturbed is fairly long, amounting to approximately 150–200 periods of the virtual cathode oscillations, which is greater than the current pulse duration. It is difficult to obtain an analytic description of the nonsteady-state processes in this system because of the detours and reflections of the charged particles, and so we used a particle simulation to analyze the processes.[12]

Figure 1a gives the oscillation frequency of the system as a function of the plasma density parameter n for various values of the beam current α. It can be seen that at low anode plasma densities the oscillation frequency varies very negligibly. This variation is caused by a change in the effective value of the flux plasma frequency ω_p as the density of the anode plasma increases. As the beam current α increases, we observe an increase in the oscillation frequency since ω_p increases with increasing α (we assume that v_0 and L are constant).

When the density of the ion background reaches a certain value $n_{cr}(\alpha)$, the oscillation frequency shows an approximately twofold jump compared with the frequency in a diode with the same current and $n=0$. It can be seen from Fig. 1a that as the frequency increases, the critical density n_{cr} increases with α. Note that at high beam currents the system goes over to stochastic oscillations with a continuous spectrum as α increases. For small α the system is transferred to a state of complete transmission with a highly nonuniform charge density distribution.

This increase in the oscillation frequency in the flux may be explained by analyzing the physical processes in the interaction space. In the first regime with a low base frequency in the spectrum, i.e., $n<n_{cr}(\alpha)$, the flux has only one elec-

tron bunch or virtual cathode and the dynamics of the system differs little from the case when $n=0$ (see Ref. 13). The oscillation frequency of the virtual cathode is determined by the plasma frequency ω_p and the motion in the system is nearly regular (Fig. 2a).

The situation changes drastically when the density of the anode ion layer is high. In this case, as a result of the highly nonuniform plasma filling of the region $0<x<x_p$, we observe a buildup of particles frozen near the virtual cathode. A stable, continuously existing, fairly high-density bunch forms in the flux which can be clearly identified on the space–time diagram (Fig. 2b). This bunch is formed of particles which remain in the interaction space for several periods of the virtual cathode oscillations and then quit the interaction space. Figure 1b shows the increase in the time-averaged space charge density $\overline{\rho}$ in the diode gap as a function of n. It can be seen that as the density of the anode plasma layer increases, the charge accumulated in the interaction space for $n>2.25$ is approximately twice that for $n=0$. The oscillation frequency in the flux with a virtual cathode is determined by the growth rate of the electrostatic instability, which in turn depends on the effective Pierce parameter α_S. An increase in α_S increases the oscillation frequency of the virtual cathode. We calculated the parameter α_S near the virtual cathode and the results are plotted in Fig. 1b. For low n we find $\alpha_S=\alpha$, although an increase in n leads to an increase in α_S. The curve $\alpha_S(n)$ reveals a steeper jump at $n\sim 2-2.5$ compared with $\overline{p}(n)$. This is because as the space charge density increases, the flux is slowed more substantially near the virtual cathode and thus the parameter $\alpha_S\sim\sqrt{\rho}/\langle v\rangle_t$ increases.

To sum up, when a highly nonuniform ion background is present in a system with a virtual cathode, a secondary electron bunch forms, promoting the buildup of space charge near the virtual cathode. This strongly influences the growth rate of the electrostatic instability which determines the formation of the virtual cathode, so that the oscillation frequency of the system can increase.

This work was supported by the Russian Fund for Fundamental Research, Grant No. 98–02–16541.

[1] H. A. Davis, R. R. Bartch, T. J. T. Kwan *et al.*, Phys. Rev. Lett. **62**, 75 (1987).
[2] A. N. Didenko, Dokl. Akad. Nauk SSSR **321**, 727 (1991) [Sov. Phys. Dokl. **36**, 844 (1991)].
[3] T. J. T. Kwan and L. E. Thode, Phys. Fluids **27**, 1570 (1984).
[4] S. C. Burkhart, R. D. Scarpetti, and R. L. Lundberg, J. Appl. Phys. **58**, 28 (1985).
[5] H. A. Davis, R. R. Bartsch, T. J. T. Kwan *et al.*, IEEE Trans. Plasma Sci. **16**, 192 (1988).
[6] A. N. Didenko, and V. I. Rashchikov, Fiz. Plazmy **18**, 1182 (1992) [Sov. J. Plasma Phys. **18**, 616 (1992)].
[7] T. Lin, W. Chen, W. Liu *et al.*, J. Appl. Phys. **68**, 2038 (1990).
[8] A. Kadish, R. J. Faehl, and C. M. Snell, Phys. Fluids **29**, 4192 (1986).
[9] *High Power Microwave Sources*, edited by V. L. Granatstein and I. Alexeff (Artech House, Boston, 1987), Chap. 13.
[10] J. Pierce, J. Appl. Phys. **15**, 721 (1944).
[11] V. D. Selemir, B. V. Alekhin, V. E. Vatrunin *et al.*, Fiz. Plazmy **20**, 689 (1994) [Plasma Phys. Rep. **20**, 621 (1994)].
[12] C. K. Birdsall and A. B. Langdon, *Plasma Physics via Computer Simulation* (McGraw-Hill, New York, 1985; Énergoatomizdat, Moscow, 1989, 452 pp.).
[13] V. G. Anfinogentov, in *Proceedings of the Fifth International Specialist Workshop on Nonlinear Dynamics of Electronic Systems, NDES'97*, Moscow, 1997, p. 284.

Translated by R. M. Durham

In situ examination of the chemical etching of SiO_2–Si structures using an atomic force microscope

A. A. Bukharaev, A. A. Bukharaeva, N. I. Nurgazizov, and D. V. Ovchinnikov

E. K. Zavoĭskiĭ Physical-Technical Institute, Kazan Science Center, Russian Academy of Sciences
(Submitted May 7, 1998)
Pis'ma Zh. Tekh. Fiz. **24**, 81–86 (November 12, 1998)

First results are reported of *in situ* visualization of the chemical etching of P^+-ion implanted SiO_2–Si structures in an aqueous HF solution using an atomic force microscope. The rates of SiO_2 etching were determined and the kinetics of the photostimulated chemical etching of Si were investigated. © *1998 American Institute of Physics.* [S1063-7850(98)01311-1]

An atomic force microscope (AFM) can be used for direct measurements in a liquid.[1] This opens up fundamentally new possibilities for studying physicochemical processes at a liquid–solid interface. By systematically obtaining *in situ* images of the same section of a surface, we can observe the transformation of a solid surface during etching or dissolution in real time.

Here we use this method for the first time to make an *in situ* study of the etching of SiO_2–Si structures in an aqueous HF solution, which is of particular interest since this is one of the main technological processes in microelectronics.

We developed a cell for operation in an HF solution using an atomic force microscope consisting of a P4-SPM-MDT probe microscope with a $15\times 15\ \mu$m scanning field. In this cell the microprobe (cantilever) of the microscope is completely immersed in the liquid which covers the surface of the sample. The liquid is situated between the sample and quartz glass with a thin transparent film which prevents the glass from being damaged by the acid. The aqueous solutions contained HF concentrations between 0.1 and 3%,

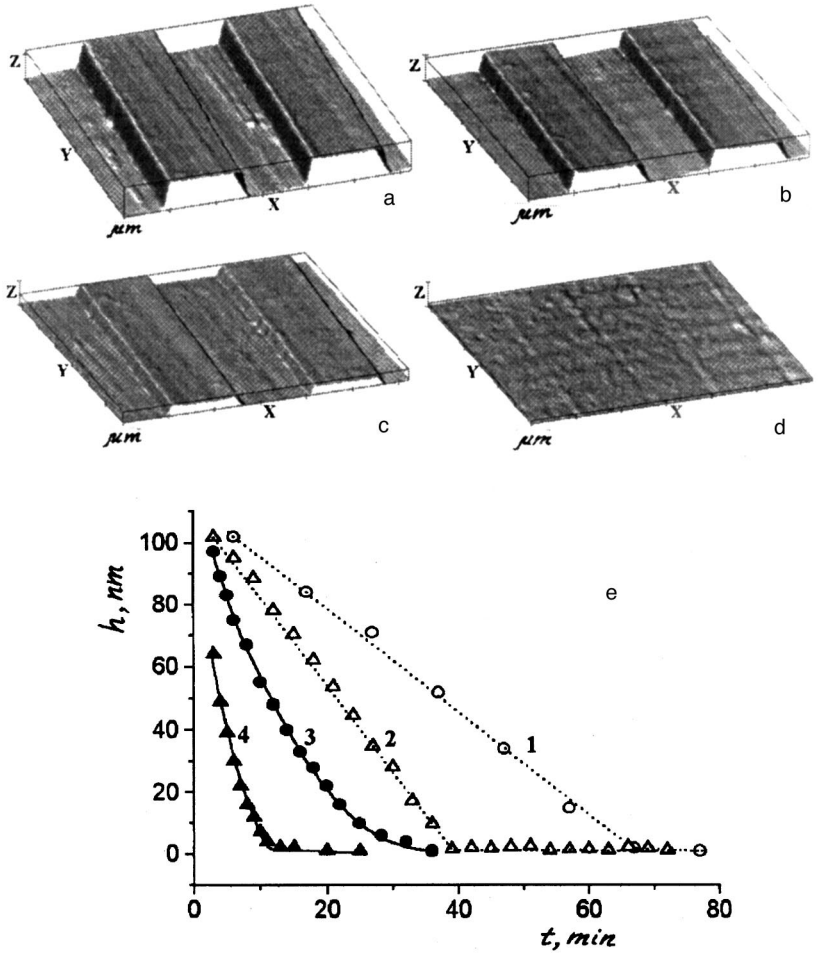

FIG. 1. Etching of SiO_2 in aqueous HF solution: time from beginning of etching in 0.25% solution — 4 (a), 25 (b), 45 (c), and 75 min (d); scale of AFM images *X*, *Y*: 1 μm, *Z*: 0.1 μm; e — kinetics of etching of initial (*1*, *2*) and implanted (*3*, *4*) SiO_2 in 0.25% (*1*, *3*) and 0.5% HF solution (*2*, *4*) (*h* — step height, *t* — etching time).

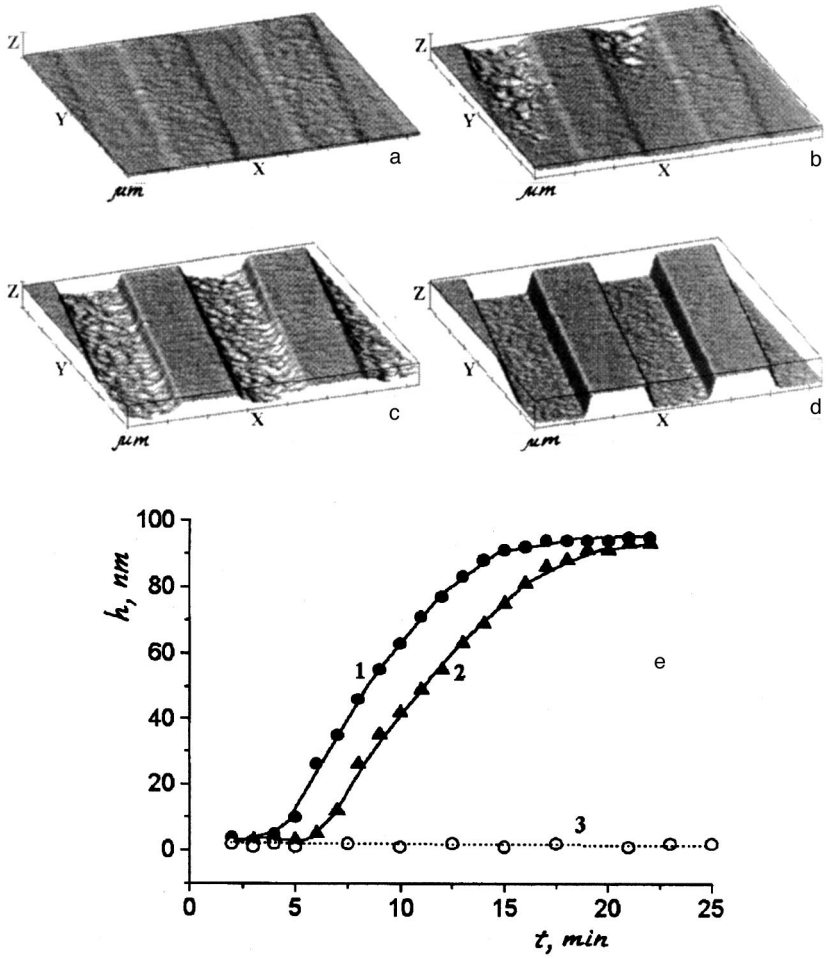

FIG. 2. Photostimulated etching of *a*Si in 0.5% aqueous HF solution: time from beginning of etching — 2 (a), 7 (b), 13 (c), and 23 min (d); scale of AFM images *X*, *Y*: 1 μm, *Z*: 0.1 μm; e — etching kinetics of *a*Si on exposure to light of different intensity (*1*, *2*) and without light (*3*).

which barely damaged the tip of the Si_3N_4 cantilever. The vertical deflection of the microscope cantilever was recorded from the deflection of a semiconductor laser beam (670 nm, 1 mW) reflected from the cantilever arm.[2] By positioning the laser beam at the end of the arm where the cantilever tip is located, we can ensure that some of the laser radiation is incident on the scanned section of surface.

The samples were cut from an *n*-Si(100) wafer with resistivity 4.5 $\Omega \cdot$cm on which a structure with a period of 3 μm was formed by photolithography, consisting of separate SiO_2 stripes 0.1 μm high and 1.5 μm wide distributed over the Si. The samples were bombarded with 40 keV P^+ ions in an ILU-3 ion accelerator at a dose of 10^{15} ions/cm^2, which exceeds the amorphization threshold of silicon.

Figures 1a–1e show AFM images of the same section of an initial unimplanted structure with protruding SiO_2 stripes, obtained systematically at different times from the beginning of etching in a 0.25% HF solution. This series of images clearly shows that the SiO_2 protrusions disappear almost completely with time. The absence of any step at the SiO_2–Si interface at the end of the experiment confirms the well-known fact that an aqueous HF solution barely dissolves the surface of crystalline silicon.[3] This allowed us to measure the absolute height of the SiO_2 protrusion during the etching process to within 2 nm and thus obtain data on the SiO_2 etching kinetics, which are plotted in Fig. 1e. The step height could be determined by recording only a few profiles across the structure so that the time taken for a single measurement did not exceed a few seconds. Curves 1 and 2 in Fig. 1e show that the rate of etching of unimplanted SiO_2 is almost constant, being 1.6 and 2.8 nm/min, respectively, for the 0.25% and 0.5% HF solution.

For the samples implanted with P^+ ions (curves *3* and *4* in Fig. 1e), the rate of SiO_2 etching was initially more than three times higher than that for the unirradiated sample. After the SiO_2 thickness had decreased to 20–40 nm, the rate of etching was appreciably lower. This behavior is attributable to the distribution of radiation defects in the implanted layer,[4] whose maximum depth of occurrence is determined by the maximum projected range of the P^+ ions in SiO_2 (approximately 70 nm for our case[5]). All these data were obtained when the laser radiation of the microscope vertical displacement detector was not incident on the scanned part of the sample.

After the SiO_2 etching process had been completed, the surface of the implanted sample was almost planar (Fig. 2a) and consisted of periodically distributed regions of crystalline (*c*Si) and amorphous silicon (*a*Si). The *c*Si sections are located at the sites of the etched SiO_2 stripes which prevented the P^+ ions from entering the silicon, and are interspersed with *a*Si regions amorphized by implantation. It is known[3] that unlike *c*Si, *a*Si dissolves in HF, although the

sample would need to be held for several days in a 3% HF solution to obtain 90 nm deep grooves (90 nm is the *a*Si thickness at the doses and implantation energies used[5]). It was found that if the laser radiation acts on the scanned section of the sample during etching, the *a*Si is etched many times faster (Fig. 2e). Moreover, as a result of the nonuniform distribution of the laser radiation intensity, the growth rate of the steps at the *c*Si–*a*Si interface differs in different parts of the scanning field. The curves plotted in Fig. 2e are in fact a continuation of curve 4 in Fig. 1, where curves 1 and 2 were obtained when the surface was exposed to light of different intensity and curve 3 was obtained without illumination. Judging by the profile of curves 1 and 2 and the height of the relief, we postulate that the change in the rate of *a*Si etching under the action of light (relative to *c*Si) is caused by the distribution of implanted *P* atoms in the silicon. Figures 2b and 2c show that on exposure to light, *a*Si is etched nonuniformly with the formation of a porous structure.

In *ex situ* control experiments using LG-78 He–Ne laser radiation (2 mW, 633 nm), photostimulated etching of *a*Si in a 0.5% HF solution with the formation of 90 nm high steps occurred within 6 min at a laser power density of 0.3 W/cm^2. Similar experiments involving laser irradiation of unimplanted SiO_2–Si structures showed that light also stimulates chemical etching of *c*Si. The *in situ* measured kinetics of this process were more complex since the photostimulated etching of *c*Si was also accompanied by dissolution of SiO_2. The AFM images showed that after the silicon has been exposed to light for 50 min (after the SiO_2 had completely dissolved), a porous structure forms with a highly developed microrelief.

To sum up, the proposed method can be used to study the kinetics of chemical etching processes in real time and to observe the transformation of the surface of multiphase structures induced by ion and laser irradiation.

This work was supported by the Russian Fund for Fundamental Research (Grant No. 98–03–32753) and by the programs ''Physics of Solid-State Nanostructures'' (Grant No. 96–1034) and ''Promising Technologies and Devices in Microelectronics and Nanoelectronics'' (Grant No. 02.04.143).

[1] B. Drake, C. B. Prater, A. L. Weisenhorn *et al.*, Science **243**, 1586 (1988).
[2] A. A. Bukharaev, D. V. Ovchinnikov, and A. A. Bukharaeva, Zavod. Labor. No. 5, 10 (1997).
[3] K. A. Valiev, T. M. Makhviladze, and A. V. Rakov, Mikroelektronika **15**, 392 (1986).
[4] K. A. Valiev, V. A. Danilov, K. A. Drakin *et al.*, Mikroelektronika **11**, 323 (1982).
[5] H. Ryssel and I. Ruge, *Ion Implantation* (Wiley, New York, 1986; Nauka, Moscow, 1983, 360 pp.).

Translated by R. M. Durham

Investigation of the nature of low-frequency fluctuations of the field emission current using a two-dimensional distribution function*

S. S. Gots, R. R. Gallyamov, and R. Z. Bakhtizin

Bashkir State University, Ufa
(Submitted April 27, 1998)
Pis'ma Zh. Tekh. Fiz. **24**, 87–93 (November 12, 1998)

A two-dimensional distribution function in the frequency range 0.03–1 Hz was used to investigate the statistical characteristics of the fluctuations of the field emission current from single crystals of tungsten and *p*-type silicon. In order to determine the type of nonlinearity predominating in the low-frequency noise of the emission current, calculations were made of the two-dimensional distribution function for a Gaussian random process subjected to a given type of nonlinear transformation and the profiles of the experimental two-dimensional distribution functions were compared with dependences obtained by numerical methods. It was established that fluctuations of the effective emitting surface of the cathode, the barrier transmission, the work function, and of the electric field strength near the emitter surface may act as primary sources of low-frequency noise in the field emission current.
 [S1063-7850(98)01411-6]

One of the undesirable effects accompanying field emission is the variability of the emission parameters of field-emission cathodes. The main contribution to the instability of the emission current is made by the low- and ultralow-frequency components of the noise, whose mechanism has not yet been fully clarified.

An analysis of studies of the nature of $1/f$ noise in field emission devices published so far suggests that the primary sources of $1/f$ noise include fluctuations of the following physical quantities: the work function, electric field strength near the cathode surface, transmission of the potential barrier, effective surface area of the emitter, or the number of emission centers. All these parameters of the emission process are taken into account analytically in the form of arguments of the Fowler–Nordheim equation,[1] which describes the nonlinear dependence between the field emission current density and the quantities F, φ, a, and b:

$$j(F,\varphi,a,b)=aF^2\exp\left(-\frac{b\varphi^{3/2}}{F}\right). \tag{1}$$

Each of the arguments F, φ, a, and b of Eq. (1) expresses a specific nonlinear dependence which differs from the others. Thus, in order to determine the sources of $1/f$ noise, it would be advisable to use methods which could identify the nature of the electrical nonlinearity of the noise. The constructiveness of this approach may at first glance seem illusory, since an investigation of the nature of the nonlinearity is no less involved that studying the nature of the $1/f$ noise itself. Suffice it to say that the use of conventional spectral[2] and correlation[3] methods of analysis for $1/f$ noise does not give the desired result.

A key direction in solving the problem of $1/f$ noise could involve using a multidimensional statistical analysis, which would provide a more comprehensive description of fluctuation processes.[4] In earlier studies of the statistics of $1/f$ noise of the field emission current using graphs of a two-dimensional distribution function, we observed characteristic sections associated with a nonlinear transformation of the primary Gaussian noise.[5,6] This indicates that a two-dimensional distribution function is sensitive to the nature of the nonlinear processes in field emitters.

Here we use numerical methods of measuring the two-dimensional distribution function, which for one-dimensional processes are, by definition, the combined probability density $W/[i(t),i(t-\tau)]$ of two arguments:[4] the noise current $i(t)$ and the noise current delayed by time τ, $i(t-\tau)$. The sampling size was 10^5–10^7 measurements. A 128×128 matrix was used to map the distribution function. In the modeling process the primary δ-correlated noise signal with Gaussian statistics was formed by summing random numbers with equally probable statistics obtained using a random number generator. To test the combined instrumental and program system, we made measurements for a Gaussian random process obtained using a G2-57 noise generator.

During studies of $1/f$ noise in field emission devices, we observed three types of fluctuations: quasicontinuous, single pulses against a continuous noise background, and packets of pulses. We showed[5] that pulse fluctuations lead to the so-called multitude type of two-dimensional distribution function, whereas continuous fluctuations correspond to a unitary type of distribution.

The results of measurements of the distribution of the emission current fluctuations from *p*-type silicon (Fig. 1a) and tungsten (Fig. 1b) show that the unitary type of two-dimensional distribution function exhibits characteristic deviations from a normal distribution law, in the form of asymmetry relative to the peak, which shows up as regions of nonzero probability in the direction of increasing arguments and localized along the coordinate axes. Unlike *p*-type silicon (Fig. 1a), the regions of nonzero values of the two-

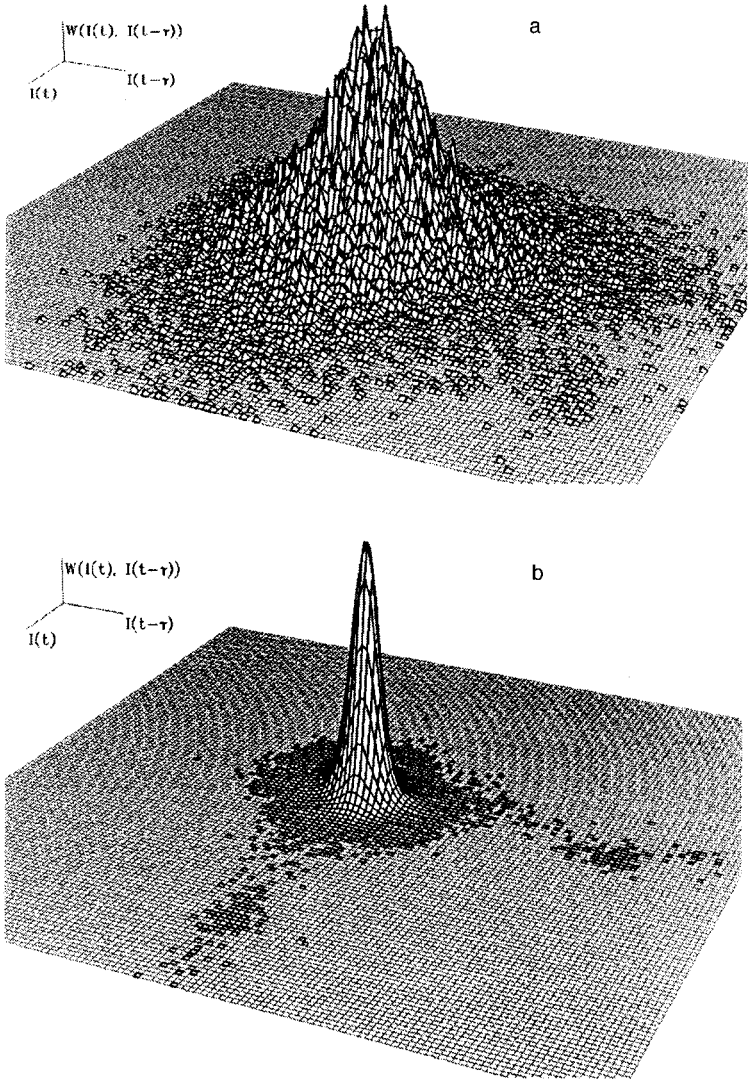

FIG. 1. Experimentally determined two-dimensional distribution functions of low-frequency fluctuations of the field emission current: a — for *p*-type silicon, b — for tungsten.

dimensional distribution function for a tungsten single crystal are more extended but narrower (Fig. 1b), which we attributed previously to the appearance of nonlinear effects.[6] For the simulation we used the dependence (1) as the most natural form of the nonlinear transformation of primary Gaussian noise for metal and semiconducting field emitters. Note that the nonlinear dependence for $j(a,b,F,\varphi)$ is only preserved for the last three arguments, although it was important to ensure continuity of the function $H(X(t))$, which describes the nonlinear transformation of the fluctuation process $X(t)$. This situation arose because in order to obtain a function with a particular profile, it was necessary to use two regions of variation of the argument and two analytic functions which determine the form of $H(X(t))$.

For the fluctuating parameter b the function $H(b)$ consisted of a linear function set which changes to exponential,

$$H(b)=\begin{cases} b, & b\leqslant 0, \\ \text{const}\,1\times\left[\exp\left(\dfrac{b}{\text{const}\,1}\right)-1\right], & b>0. \end{cases} \tag{2}$$

For the nonlinear transformations $H(F)$ of the electric field fluctuations $F(t)$ and $H(\varphi)$ of the work function fluctuations $\varphi(t)$, it was necessary to use the sum of linear and exponential dependences

$$H(F)=\begin{cases} F, & F\leqslant 0, \\ F+a\,F^2\exp\left(-\dfrac{\text{const}\,2}{F}\right), & F>0; \end{cases} \tag{3}$$

$$\begin{cases} \varphi, & \varphi\leqslant 0, \\ \varphi+a\exp\left(-\dfrac{\varphi^{3/2}}{\text{const}\,3}\right), & \varphi>0. \end{cases} \tag{4}$$

From the point of view of the physical mechanism for the occurrence of the fluctuations, the difference between the forms of Eqs. (3) and (4) compared with Eq. (2) may be explained by the fact that the fluctuations $F(t)$ and $\varphi(t)$ are local, whereas the fluctuations of the barrier transmission $b(t)$ embrace to the complete emitting surface of the cathode. Thus, the equivalent electrical circuits (3) and (4) com-

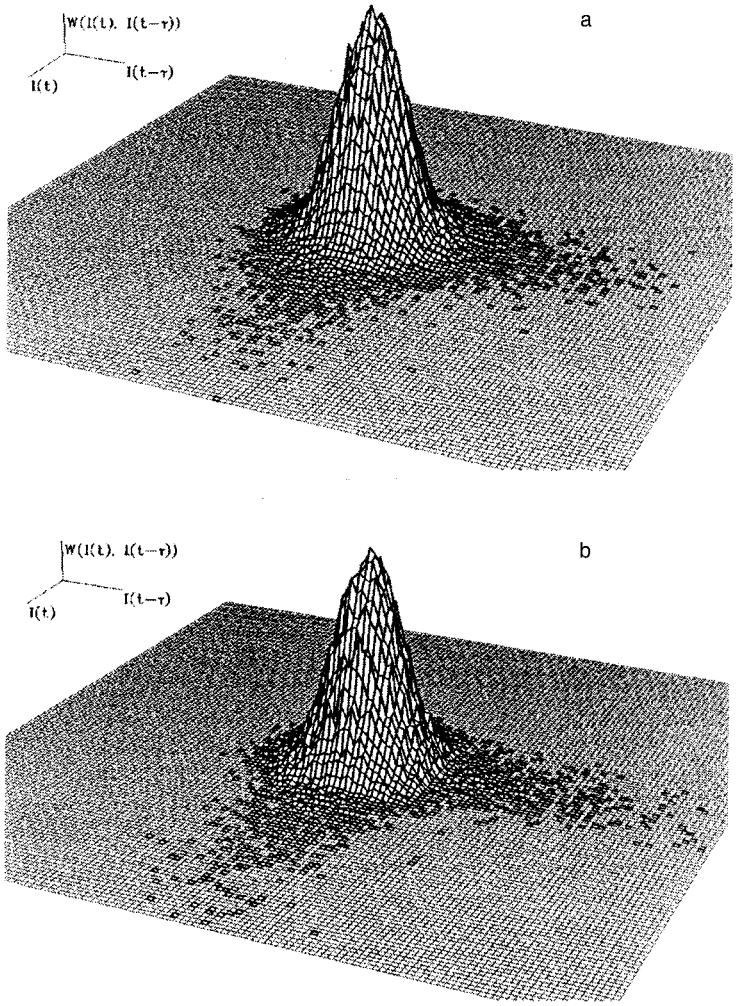

FIG. 2. Two-dimensional distribution functions calculated numerically for a system with different Fowler–Nordheim nonlinear transfer characteristics $H[X(t)]$ for a normal type of primary fluctuation process: a — using the nonlinear characteristics $H(F)$ for the fluctuations of the field strength F; b — using the nonlinear characteristic $H(\varphi)$ for the fluctuations of the work function φ.

prise a parallel-connected linear resistance (corresponding to the nonfluctuating part of the emitter at a given time) and a nonlinear resistance (its fluctuating part).

Figure 2 gives the results of calculations of the two-dimensional distribution function obtained for nonlinearity of type (3) and (4), respectively, and a comparison shows that they agree to within statistical error. A similar two-dimensional distribution function was obtained for (2) nonlinearity of the type (2). By varying the values of const 1, const 2, and const 3, we can obtain regions of nonzero values of the distribution function extending to any length in the direction of increasing values of the arguments. In particular, by using each of the dependences (2)–(4), we obtained values of the two-dimensional distribution function exactly corresponding to the experimental curves for *p*-type silicon (a) and tungsten (b). Thus, any of the nonlinear dependences can transform the statistics of a Gaussian random process into a form characteristic of the statistics of the field emission current fluctuations. At present, we are working on using the two-dimensional distribution function to obtain quantitative estimates of the relative contribution of the fluctuations of the nonlinear components caused by fluctuations of the field at the surface of the emitter, the work function, and the barrier transparency.

This work was partly supported by the Federal Program ''Surface Atomic Structures'' of the Ministry of Science and Technology of the Russian Federation (Project No. 96–2.27).

*Paper presented at the International Conference on Emission Electronics, Tashkent, Republic of Uzbekistan, 4–6 November 1997.

[1] A. Modinos, *Field, Thermionic, and Secondary Electron Emission Spectroscopy* (Plenum Press, New York, 1984), 375 pp.
[2] T. Kawakubo and T. Kobayashi, in *Proceedings of the 13th Conference on Noise in Physical Systems and 1/f Fluctuations*, Vilnius, 1996, p. 263.
[3] F. N. Hooge and P. A. Bobbert, Physica B **239**, 223 (1997).
[4] V. I. Tikhonov, *Statistical Radio Engineering* [in Russian], Radio i Svyaz', Moscow (1982), 624 pp.
[5] S. S. Ghots and R. Z. Bakhtizin, in *Proceedings of the Conference on Noise in Physical Systems and 1/f Fluctuations*, Leuven, Belgium, 1997, p. 609.
[6] S. S. Gots and R. Z. Bakhtizin, in *Proceedings of Scientific and Technical Seminar on Noise and Degradation Processes in Semiconductor Devices*, Moscow, 1997 [in Russian], p. 86.

Translated by R. M. Durham

Analytic model of the current–voltage characteristic of a small probe in a magnetic field

V. A. Rozhanskiĭ and A. A. Ushakov

St. Petersburg State Technical University
(Submitted May 15, 1998)
Pis'ma Zh. Tekh. Fiz. **24**, 1–10 (November 26, 1998)

An analytic model is proposed for a small wall probe (whose dimensions perpendicular to the magnetic field are smaller than the ion Larmor radius) in a completely ionized plasma. The structure of the current collection regions is described and an analytic expression is obtained for the current–voltage characteristic of the probe. It is shown that a model with a classical diffusion coefficient gives results close to the experimental values. © *1998 American Institute of Physics.* [S1063-7850(98)01511-0]

1. INTRODUCTION

Electrostatic probes are widely used to determine the plasma parameters in nuclear fusion facilities. Nevertheless, the theory of a probe in a magnetic field is still far from completion. Despite numerous theoretical and experimental studies, various questions still have not been answered, such as the absence of saturation of the ion and electron branches of the current–voltage characteristic, the dependence of the current on voltage in the transition section of the probe characteristic, and the relatively low ratio of the saturation electron and ion currents compared with $(m_i/m_e)^{1/2}$. Here we propose an analytic model which describes the electron branch of the current–voltage characteristic of a small probe in a completely ionized plasma in a magnetic field. We assume that the transverse dimension of the probe is smaller than the ion Larmor radius ρ_{ci} (the opposite case of a large probe was considered in Ref. 1) but larger than the electron Larmor radius ρ_{ce}. We show that the saturation electron current is given by the Bohm formula with a classical transverse diffusion coefficient. The results of calculations using the proposed analytic formula for the transition section of the current–voltage characteristic agree with the results of numerical modeling by Sanmartin.[2] The fact that no saturation of the electron-branch current is observed experimentally can be attributed to an increase in the thickness of the space charge layer near the probe. The analytic model shows reasonable agreement with the experimental results obtained on the TdeV tokamak.[3]

2. MODEL

We shall analyze a homogeneous plasma of density n_0 and temperature $T_e=T_i=T$ in a magnetic field B. For simplicity, we initially consider the case of cylindrical symmetry when the magnetic field is perpendicular to a circular wall probe of radius a (Fig. 1). (The case of an inclined magnetic field will be considered subsequently in similar fashion). A positive voltage is applied to the probe relative to the surrounding walls. The wall potential is taken to be zero and the probe potential will be denoted by φ_p.

When the plasma is completely ionized, we can adopt an approach similar to that used for a weakly ionized plasma[4] (see also Ref. 2). Similar ideas are also discussed in Ref. 5. When the probe is positively charged, it collects electrons and the plasma density is reduced in an ellipsoidal zone having characteristic dimensions a and $l_\parallel$ perpendicular and parallel to the magnetic field, respectively. Since the probe radius a is smaller than the Larmor radius of the ions, they can move freely perpendicular to the magnetic field substantially faster than the electrons. Thus, the ions should be trapped in the electron ellipsoid, i.e., the electric field should be balanced by the ion pressure gradient, and a Boltzmann distribution is established for the ions

$$\varphi=-\frac{T_i}{e}\ln\frac{n}{n_0}+\varphi_f, \tag{1}$$

where φ_f is the plasma potential. The electron flux density $\mathbf{\Gamma}_e=n\mathbf{u}_e$ can be obtained from the force balance equation

$$-\nabla p_e+en\nabla\varphi-en\mathbf{u}_e\times\mathbf{B}+\mathbf{R}_{ei}=0, \tag{2}$$

where $\mathbf{R}_{ei}$ is the frictional force between the electrons and the ions:

$$\mathbf{R}_{ei}=-knm_e\nu_{ei}(\mathbf{u}_e-\mathbf{u}_i). \tag{3}$$

The numerical coefficient has values $k=0.51$ and $k=1.0$ parallel and perpendicular to the magnetic field, respectively. From Eqs. (1)–(3) we obtain expressions for the density of the longitudinal electron flux $\mathbf{\Gamma}_{e\parallel}$ and the transverse electron flux $\mathbf{\Gamma}_{e\perp}$:

$$\mathbf{\Gamma}_{e\parallel}=\Gamma_{i\parallel}-D^*_{e\parallel}\frac{\partial n}{\partial z},\quad \mathbf{\Gamma}_{e\perp}=-D_{e\perp}\nabla_\perp n, \tag{4}$$

where $D^*_{e\parallel}=(T_e+T_i)/(0.51m_e\nu_{ei})$ is the effective longitudinal coefficient of electron diffusion, $D_{e\perp}=(T_e+T_i)\nu_{ei}/(m_e\omega_{ce}^2)$ is the classical transverse coefficient of electron diffusion, and ω_{ce} is the electron cyclotron frequency. The effective longitudinal coefficient of electron diffusion is inversely proportional to the plasma density n, whereas the transverse diffusion coefficient is directly proportional to n. Substituting Eq. (4) into the equation of continuity for the electrons $\nabla\cdot\mathbf{\Gamma}_e=0$, we obtain

$$\frac{1}{r}\frac{\partial}{\partial r}\left(rD_{e\perp}\frac{\partial n}{\partial r}\right)+\frac{\partial}{\partial z}\left(D^*_{e\parallel}\frac{\partial n}{\partial z}-\Gamma_{i\parallel}\right)=0. \tag{5}$$

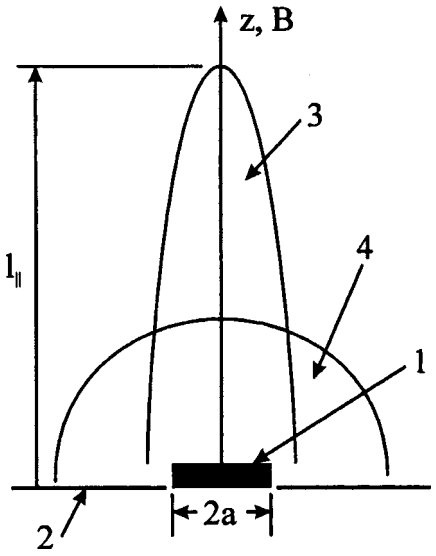

FIG. 1. Structure of electron and ion current collection regions: *1* — probe, *2* — wall, *3* — electron collection region, and *4* — ion collection region.

Neglecting the divergence of the longitudinal ion flux, which is permissible outside the ion collection zone at distances from the probe greater than ρ_{ci}, we obtain

$$\frac{1}{r}\frac{\partial}{\partial r}\left(r\frac{n}{n_0}\frac{\partial n}{\partial r}\right)+\frac{\omega_{ce}^2}{0.51v_{ei}^2(n_0)}\frac{\partial}{\partial z}\left(\frac{n_0}{n}\frac{\partial n}{\partial z}\right)=0. \tag{6}$$

Equation (6) is similar to that solved numerically in Ref. 2 and yields an expression for the characteristic longitudinal dimension of the electron ellipsoid

$$l_\parallel=a(\omega_{ce}/v_{ei}). \tag{7}$$

If the electron current to the probe is lower than the saturation electron current, the longitudinal potential profile in the plasma should be nonmonotonic (Fig. 2). This effect is known as ''overlap.''[2,4] In most of the electron ellipsoid the potential profile corresponds to a Boltzmann distribution for the ions (1). The potential in this region increases from the plasma potential φ_f at infinity to its maximum φ^*, which is related to the plasma density n^* at this point

$$\varphi^*=-(T_i/e)\ln(n^*/n_0)+\varphi_f. \tag{8}$$

Near the probe, however, there must be a region where the electrons are trapped, since their flux must be less than thermal. Consequently, in this region the potential profile should correspond to the Boltzmann distribution for the electrons and should therefore decrease on approaching the probe. The electron flux to the probe can be expressed in terms of the potential difference $\varphi^*-\varphi_p$

$$\Gamma_{e\parallel}=n^*\sqrt{\frac{T_e}{2\pi m_e}}\exp\left(-\frac{e(\varphi^*-\varphi_p)}{T_e}\right). \tag{9}$$

Then, substituting the maximum of the potential φ^* (8) into Eq. (9), we obtain

$$-\frac{T_i}{e}\ln\left(\frac{n^*}{n_0}\right)-\frac{T_e}{e}\ln\left(\frac{n^*}{\Gamma_{e\parallel}}\sqrt{\frac{T_e}{2\pi m_e}}\right)=\varphi_p-\varphi_f. \tag{10}$$

Most of the electron current I_e to the probe is collected far from the probe where the plasma density is weakly perturbed. Thus, the nonlinear equation (6) may be replaced by the corresponding linear one (Laplace equation)

$$\frac{1}{r}\frac{\partial}{\partial r}\left(r\frac{\partial n}{\partial r}\right)+\frac{D_{e\parallel}^*(n_0)}{D_{e\perp}(n_0)}\frac{\partial^2 n}{\partial z^2}=0. \tag{11}$$

The problem may be solved analytically by imposing the boundary condition $n=n^*$ at the surface of the probe (thus neglecting the longitudinal dimension of the ion ellipsoid compared with the longitudinal dimension of the electron ellipsoid). In this linearized case, the electron current I_e should be a linear function of the plasma density n^* at the layer boundary

$$\frac{n^*}{n_0}=1-\frac{I_e-I_i(n^*)}{I_e^{\rm sat}}. \tag{12}$$

We shall assume that the ion current to a positively charged probe corresponds to the Bohm current with the plasma density n^*: $I_i=en^*c_sS_{\rm probe}=I_i^0n^*/n_0$, where $c_s=((T_e+T_i)/m_i)^{1/2}$ is the ion acoustic velocity and $S_{\rm probe}$ is the projective area of the probe parallel to the magnetic field. The electron current to the probe is $I_e=e\Gamma_{e\parallel}S_{\rm probe}$. The saturation electron current $I_e^{\rm sat}$ is calculated by solving the Laplace equation (11) with zero boundary conditions at the probe surface, similar to the case of a weakly ionized plasma:[6]

$$I_e^{\rm sat}=k2\pi en_0\sqrt{D_{e\parallel}^*D_{e\perp}}C=k2.8\pi en_0\rho_{ci}c_sC,$$

$$\rho_{ci}=c_s/\omega_{ci}. \tag{13}$$

The nonlinearity of the initial equation (6) is taken into account by introducing a coefficient k of order unity. The function C is a geometric factor determined by the size and shape of the probe and corresponds to the capacitance of a conductor of the same shape as the probe but whose longitudinal dimension is $(D_{e\parallel}^*/D_{e\perp})^{1/2}$ times shorter. For the most interesting cases the value of C can be obtained analytically. For a disk probe of radius a the coefficient is $C=2a/\pi$. When the magnetic field forms an angle α with the wall, the collection of the current is determined by the projection of the probe parallel to the magnetic field. For a disk probe this projection is an ellipse with the semiaxes a and $b=a\sin\alpha$. The corresponding value of C is

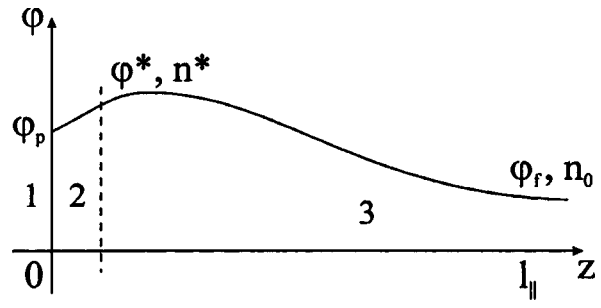

FIG. 2. Potential distribution parallel to magnetic field: *1* — probe, *2* — space charge layer, and *3* — electron collection region.

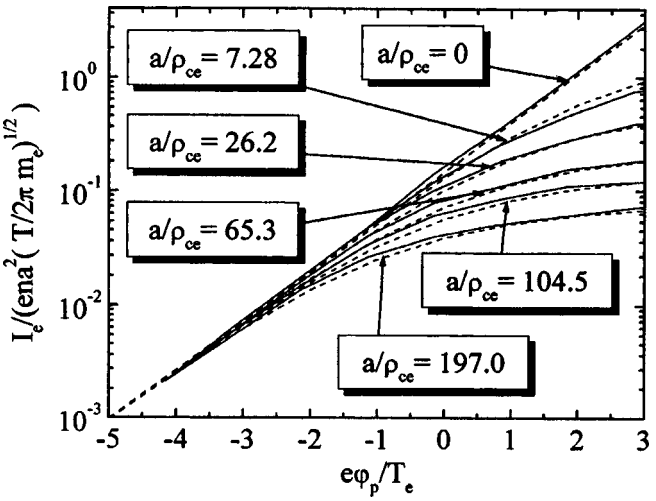

FIG. 3. Electron current at probe I_e versus applied potential φ_p ($\varphi_p=0$ when the probe potential is equal to the wall potential) for various magnetic fields. Results of the numerical model of Sanmartin[2] (dashed curves) are compared with those obtained by an analytic solution of the proposed model (15) (solid curves).

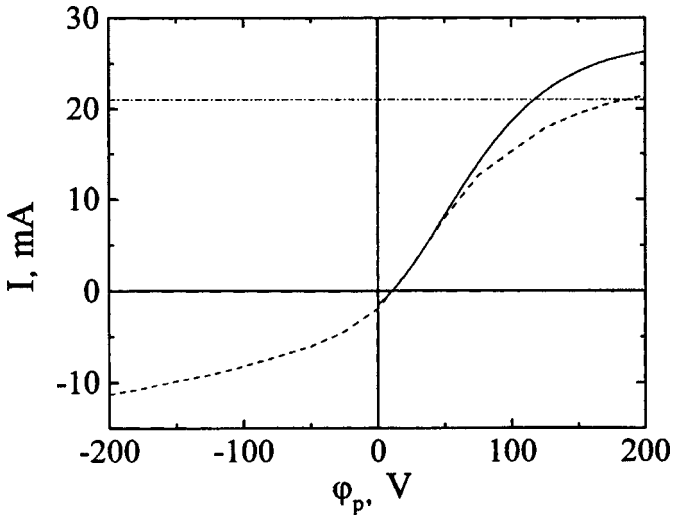

FIG. 4. Comparison between the experimental probe characteristic obtained for the TdeV tokamak (dashed curve) and results of an analytic solution of the proposed model (15), (16) (solid curve). The dot-dash line gives the maximum attainable electron current $I_e^{\lim}$.

$$C=\frac{a}{K(\sqrt{1-b^2/a^2})}, \quad K(\xi)=\int_0^{\pi/2}\frac{d\varphi}{\sqrt{1-\xi^2\sin^2\varphi}}. \quad (14)$$

An expression for the transition section of the current–voltage characteristic is obtained by substituting Eq. (12) into Eq. (10)

$$\left(1-\frac{I_e}{I_e^{\rm sat}}\right)^2\frac{en_0S_{\rm probe}}{I_e}\sqrt{\frac{T}{2\pi m_e}} =\left(1-\frac{I_i^0}{I_e^{\rm sat}}\right)^2\exp\left(\frac{e(\varphi_f-\varphi_p)}{T}\right). \quad (15)$$

In Fig. 3 the probe characteristics obtained from Eq. (15) are compared with a numerical solution of the nonlinear problem[2] for the case $a=b$. (Since an isolated probe rather than a wall probe is considered in Ref. 2, the saturation current $I_e^{\rm sat}$ given by Eq. (13) should be doubled). We show that good agreement is achieved for a numerical coefficient $k=0.7$ over a wide range of magnetic field.

For a magnetic field almost parallel to the wall ($\alpha\ll 1$), expression (13) can be simplified ($k=0.7$)

$$I_e^{\rm sat}=2\pi en_0\rho_{ci}c_s\frac{a}{K(\sqrt{1-b^2/a^2})} \approx en_0\rho_{ci}c_s\frac{2\pi a}{\ln(4\sqrt{2}/\sin\alpha)}. \quad (16)$$

Figure 4 shows the electron branch of the current–voltage characteristic calculated using Eqs. (15) and (16), and the experimental probe characteristic obtained using the TdeV tokamak.[3] This experiment has the parameters $B=1.4\,\mathrm{T}$, $\alpha=3°$, $a=0.95\,\mathrm{mm}$, the temperature calculated from the exponential section is $T^{\rm stand}=27\,\mathrm{eV}$, and the plasma density obtained from the saturation ion current $n^{\rm stand}=3.6\times10^{18}\,\mathrm{m}^{-3}$. The solid curve in Fig. 4 was obtained from Eq. (15) where the temperature was selected so that the experimental and theoretical curves agreed over most of the transition section. The plasma density was recalculated from the saturation ion current for the temperature thus obtained. Our method gives $T=24\,\mathrm{eV}$ and $n=4.0\times10^{18}\,\mathrm{m}^{-3}$. The corresponding saturation electron current is $I_e^{\rm sat}=27\,\mathrm{mA}$.

The proposed simple model can be refined by taking into account the following factors.

1. For probe potentials substantially higher than the plasma potential the electrons is the layer may no longer be trapped. Thus, Eq. (9) is no longer valid and should be replaced by the condition that the electron flux is equal to the thermal flux. Consequently, expression (15) for the electron branch of the current–voltage characteristic only holds for currents lower than $I_e^{\lim}=I_e^{\rm sat}/(1+(I_e^{\rm sat}-I_i^0)/I_e^T)<I_e^{\rm sat}$ ($I_e^T=S_{\rm probe}en_0\sqrt{T_e/2\pi m_e}$). At high applied potentials the electron current I_e is simply equal to $I_e^{\lim}$. For plasma and probe parameters for which $I_e^{\lim}$ is substantially less than $I_e^{\rm sat}$, the saturation electron current is reduced accordingly as a result of this effect. The maximum attainable electron current $I_e^{\lim}$ is also plotted in Fig. 4 (dot-dash curve).

2. For high positive probe potentials the thickness of the space charge layer d depends on the potential drop in the layer $d\sim r_d(e\varphi_p/T)^{3/4}$. The effective collecting area of the probe therefore increases. (For the case $\alpha\ll1$, for instance, for high probe potentials the minor semiaxis of the ellipse should be taken to be d rather than b). This effects leads to the absence of saturation of the electron current $I_e^{\rm sat}$ and $I_e^{\lim}$.

3. CONCLUSIONS

An analytic model has been proposed for a wall probe having dimensions perpendicular to the magnetic field much smaller than the ion Larmor radius. We have shown that a model with a classical diffusion coefficient gives results close to the experimental ones.

The authors are grateful for the support of the Russian Fund for Fundamental Research (Grant No. 96–02–16919-a), St. Petersburg State University (Grant No. 97–0–5.3–17), and the Ministry of Science and Technology of the Russian Federation (Subprogram ''Controlled Nuclear Fusion and Plasma Processes,'' Grant No. 377).

[1] V. Rozhansky, A. Ushakov, and S. Voskoboynikov, Contrib. Plasma Phys. **36**, 391 (1996).

[2] J. R. Sanmartin, Phys. Fluids **13**, 103 (1970).

[3] J. P. Gunn, C. Boucher, B. L. Stansfield, C. S. MacLatchy, Contrib. Plasma Phys. **36**, 45 (1996).

[4] V. A. Rozhanskiĭ and L. D. Tsendin, Zh. Tekh. Fiz. **48**, 1647 (1978) [Sov. Phys. Tech. Phys. **23**, 932 (1978)].

[5] P. C. Stangeby, J. Phys. D **15**, 1007 (1982).

[6] D. Bohm, in *The Characteristics of Electrical Discharges in Magnetic Fields*, edited by A. Guthrie and R. Wakerling (McGraw-Hill, New York, 1949), Chaps. 1, 2, and 9.

Translated by R. M. Durham

Optical excitation of surface waves and photopiezoelectric resonance in a photorefractive crystal

M. P. Petrov, A. P. Paugurt, V. V. Bryksin, and V. M. Petrov

A. F. Ioffe Physicotechnical Institute, Russian Academy of Sciences, St. Petersburg
(Submitted June 15, 1998)
Pis'ma Zh. Tekh. Fiz. **24**, 11–16 (November 26, 1998)

Resonant optical excitation of surface waves of a photorefractive crystal (BSO) was observed for the first time when a hologram was recorded by an oscillating interference pattern. The vibrations of the surface relief observed are caused by oscillation of the space charge field and the inverse piezoelectric effect. © *1998 American Institute of Physics.*
[S1063-7850(98)01611-5]

Photorefractive crystals exhibit both electrooptic and piezoelectric effects. Thus, holographic recording in these media with the formation of an electric field grating is accompanied not only by variations of the refractive index but also by deformations in the sample. As a result, if the crystal is suitably cut, a periodic surface relief appears, which may be regarded as a reflection hologram, since the surface displacements in the linear approximation should be linearly related to the interference pattern of the light incident on the crystal. This type of hologram was observed experimentally for the first time in a photorefractive crystal under static conditions in $Bi_{12}TiO_{20}$ (Ref. 1) and a theoretical analysis of the surface relief for uniaxial crystals was made in Refs. 2 and 3. Stepanov *et al.*[4] used two-wave mixing for the first time to record the diffraction of light from this type of hologram in $Bi_{12}SiO_{20}$ with two coherent beams used for recording, one of which was periodically phase-modulated.

Here we also recorded a hologram when one of the beams was phase-modulated, but in addition to recording the two-wave mixing involving the first negative diffraction order, we also observed the first diffraction order, which is phase-reversed (phase-conjugate) with respect to the appropriate recording beam. Recording the phase-conjugate wave allows us to directly record the frequency dependence of the crystal surface waves and to determine whether surface waves, including photopiezoelectric resonance, are present.

The apparatus is shown schematically in Fig. 1. The holographic gratings were recorded by beams A_S and A_R with the phase of beam A_R modulated using an electrooptic modulator. The light source was a Compass-200, $\lambda = 530$ nm laser with a 200 mW output power. The measurements were made using a (110)-cut $Bi_{12}SiO_{20}$ crystal and an electric field E_0 was applied along the [001] axis. The front and rear faces of the crystal were nonparallel so that the beams reflected from these faces could be clearly separated.

If the photodetector was positioned at (●)1, the two-wave mixing signal was recorded (the reflected beam A_s plus the first negative order diffraction of the beam A_R). If the photodetector was positioned at (●)2, the first positive diffraction order was recorded for the reflected beam. We note that the complex amplitude of the beam diffracted at (●)2 is $A_{S2} = \sqrt{\eta A_S^*}$, where $\sqrt{\eta}$ is the diffraction efficiency, i.e., A_{S2} is the phase conjugate of A_S.

When the photodetector was positioned at (●)3 or (●)4, the two-wave mixing signal and the phase-conjugate beam were recorded, respectively, but in a transmission geometry, i.e., as a result of diffraction at the refractive index grating. Figure 2 gives the output signals as a function of the modulation frequency $\Omega/2\pi$ for the phase-conjugate beams in transmission geometry I_4 and reflection geometry I_2. The dependence of these signals on the external field E_0 is cubic.

To make a quantitative theoretical analysis, we need to analyze the so-called Kukhtarev equations,[5] which describe the formation of an electric charge and field grating in a photorefractive crystal and the elastodynamics equations[6] allowing for the contribution of the piezoelectric effect. Here we shall confine ourselves to a qualitative interpretation of the results.

It is known[7] that the amplitude of an electric field grating for a hologram recorded by the drift mechanism involving a phase-modulated beam, and also assuming that the contrast of the interference pattern m is low and the amplitude of the phase modulation θ is low, has the form

$$E_{SC}(t) = -mE_0(1 + F' + iF''), \tag{1}$$

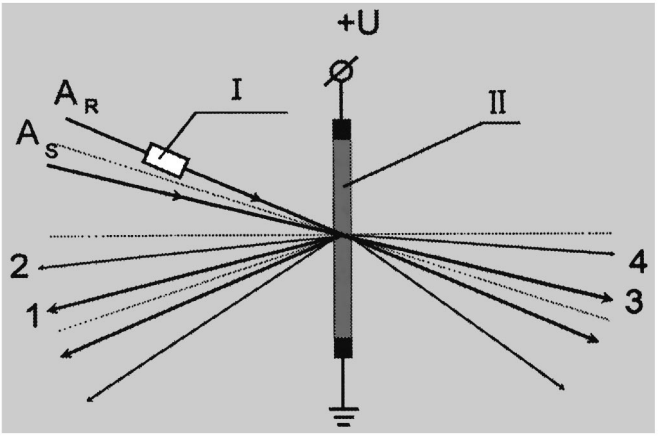

FIG. 1. Experimental geometry: I — electrooptic modulator, II – $Bi_{12}SiO_{20}$ crystal.

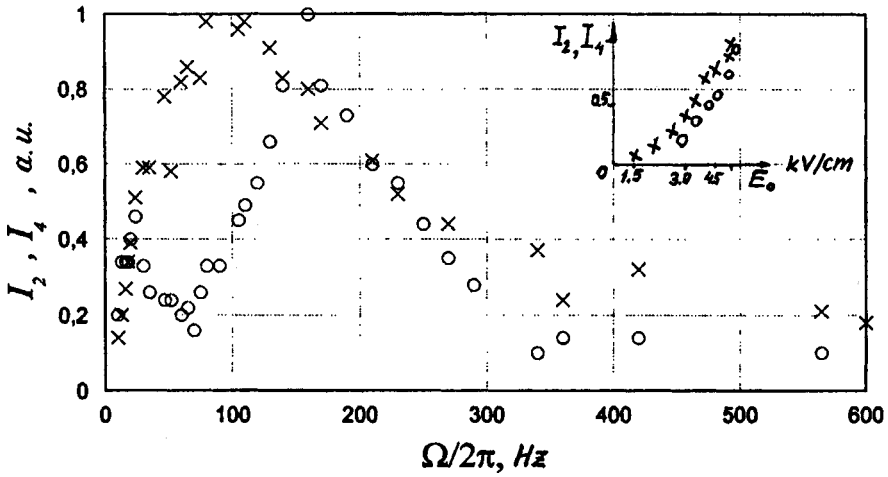

FIG. 2. Dependence of I_2 and I_4 on the phase modulation frequency: $\theta \approx 0.8$ rad, $m \approx 0.5$. The intensity of the light incident on the crystal is approximately 400 mW/cm^2, $\Lambda = 27\ \mu$m. The inset gives the dependence of I_2 and I_4 on the external field at frequencies corresponding to resonance. All the data are given in arbitrary units and the absolute values of I_2 are approximately two orders of magnitude lower than I_4: I_2 — ○, I_4 — ×.

$$F' = \frac{\theta g d \cos(\Omega t + \gamma)}{\sqrt{1 + 2g^2(1-d^2) + g^4(1+d^2)^2}}; \tag{2}$$

here $d = KL_0$, $K = 2\pi/\Lambda$, where Λ is the period of the interference pattern, L_0 is the carrier drift velocity ($L_0 \propto E_0$), γ is the phase which depends on Ω, $g = \Omega \tau_M$, τ_M is the Maxwellian relaxation time, and an expression for F'' is given in Ref. 7. We find that to within terms of order θ^2,

$$I_4 = I_S \Phi(r_{ij}) m^2 E_0^2 F', \tag{3}$$

where $\Phi(r_{ij})$ is a coefficient which depends on the electrooptic tensor r_{ij}, and I_S is the intensity of the S beam. However, we can assume that since the surface deformations are linearly related to the electric grating field $E_{SC}(t)$, we have

$$I_2 = I_S R_0^2 m^2 E_0^2 |(D(0) + D(\Omega)F' + iD(\Omega)F'')|^2. \tag{4}$$

Here R_0 is the amplitude reflection coefficient, $D(0)$ and $D(\Omega)$ are coefficients which depend on the piezoelectric constant, the elastic constants, the grating period for zero frequency, and Ω, respectively. In general, $D(\Omega)$ can be a complex quantity. Then, to within terms of order θ^2 we have

$$I_2 = I_S R_0^2 m E_0^2 D(0)(\mathrm{Re}\, D(\Omega)F' - \mathrm{Im}\, D(\Omega)F''). \tag{5}$$

Here Re and Im denote the real and imaginary parts of $D(\Omega)$, respectively.

We know from Ref. 7 that F' has a maximum at the frequency $\Omega = \Omega_r = 1/\tau_M(d^2+1)^{1/2}$ (for $m \ll 1$) and F'' has a maximum for $\Omega = 0$, if $d \ll 1$, and for $\Omega = \Omega_r$, if $d \gg 1$.

A comparison of the experimental dependence of I_2 and I_4 suggests that the maxima near 90 and 160 Hz are associated with the maximum of the function F' (and possibly F'' for I_2).

The mechanism responsible for these maxima can be explained qualitatively as follows.

When a photorefractive crystal is illuminated by two beams, one of which is phase-modulated, the interference pattern oscillates near its equilibrium position at frequency Ω. These oscillations of the interference pattern cause corresponding oscillations of the space charge grating. If the frequency Ω is close to the natural frequency of the space charge waves Ω_r (Refs. 7 and 8), the space charge waves, and hence the waves of the electric field grating and the photorefractive waves, are amplified, which is recorded using beam I_4. Since the field $E_{SC}(t)$ undergoes resonant amplification, the amplitude of the surface waves also has a maximum as a result of the inverse piezoelectric effect. Thus, a maximum should be observed for I_2 at the same frequency as for I_4.

This mechanism also describes the cubic dependence of I_2 and I_4 on the external field. However, the I_2 maximum is shifted experimentally relative to the I_4 maximum by 70 Hz. This may be caused by the frequency dependence $D(\Omega)$ and by the different value of τ_M near the surface and in the bulk of the crystal, since τ_M depends on (is inversely proportional to) the intensity of the recording light and this intensity is highly nonuniform over the crystal thickness because of absorption. In some experiments we observed an additional maximum for the I_2 beam at frequencies near 500–600 Hz, which may be attributed to the natural vibrations of the surface layer of the sample. The resonance maxima observed for the reflected beam I_2 may be described as photopiezoelectric resonance, since they occur as a result of the resonant optical excitation of surface waves in the crystal caused by the piezoelectric effect.

[1] A. M. Bliznetsov, M. P. Petrov, and A. V. Khomenko, Pis'ma Zh. Tekh. Fiz. **10**, 1094 (1984) [Sov. Tech. Phys. Lett. **10**, 463 (1984)].
[2] S. M. Shandarov, Zh. Tekh. Fiz. **56**, 583 (1986) [Sov. Phys. Tech. Phys. **31**, 352 (1986)].
[3] S. M. Shandarov and V. M. Shandarov, Zh. Tekh. Fiz. **60**(2), 106 (1990) [Sov. Phys. Tech. Phys. **35**, 199 (1990)].
[4] S. Stepanov, N. Korneev, A. Gerwens, and K. Buse, Appl. Phys. Lett. **72**, 879 (1998).
[5] N. M. Kukhtarev, V. B. Markov, S. G. Odulov, M. S. Soskin, and V. L. Vinetsky, Ferroelectrics **22**, 949 (1979).
[6] Yu. I. Sirotin and M. P. Shaskol'skaya, *Principles of Crystal Physics* [in Russian], Nauka, Moscow (1979).
[7] M. P. Petrov, V. M. Petrov, V. V. Bryksin, I. Zouboulis, A. Gerwens, and E. Kraetzig, Opt. Lett. **22**, 1083 (1997).
[8] R. F. Kazarinov, R. A. Suris, and B. I. Fuks, Fiz. Tekh. Poluprovodn. **6**, 572 (1972) [Sov. Phys. Semicond. **6**, 500 (1972)].

Translated by R. M. Durham

Photoluminescence of II–IV–V_2 and I–III–VI_2 crystals passivated in a sulfide solution

V. N. Bessolov, M. V. Lebedev, V. Yu. Rud', and Yu. V. Rud'

A. F. Ioffe Physicotechnical Institute, Russian Academy of Sciences, St. Petersburg; State Technical University, St. Petersburg

(Submitted March 19, 1998)
Pis'ma Zh. Tekh. Fiz. **24**, 17–22 (November 26, 1998)

An investigation was made to determine how chemical treatment of the surface of II–IV–V_2 and I–III–VI_2 semiconductor crystals (such as $CdSiAs_2$, $ZnSnP_2$, $CuGaSe_2$, and r-$AgInS_2$) using a solution of ammonium sulfide in *tert*-butyl alcohol influences their photoluminescence properties. It is shown that the photoluminescence intensity is enhanced substantially after treatment with the spectral profile and energy position of the band peaks remaining unchanged. © *1998 American Institute of Physics.* [S1063-7850(98)01711-X]

The ternary semiconducting compounds II–IV–V_2 and I–III–VI_2, being structural and electronic analogs of the III–V and II–VI semiconductors, have recently started to be actively used in photoconverter technology. It is known that the surface properties of semiconductors exert an appreciable influence on the characteristics of optoelectronic devices. The development of methods of modifying the electronic properties of the surface is thus an important problem.

The electronic properties of the surface of III–V semiconductors are actively modified by sulfide passivation, which involves treating the semiconductors with sulfide-containing solutions or gases. Sulfide passivation of a semiconductor surface substantially reduces the surface recombination rate, which enhances the photoluminescence intensity[1] and improves various characteristics of many semiconductor devices.[2–5] The use of low-permittivity alcohols as solvents to prepare the sulfide solutions can also substantially enhance the passivation efficiency of a GaAs surface[6] and of InGaAs/AlGaAs laser mirrors.[7]

Nelson *et al.*[8] recently showed that treatment of the surface of $CuInSe_2$ (a chalcopyrite) using an aqueous solution of ammonium sulfide leads to passivation of the surface states and weakens the anchoring of the Fermi surface level.

In order to achieve more efficient electronic passivation, we treated the surface of II–IV–V_2 and I–III–VI_2 crystals with solutions of ammonium sulfide in *tert*-butyl alcohol.

The samples were electrically homogeneous single-crystal wafers of the ternary compounds $CdSiAs_2$, $ZnSnP_2$, $CuGaSe_2$, and r-$AgInS_2$ having arbitrary crystallographic orientation and average dimensions of $2\times2\times1$ mm. Ternary II–IV–V_2 compounds ($CdSiAs_2$ and $ZnSnP_2$) were grown by directional low-temperature crystallization from nonstoichiometric melts and exhibited a chalcopyrite structure with crystal lattice parameters consistent with those reported in the literature.[9] Ternary I–III–IV_2 compounds ($CuGaSe_2$ and $AgInS_2$) were grown by directional crystallization from near-stoichiometric melts. The growth regime produced $CuGaSe_2$ single crystals with a chalcopyrite structure and $AgInS_2$ single crystals with an orthorhombic structure; the lattice parameters were also consistent with those given in

TABLE I. Electrical and luminescence properties of ternary semiconductors.

	$T=300$ K		$T=77$ K	
Semiconductor	p, cm^{-3}	$\mu_p^{300\ K}$, $cm^2/(V\cdot s)$	$h\upsilon_m$, eV	I_m/I_{m0}
$CdSiAs_2$	3×10^6	350	1.54	6.0
$ZnSnP_2$	8×10^{16}	45	1.425	5.0
$CuGaSe_2$	5×10^{17}	20	1.475	2.3
r-$AgInS_2$	2×10^{16}	35	2.015	4.0
			1.910	1.8
			1.720	1.2

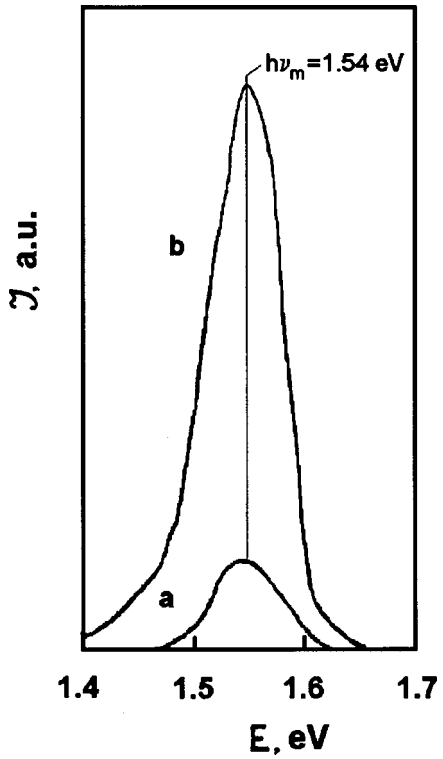

FIG. 1. Photoluminescence spectrum of chalcopyrite $CdSiAs_2$ single crystal before (a) and after (b) treatment with a solution of ammonium sulfide in *tert*-butyl alcohol at $T=77$ K.

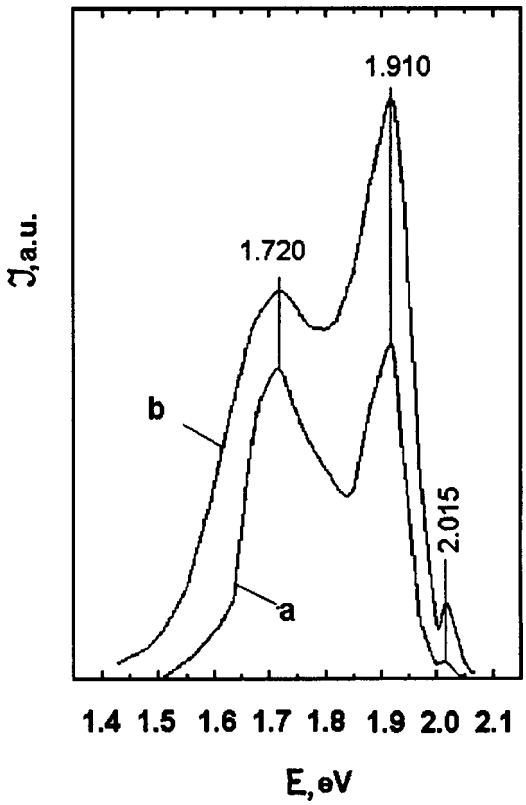

FIG. 2. Photoluminescence spectrum of orthorhombic r-$AgInS_2$ single crystal before (a) and after (b) treatment with a solution of ammonium sulfide in *tert*-butyl alcohol at $T=77$ K.

the literature.[9] The crystals were grown without intentionally introducing any impurities and possessed p-type conductivity. The concentrations and Hall mobilities of the holes are given in Table I.

Sulfide passivation was carried out using a solution of ammonium sulfide $(NH_4)_2S$ in *tert*-butyl alcohol t-C_4H_9OH at room temperature. The passivation time differed for different crystals, ranging between 10 and 100 min.

Photoluminescence was excited by He–Cd laser radiation ($\lambda=0.44\,\mu$m, $P=15$ mW); the depth of absorption of the radiation was 10^{-5}–10^{6} cm. The photoluminescence spectra were recorded using an MDR-3 monochromator with an FÉU-62 photomultiplier. The spectral resolution was at least 1 meV. The measurements were made at liquid nitrogen temperature. Initial crystals for which the parameters of the photoluminescence spectra were highly reproducible from one point to another were selected by probing the surface with exciting focused radiation (spot diameter around 0.1 mm).

The experimental results are as follows. The photoluminescence spectra of the nonpassivated $CdSiAs_2$ (Fig. 1), $ZnSnP_2$, and $CuGaSe_2$ contain a single band and the spectrum of nonpassivated r-$AgInS_2$ (Fig. 2) contains three bands for which the energy position of the maxima $h\nu_m$ is given in Table I). Most of the photoluminescence bands observed in these crystals are caused by radiative transitions involving various lattice defect levels, but for r-$AgInS_2$ the shortest-wavelength peak may be juxtaposed with the interband radiation.

An analysis of the results suggests that sulfide passivation of the surface of $CdSiAs_2$ (Fig. 1), $ZnSnP_2$, and $CuGaSe_2$ crystals enhances the photoluminescence intensity but the band profile and the energy positions of their peaks remain unchanged. Table I gives the increase in the photoluminescence intensity for these crystals relative to the intensity of the nonpassivated semiconductor I_m/I_{m0}.

Sulfide passivation of the surface of r-$AgInS_2$ increases the intensity of all three photoluminescence bands, but to different degrees (Fig. 2, Table I). The largest increase (fourfold) was observed for the high-energy band (peak energy 2.015 eV) attributed to interband luminescence. The longer-wavelength bands with peak energies of 1.91 and 1.72 eV, attributed to radiative transitions in donor–acceptor pairs or between local defect levels and combined bands, also increase but to a lesser extent compared with the edge band (by factors of 1.8 and 1.2, respectively) (Fig. 2, Table I).

The experimental results indicate that sulfide passivation of crystals of two different classes of ternary compounds with different atomic composition using a solution of ammonium sulfide in *tert*-butyl alcohol substantially reduces the surface nonradiative recombination rate. The fact that the profile and position of the peaks remain unchanged under sulfide passivation indicates that the surface recombination rate is reduced without any change in the dominant mechanism of radiative carrier recombination.

To sum up, sulfide passivation with alcohol solutions, which has been successfully used to passivate III–V semiconductors,[6,7] can substantially improve the electronic properties of the surface of II–IV–V_2 and I–III–VI_2 crystals and can be used to enhance the efficiency of devices made using these semiconductors.[10]

[1] B. J. Scromme, C. J. Sandroff, E. Yablonovich, and T. Gmitter, Appl. Phys. Lett. **51**, 2022 (1987).
[2] P. D. Moulin, S. P. Tobin, M. S. Lundstrom, M. S. Carpenter, and M. R. Melloch, IEEE Electron Device Lett. **9**, 368 (1988).
[3] R. N. Nottenburg, C. J. Sandroff, D. A. Humphrey, T. H. Hollenbeck, and R. Bhat, Appl. Phys. Lett. **52**, 218 (1988).
[4] L. J. Huang, K. Rajesh, W. M. Lau, S. Ingrey, D. Landheer, J.-P. Noël, and Z. H. Lu, J. Vac. Sci. Technol. A **13**, 792 (1995).
[5] A. J. Howard, C. I. H. Ashby, J. A. Lott, R. P. Schneider, and R. F. Corless, J. Vac. Sci. Technol. A **12**, 1063 (1994).
[6] V. N. Bessolov, E. V. Konenkova, and M. V. Lebedev, J. Vac. Sci. Technol. B **14**, 2761 (1996).
[7] V. N. Bessolov, M. V. Lebedev, Yu. M. Shernyakov, and B. V. Tsarenkov, Mater. Sci. Eng., B **44**, 380 (1977).
[8] A. J. Nelson, C. R. Schwerdtfeder, G. C. Herdt, D. King, M. Contreras, K. Ramanathan, and W. L. O'Brien, J. Vac. Sci. Technol. A **15**, 2058 (1997).
[9] *Handbook of Physicochemical Properties of Semiconductors* [in Russian], Nauka, Moscow (1978), 340 pp.
[10] Yu. V. Rud', Fiz. Tekh. Poluprovodn. **28**, 1105 (1994) [Semiconductors **28**, 633 (1994)].

Translated by R. M. Durham

Influence of uniaxial compression on the photoconductivity of highly compensated Si⟨B, Mn⟩

M. K. Bakhadyrkhanov, Kh. M. Iliev, and Kh. F. Zikrillaev

Tashkent State Technical University
(Submitted May 6, 1998)
Pis'ma Zh. Tekh. Fiz. **24**, 23–28 (November 26, 1998)

It was observed that the photosensitivity limit and the increase in the photoresponse depend fairly strongly on uniaxial elastic deformation in compensated Si⟨B, Mn⟩ crystals.
 [S1063-7850(98)01811-4]

A characteristic feature of the photoconductivity spectra of highly compensated Si⟨B, Mn⟩ (i.e., $|1-k| \ll 1$, where k is the degree of compensation of the material) is that near the fundamental absorption region the photocurrent increases very steeply. Bakhadyrkhanov[1] noted that the anomalously high photosensitivity of highly compensated Si⟨B, Mn⟩ is caused by the manganese atoms forming various multiply charged clusters which act as sensitizing centers. These centers are barely screened because of the absence of any equilibrium carriers in the highly compensated Si⟨B, Mn⟩ and the lifetime of the nonequilibrium carriers in this crystal becomes asymmetric. We can postulate that changes in the state of these charged clusters, induced by any external mechanical influences which alter the symmetry of the crystal lattice, should be observed in the photoconductivity spectra.

In this context, it is interesting to study the influence of uniaxial elastic compression on the spectral dependence of the photoconductivity near the fundamental absorption region in highly compensated Si⟨B, Mn⟩ samples.

These investigations will allow us not only to determine more accurately any change in the silicon band gap under uniaxial elastic compression but also to assess the possibility of using the photoconductivity of uniaxially compressed, highly compensated Si⟨B, Mn⟩ to record infrared radiation and strain.

For the investigations we used a batch of Si⟨B, Mn⟩ samples with different degrees of compensation and the [111], [110], and [100] crystallographic axes directed along the large edge. The initial material was KDB-10 industrial-grade silicon into which manganese was introduced by diffusion from the gas phase in the temperature range 1000–1150 °C. The photoconductivity spectra of the Si⟨B, Mn⟩ samples under uniaxial elastic compression were investigated using an IKS-21 infrared spectrometer and a special cryostat which could produce mechanical stresses up to 2×10^4 kg/cm^2 in $4\times1\times1$ mm samples at temperatures between 80 and 300 K.

Figure 1 gives the spectral dependence of the photocurrent near the fundamental absorption region for highly compensated Si⟨B, Mn⟩ samples with $\rho=10^5\ \Omega\cdot$cm with and without uniaxial elastic compression at $X=8\times10^8$ Pa and with the compression condition $\{I_{ph}\|X\|[100]\}$. It can be seen that in the fundamental absorption region the photocurrent increases very abruptly in these samples (curve *1*). The photoconductivity spectra of the samples under uniaxial elastic compression (curve *2*) were obtained under identical conditions. The photoconductivity spectrum under compression is shifted toward longer wavelengths and the photocurrent increases slightly more steeply compared with the spectrum in the absence of compression. Compression increases the photocurrent by almost three orders of magnitude (points *a* and *b*) and when the compression is removed, the photocurrent returns to its level before compression. Similar results were obtained for all the highly compensated Si⟨B, Mn⟩ samples within the elastic compression range. Preliminary calculations of the photocurrent sensitivity to uniaxial elastic compression within the fundamental absorption region indicate that this is appreciably higher than the strain sensitivity of silicon caused by a change in its resistivity. This indicates that Si⟨B, Mn⟩ samples can be used to fabricate a strain gauge having a sensitivity several orders of magnitude better than that of commercial silicon strain gauges.

Figure 2 shows spectral dependence of the relative changes in the photocurrent of these samples under the condition $\{I_{ph}\|X\|[100]\}$ for degrees of compression $X=2\times10^8$, 4×10^8, 6×10^8, and 8×10^8 Pa. It can be seen from Fig. 2a that the maximum of the photocurrent corresponding to photon energies in the fundamental absorption region shifts toward longer wavelengths as the degree of compression increases. It should be noted that as the compression increases, the range of maximum photocurrents becomes more gently sloping, which leads to broadening of the frequency range of the photosensitivity. Thus, mechanical compression can be used not only to broaden and shift the fundamental absorption region of the samples but also to broaden the frequency range of their sensitivity. Similar investigations of highly compensated Si⟨B, Mn⟩ samples under the compression conditions $\{I_{ph}\|X\|[110]\}$ and $\{I_{ph}\|X\|[111]\}$ revealed qualitative agreement with the shift of the photoconductivity spectra for compression in the direction of the [100] crystallographic axis but quantitatively these shifts were smaller.

The qualitative agreement between the experimental results obtained for the photoconductivity spectra under the compression conditions $\{I_{ph}\|X\|[100]\}$, $\{I_{ph}\|X\|[110]\}$, and $\{I_{ph}\|X\|[111]\}$ indicates that the observed shifts are caused

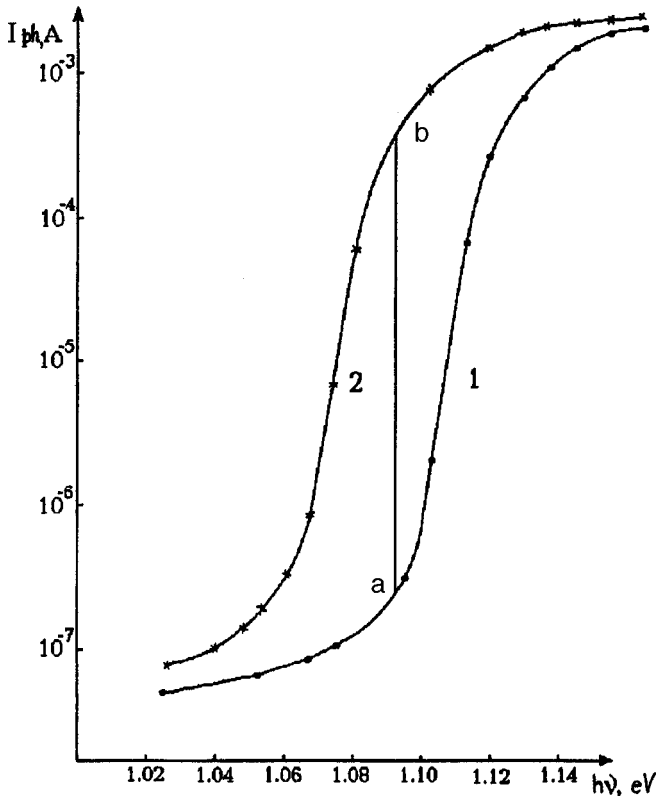

FIG. 1. Spectral dependence of the photoconductivity of highly compensated Si⟨B,Mn⟩ under uniaxial compression $\{I_{ph}\|X\|[100]\}$ at $T=77$ K: *1* — $X=10^5$ Pa, *2* — $X=8\times10^8$ Pa.

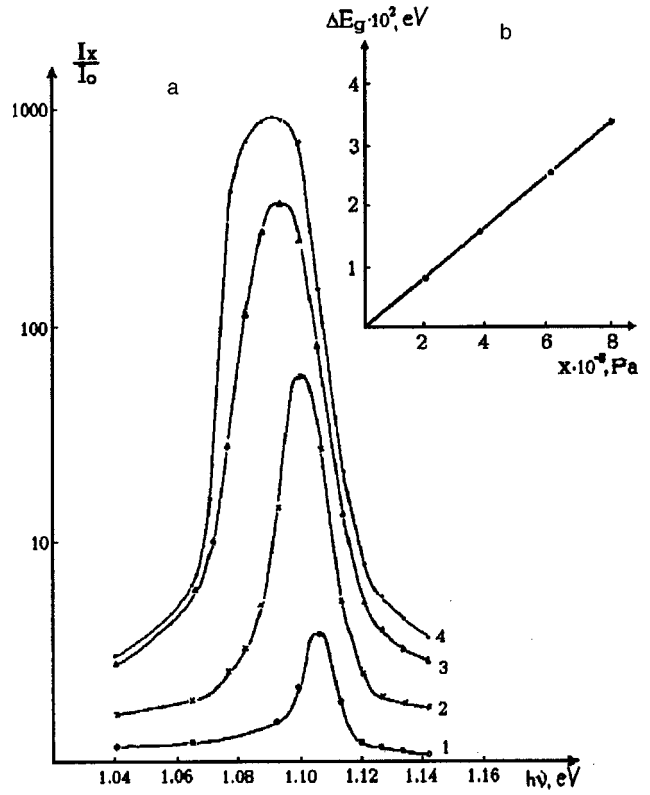

FIG. 2. Spectral dependence of the relative changes in the photocurrent (a) and the band gap of Si under uniaxial elastic compression (b): *1* — $X=2\times10^8$ Pa, *2* — $X=4\times10^8$ Pa, *3* — $X=6\times10^8$ Pa, and *4* — $X=8\times10^8$ Pa.

by a reduction of the band gap. This is also evidenced by the low-energy shift of the red limit of the photoresponse as a function of the degree of compression under the condition $\{I_{ph}\|X\|[100]\}$ plotted in Fig. 2b. From this figure we can infer that the Si band gap decreases under uniaxial elastic compression as $Eg(x)=Eg(0)-\alpha X$.

The experimental results were used to determine the pressure coefficients of variation of the silicon band gap under the conditions $\{I_{ph}\|X\|[100]\}$, $\{I_{ph}\|X\|[110]\}$, and $\{I_{ph}\|X\|[111]\}$, which are respectively:

$$\alpha_{[100]}=4.25\times10^{-11}\ \text{eV/Pa},$$

$$\alpha_{[110]}=2.75\times10^{-11}\ \text{eV/Pa},$$

$$\alpha_{[111]}=2.25\times10^{-11}\ \text{eV/Pa},$$

and are of the same order of magnitude as the data obtained in Refs. 2 and 3.

It is known[2,3] that when silicon crystals are compressed in the direction of the [100] crystallographic axis, the band gap shows the largest decrease and thus, the shift of the photoconductivity spectra in this direction is greater than that under compression in the [110] and [111] directions. The increased steepness of the photocurrent spectrum is evidently caused by a change in the degree of filling of the deep manganese level under elastic compression[4] which leads to a change in the degree of compensation of the samples and the cross section for capture of electrons and holes at ionized manganese centers.

[1] M. K. Bakhadyrkhanov, Author's Abstract of Doctoral Dissertation [in Russian], Leningrad (1982).
[2] P. I. Baranskiĭ, V. P. Klochkov, and I. V. Potykevich, *Semiconductor Electronics* [in Russian], Naukova Dumka, Kiev (1973), 703 pp.
[3] A. L. Polyakova, *Deformation of Semiconductors and Semiconducting Devices* [in Russian], Énergiya, Moscow (1981), 168 pp.
[4] Kh. M. Iliev, Author's Abstract of Dissertation for Candidate's Degree [in Russian], Tashkent, (1991).

Translated by R. M. Durham

Radiation resistance of the internal memory of programmable logic devices

Yu. A. Kotov, S. Yu. Sokovnin, and V. A. Skotnikov

Institute of Electrophysics, Urals Branch of the Russian Academy of Sciences, Ekaterinburg
(Submitted December 1, 1997)
Pis'ma Zh. Tekh. Fiz. **24**, 29–32 (November 26, 1998)

An investigation was made of the radiation resistance of the internal memory of programmable logic devices. It was established that the internal memory of CMOS devices shows enhanced sensitivity to ionizing radiation when their outputs are shorted together. Information stored in the internal memory of the devices is erased at an absorbed dose substantially below the level at which the device fails. It is suggested that this effect may be used as a method of erasing information. © *1998 American Institute of Physics.* [S1063-7850(98)01911-9]

Programmable logic devices (PLDs), especially microcontrollers, are now widely used in the design of electronic devices. These PLDs can be used to construct new devices by programming their internal memory, which is simpler, faster, and cheaper than the usual method. Commercially available emulation tools can be used for computer modeling of the functions of the PLD itself and the electronic device being constructed before writing the program in the internal memory of the PLD. However, the problem of the radiation resistance of the PLD internal memory and also the possibility of re-use arises in many applications. These PLDs are fairly expensive and recently manufacturers have abandoned the use of expensive ultraviolet-transparent windows on PLD chips. These windows made it possible to re-use PLDs by erasing the internal memory with ultraviolet light.

We know that radiation, including bremsstrahlung, can be used to monitor the quality and modify the properties of microcircuits.[1] The effect of ionizing radiation on the materials and design of in-circuit memory chips has been thoroughly studied,[2] although we could find no investigations of the radiation resistance of PLD internal memories reported in the literature.

Thus, we investigated the action of bremsstrahlung from a pulsed high-current electron beam on the internal memory of a PLD. The experiments were carried out using Zilog Z86 and Intel 87C196KR microcontrollers. The radiation source was a URT-0.5 accelerator[3] (electron energy 0.5 MeV) operated as a bremsstrahlung generator at frequency 50 Hz, which delivered an average absorbed dose rate of 7.64 Gy/min at a distance of 0.5 cm from the target where the PLDs were located, with a maximum (per pulse) absorbed dose rate of 6.36 kGy/s.

The microcontrollers were monitored and written as follows: Z86 using the manufacturer's programmer-emulator and 87C196KR using a ''Sterkh-710'' programmer, ''Bond'' Scientific-Industrial Organization, Berdsk.

PLDs with test patterns written to all locations or working programs loaded were irradiated until the internal memory was completely erased. The PLD was periodically monitored during irradiation. After irradiation, the PLDs were examined to determine whether test and working programs could be written, followed by operation in a real device.

We established that information in the internal memory of the PLDs is completely preserved up to the absorbed dose levels at which they are known to start malfunctioning (higher than 1000 Gy) (Ref. 2). However, we found that the information could be erased when the PLD was wrapped in aluminum foil so that all the microcircuit contacts were reliably shorted. In this case, the following results were obtained:

1) Information in the internal memory of all the PLDs was completely erased (using ten of each type) after irradiation for 50 min (absorbed dose around 380 Gy);

2) At half the dose needed for total erasure, most of the information was erased, except for a few randomly distributed bits;

3) After the first erasure, all the PLDs were suitable for reuse, after the second erasure this figure was 80%, and 50% of the microcircuits withstood four cycles.

These results differ appreciably from those reported in Ref. 2 where it was shown that 1802 microprocessors fabricated by CMOS technology failed at doses above 130 Gy. However, these microprocessors had substantially thicker below-gate insulators compared with our PLDs (an increase in thickness substantially reduces the radiation resistance of microcircuits[2]).

Writing to a memory cell of a CMOS PLD is performed by applying a specific negative critical voltage at which a charge forms at the interface of the nitride and silicon dioxide layers and a high logic level ''1'' is established. When a positive critical voltage is applied, a low logic level ''0'' is established.[4] Thus, to erase the PLD the charge must be reduced from logic ''1'' to logic ''0.'' The mechanism for dissipation of charge under irradiation can be either a surface or a bulk one. At x-ray intensities higher than 10^2 Gy/s, as in our case, the densities of the injection and bulk currents become comparable $\sim 10^{-7}$ A/cm^2 (Ref. 2).

The fact that the PLD outputs must be electrically connected to erase information confirms that leakage currents play a major role in removing the charge, since a CMOS transistor memory element circuit[4] assumes no connections between the write, read, address, supply, and ground busses.

However, this complicates the current dissipation path if there is no connection between the busses.

However, our intensities were not sufficient (threshold 10^6 Gy/s) for the evolution of the photovoltaic effect where the voltage drop changes at the below-gate insulator thus shifting the threshold voltage.[2]

To check out the erasure mechanism, we irradiated written 87C196LK PLDs with ^{60}Co radiation at a dose rate of around 0.2 Gy/s. The information in the PLDs was completely erased at an absorbed dose of 500 Gy, which confirms that the dose rate has no or very little influence in the range studied 0.2–6360 Gy/s.

To sum up, we have established that the internal memory of CMOS PLDs exhibits enhanced sensitivity to ionizing radiation when its outputs are shorted. Information stored in the internal memory of the PLDs is erased at an absorbed dose substantially below the level at which the PLD malfunctions.

These data on the possible number of PLD erasure cycles can be used to estimate the absorbed dose level at which these PLDs begin to malfunction, above 700 Gy.

This effect can be used as a method of erasing information written in the internal memory of PLDs so that they can be reused.

[1] V. S. Vavilov, B. M. Gorin, N. S. Danilin *et al.*, *Radiation Methods in Solid-State Electronics* [in Russian], Radio i Svyaz', Moscow (1990), 184 pp.
[2] V. S. Pershenkov, V. D. Popov, and A. V. Shal'nov, *Surface Radiation Effects in Elements of Integrated Microcircuits* [in Russian], Énergoatomizdat, Moscow (1988), 256 pp.
[3] Yu. A. Kotov and S. Yu. Sokovnin, *Accelerator for Commercial Application URT-0.5, Proceedings of 11th IEE International Pulsed Power Conference*, 1997, Baltimore, USA (in press).
[4] S. V. Yakubovskiĭ *et al.*, *Textbook of Analog and Digital Integrated Microcircuits* [in Russian], Radio i Svyaz', Moscow (1984), 432 pp.

Translated by R. M. Durham

Ion energy cost in a combined inductive–capacitive rf discharge

S. V. Dudin, A. V. Zykov, K. I. Polozhiĭ, and V. I. Farenik

Kharkov State University Scientific Physicotechnological Center, Kharkov
(Submitted November 11, 1997)
Pis'ma Zh. Tekh. Fiz. **24**, 33–39 (November 26, 1998)

Experimental measurements were made of the ion energy cost η as a function of the parameters of a combined rf inductive–capacitive discharge at low pressures ($p<10^{-2}$ Torr). It was established that η does not depend on the power supplied, it has a minimum as a function of pressure, and also decreases when an rf potential is applied to the electrodes. The results can be used to find the optimum parameters in terms of energy efficiency of ion formation and may be useful for refining the theoretical models of a combined rf inductive–capacitive discharge. © *1998 American Institute of Physics.* [S1063-7850(98)02011-4]

An rf induction discharge has been widely used as the plasma-forming stage in various ion plasma process systems.[1–4] In these systems the fixed self-bias potential formed at the electrodes to which rf voltage is applied[5] is frequently used to accelerate the ions from the induction discharge plasma to the surface being treated. In this case, the gas discharge combines the bulk nature of the processes in an electrodeless induction discharge with the important role of the electrode layers typical of a capacitive discharge, and is in fact a combined rf inductive–capacitive discharge.[6]

Although many studies have dealt with the physics of induction discharges[7,8] and electrode layers,[9,10] and patents have also been published,[11,12] the combined rf inductive–capacitive discharge has been little studied. We investigated this type of discharge in Ref. 6 where they analyzed the power distribution at low pressure and determined the optimum ratio of system parameters in terms of energy input to the ion flux to the target. We used the approximation of a constant ion energy cost η although we know that this value depends on the discharge parameters.[13] Here we propose to measure this dependence experimentally for a low-pressure rf inductive–capacitive discharge.

Different authors define the ion energy cost differently, depending on the particular problem. For example, in theoretical studies, such as Ref. 9, this value characterizes the total energy losses by the electrons as a result of elastic and inelastic collisions with the formation of a single ion in the bulk of the discharge. In technical applications such as ion sources, the ion energy cost is defined as the ratio of the total power supplied to the ion beam current.[1] Practical experience shows that the most convenient characteristic for comparing the efficiency of the ion-forming stages of various ion plasma process systems is the value $\eta=eP_i/I$, where $I=\oint_S j(\xi)d\xi$ is the total ion current to the walls of the gas discharge chamber, S is the surface area of the electrodes confining the plasma, j is the ion current density at the plasma boundary, and P_i is the power absorbed in the bulk, which includes the electron energy losses in elastic and inelastic collisions, and also the unavoidable losses of energy transferred by the charged particle fluxes to the plasma boundary as a result of their thermal motion.

With this definition of the ion energy cost, the value of η for an rf inductive–capacitive discharge can easily be expressed in terms of parameters which can be directly measured experimentally: I, the power absorbed by the discharge P_0, the amplitude φ of the rf voltage between the electrodes, and the ratio of the electrode areas δ ($\delta>1$). In a pure induction discharge we find $\varphi=0$ and $P_i=P_0$. When $\varphi\neq 0$, we find $P_i=P_0-P_a$, where P_a is the power dissipated in acceleration of the ions. The value of P_a, which depends on δ and φ, can be calculated using the theoretical model of the power balance in an rf inductive–capacitive discharge described in Ref. 6. Using the results of this study, we can easily derive the following expression for η in a combined rf discharge: $\eta=e(P_0-P_a)/I$, where $P_a=\gamma(\delta)\cdot\varphi\cdot I$, and the function $\gamma(\delta)$ allows for the influence of the ratio of areas of the rf electrodes on the power distribution in the discharge. At low pressures when the ''3/2-power'' law holds for the positive ion current in the rf electrode layers,[14,15] the voltage ratios between the plasma and the electrodes are inversely proportional to the ratio of the fourth powers of their areas and $\gamma(\delta)=\delta(\delta^2-\delta+1)/(1+\delta^4)$ (Ref. 6).

Experiments to determine η and its functional dependence on the parameters of an rf inductive–capacitive discharge were carried out using an apparatus equipped with a single-grid source of low-energy ions.[3] The source is shown schematically in Fig. 1. An rf voltage of frequency 13.56 MHz was supplied by a UV-1 generator via a matching device to an internal screened inductor *3* and the cylindrical housing of the gas-discharge chamber *4*, which also functioned as the rf electrode. The grounded electrode was a grid *1*. The geometric dimensions of the ion source were as follows: length 80 mm and diameter 250 mm, i.e., this design had $\delta\approx 3$. The range of variation of the working parameters of the ion source was as follows: pressure in gas discharge chamber $p=10^{-4}$–10^{-2} Torr, voltage at rf electrode $\varphi=0$–500 V, and rf power supplied $P=0.2$–1 kW. The ion current density j at the walls of the discharge chamber and at the grid was measured using a single planar probe *6* under conditions of ion current saturation. Measurements of the current density distribution showed that for $p<10^{-3}$ Torr, this was almost uniform over the plasma surface and thus we

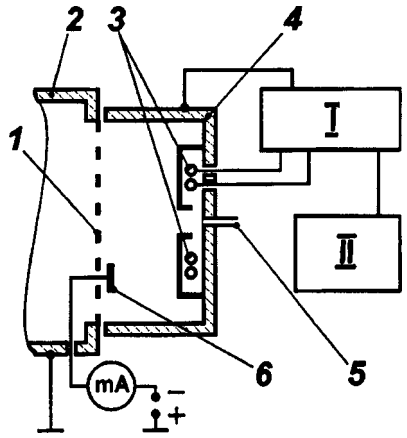

FIG. 1. Schematic of rf ion source: *1* — grounded grid electrode, *2* — connecting flange of vacuum chamber, *3* — screened two-turn inductor, *4* — metal housing of gas-discharge chamber, I — matching device, II — rf generator, *5* — working gas inlet, and *6* — single planar probe.

assumed $I=jS$ in the calculations. To determine the power P_0 deposited directly in the discharge ($P_0=P-P_{\text{loss}}$), we measured the electrical power loss P_{loss} in the inductor and the matching device. The ion energy cost was calculated using the experimental data and the formula given above.

Systematic investigations were made of the dependence of η on P_0, p, and φ in a combined discharge using argon as the working gas. The use of other gases such as air, Freon, nitrogen, and oxygen revealed no qualitative differences in the dependence of η on p and φ, with only the absolute value of η varying (the difference was less than 30%).

An analysis of the results of the measurements showed that in an inductive discharge ($\varphi=0$) η does not depend on the power deposited in the discharge over the entire range studied (j is proportional to P_0). However, we established that η depends strongly on the pressure in the gas-discharge chamber. Figure 2a gives results of experimental measurements of j and also values of η calculated using these, plotted as a function of p for various φ. The curves typically show a minimum of η at $p\sim10^{-3}$ Torr or, in other words, there is an optimum pressure range in terms of ion formation efficiency both for an inductive discharge and for an rf inductive–capacitive discharge.

The results for a pure inductive discharge ($\varphi=0$) show good agreement with the theoretical calculations[16] made using the approximation of a Maxwellian electron energy distribution function. In this case, the energy flux transferred by the charged particles to the walls of the discharge chamber is proportional to the electron temperature T_e, which depends only on the pressure p and the characteristic system dimension d, that is η is uniquely determined by the parameter pd.

In the graphs plotted in Fig. 2a we also draw attention to the decrease in η when a potential is applied to the rf electrodes. In order to identify the laws governing this effect at fixed p and P_0, we measured the dependence $\eta(\varphi)$ and the results are plotted in Fig. 2b. It can be seen that as φ increases, the ion energy cost decreases monotonically from $\eta\approx80$ eV/ion in a pure inductive discharge ($\varphi=0$) to the minimum $\eta\approx30$ eV/ion at $\varphi>300$ V.

On the basis of theoretical models of a capacitive rf discharge,[17–19] we postulate that the reduction of the ion en-

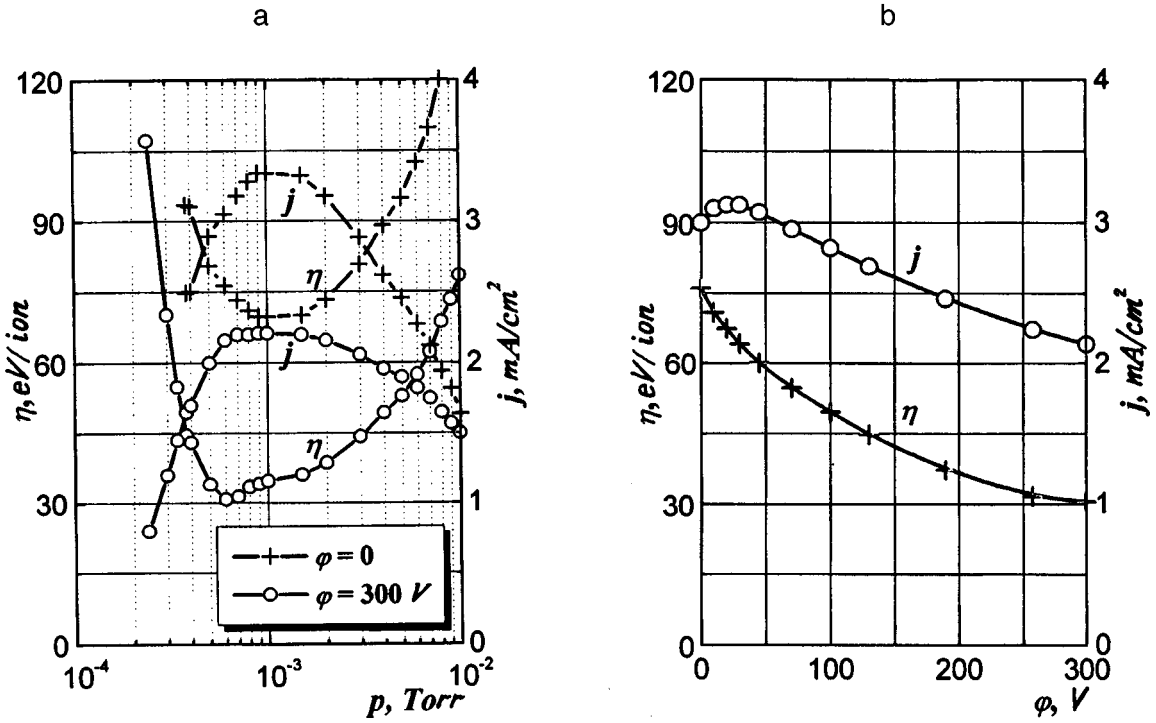

FIG. 2. Ion energy cost η and current density to probe j as a function of a—pressure p in the gas discharge chamber for a pure inductive discharge ($\varphi=0$ V) and for an rf inductive–capacitive discharge ($\varphi=300$ V) and b—as a function of the potential φ at the rf electrode at constant pressure $p=5.5\times10^{-4}$ Torr, $P_0=400$ W.

ergy cost with increasing φ is caused by an increased fraction of fast electrons in the electron energy distribution function. This may be caused by stochastic heating of the electron gas as a result of its interaction with the rf electrode layers or it may be attributed to Ohmic heating in the plasma phase of the capacitive layer.[18] However, before definitive conclusions can be drawn as to the nature of this effect, the dynamics of the electron energy distribution function must be investigated experimentally when an inductive discharge is exposed to a weak potential rf electric field. We plan to carry out such experiments in the very near future.

To sum up, we have measured the ion energy cost as a function of the parameters of a combined rf inductive–capacitive discharge at low pressures. We have established that η does not depend on the supplied power, it has a minimum as a function of pressure, and also decreases when a potential rf electric field is applied to the plasma. These results were used to find the optimum parameters of the process system in terms of ion formation efficiency and to obtain data needed to refine the theoretical models of a combined rf inductive–capacitive discharge.

[1] M. D. Gabovich, *Physics and Engineering of Plasma Ion Sources* [in Russian], Atomizdat, Moscow (1972).
[2] *Plasma Processing for VLSI*, edited by N. G. Einspruch and D. M. Brown, Vol. 8 of VLSI Electronics (Academic Press, New York, 1984; Mir, Moscow, 1987).
[3] A. M. Budyanskiĭ, A. V. Zykov, and V. I. Farenik, *Rf Ion Source* Ukrainian Patent No. 2426, Russian Patent No. 1570549 (28.06.93).
[4] J. Asmussen, J. Vac. Sci. Technol. A **7**, 883 (1989).
[5] Yu. P. Raĭzer and M. N. Shneĭder, Fiz. Plazmy **18**, 1211 (1992).
[6] S. V. Dudin, A. V. Zykov, and K. I. Polozhiĭ, Pis'ma Zh. Tekh. Fiz. **22**(19), 54 (1996) [Tech. Phys. Lett. **22**, 801 (1996)].
[7] J. A. Hopwood, Plasma Sources Sci. Technol. **1**, 109 (1992).
[8] M. M. Turner, Phys. Rev. Lett. **71**, 1844 (1993).
[9] M. A. Lieberman, J. Appl. Phys. **65**, 4186 (1989).
[10] A. M. Budyanskiĭ, Pis'ma Zh. Tekh. Fiz. **18**(1), 17 (1992) [Tech. Phys. Lett. **18**, 6 (1992)].
[11] J. S. Ogle, US Patent 4948458 (1990).
[12] D. K. Coultas and J. H. Keller, European Patent, Publication N 0379828, A2 (1990).
[13] G. R. Misium, A. J. Lichtenberg, and M. A. Lieberman, J. Vac. Sci. Technol. A **7**, 1007 (1989).
[14] M. A. Lieberman, J. Appl. Phys. **65**, 4186 (1986).
[15] A. M. Budyanskiĭ, Pis'ma Zh. Tekh. Fiz. **18**(1), 17 (1992) [Tech. Phys. Lett. **18**, 6 (1992)].
[16] V. G. Bondarenko, V. P. Denisov, B. G. Eremin *et al.*, Fiz. Plazmy. **17**, 756 (1991) [Sov. J. Plasma Phys. **17**, 442 (1991)].
[17] I. D. Kaganovich and L. D. Tsendin, IEEE Trans. Plasma Sci. **20**(2), 66 (1992).
[18] I. D. Kaganovich and L. D. Tsendin, IEEE Trans. Plasma Sci. **20**(2), 86 (1992).
[19] B. P. Wood, M. A. Lieberman, and A. J. Lichtenberg, IEEE Trans. Plasma Sci. **23**(1), 89 (1995).

Translated by R. M. Durham

Influence of diffusive processes on the formation of the radial structure of an electric arc in metal vapor

I. L. Babich, A. N. Veklin, V. A. Zhovtyanskiĭ, and A. Yu. Pan'kin

Taras Shevchenko University, Kiev
(Submitted May 27, 1998)
Pis'ma Zh. Tekh. Fiz. **24**, 40–45 (November 26, 1998)

The role of diffusive processes in the establishment of the radial structure of a free-burning electric arc was investigated experimentally and numerically. It is shown that the increased content of plasma-forming particles in the peripheral region of arcs observed in many experiments arises from the inadequacy of the assumption on the plasma equilibrium state. This effect can be attributed to the plasma nonequilibrium established as a result of resonant radiation from the hotter axial region undergoing absorption and reemission at the edge of the arc.
 [S1063-7850(98)02111-9]

An arc was struck in air between 6 mm diameter uncooled copper electrodes with an interelectrode gap of 2–8 mm. In order to avoid droplet formation, the arc was generated by a current of up to 100 A amplitude and 30 ms duration, which was superposed on an arc-sustaining low-current discharge. The investigations were carried out at the quasisteady stage of the process. As a result of the spatial and temporal instability of the discharge, we used a method of one-shot tomographic recording[1] of the radial intensity distribution of the 510.5 and 521.8 nm copper spectral lines which were used to determine the plasma temperature profile $T(r)$. The electron density distribution $N_e(r)$ was measured from the absolute intensity of the 465.1 nm line.

The equation of state assuming local thermodynamic equilibrium was used to calculate the radial profiles of the total density of copper atoms and ions $N_{\mathrm{Cu}}(r)$. When converted to the relative content $x_{\mathrm{Cu}}=N_{\mathrm{Cu}}/\Sigma N$ (where ΣN is the total density of heavy particles in a copper–air plasma), these profiles show an increase in x_{Cu} at the edge of the arc, as in Refs. 2 and 3. It is generally assumed that this increase is caused by separation of the components of the plasma-forming mixture during diffusion (known as ''demixing'' in the English language literature). In our case, the only characteristic feature is that this increase is far more noticeable and is almost an order of magnitude greater than in the axial region. This is evidently caused by the different type of arc, free-burning here as opposed to wall-stabilized in Refs. 2 and 3. In any case, this result is physically meaningless.

We used laser absorption spectrometry to attempt to expand the region of investigation in the radial direction. This involved recording the ''shadow'' from the arc at the entry slit of a spectrometer using a parallel beam from a copper vapor laser. The coefficient of self-absorption $\varkappa_0$ thus determined at the center of the 510.5 nm spectral line was appreciable in a spatial region whose radius was several times larger than the size of the arc emitting zone (Fig. 1). Since the energy of the lower level of the transition responsible for the absorption on the 510.5 nm line is only 1.39 eV, the populations of this level and the ground level are closely related and the results of measurements of the self-absorption in fact reflect the distribution of the copper atom density.

The influence of diffusive processes was taken into account by simulating them numerically, assuming that the copper–nitrogen plasma of a free-burning electric arc is axisymmetric and consists of electrons, CuII ions, CuI atoms, and nitrogen molecules N_2:

$$(1/r)d/dr(r\Gamma_{\mathrm{Cu}})=S_{\mathrm{Cu}}, \tag{1}$$

where $S_{\mathrm{Cu}}=S_{\mathrm{Cu\,I}}+S_{\mathrm{Cu\,II}}$ is the density of the copper erosion source and Γ_{Cu} is the copper diffusive flux. The value of S_{Cu} is related to the discharge current via the coefficient of electrode erosion, whose value for copper was taken to be $b_r=10^{-4}$ g/C (Ref. 4). The boundary conditions were taken to be zero derivatives on the arc axis and zero x_{Cu} at the absorbing wall separated from the axis by the distance R_W. Equation (1) was supplemented by the Saha, Dalton, and quasineutrality equations.

We selected the following approximations for the radial profiles of the temperature and the density of the copper erosion source:

$$T(r)=(T_0-T_a)\exp[-(r/R_T)^2]+T_a,$$
$$S_{\mathrm{Cu}}(r)=S_0\exp[-(r/R_S)^2], \tag{2}$$

where $T_a=300$ K is the temperature of the surrounding medium. The first of these approximations is generally accepted for an electric arc[5] and the values of T_0 and R_T were selected to give the best agreement with the experimental results. It was found that the choice of function $S_{\mathrm{Cu}}(r)$ is unimportant; in the limits $R_S<R_T$ the result of the calculations is almost independent of the value of R_S.

The diffusion coefficients of the multicomponent mixture were defined in terms of the coefficients of binary diffusion,[6] which in turn were defined in terms of collision integrals as a function of the interaction potentials between the corresponding components allowing for the temperature dependences. Ambipolar diffusion was also taken into account in the calculations.

Since Eq. (1) is nonlinear, we cannot apply the maximum principle, whereby the solution can only have an extreme value at the boundaries.[7] Nevertheless, the results of

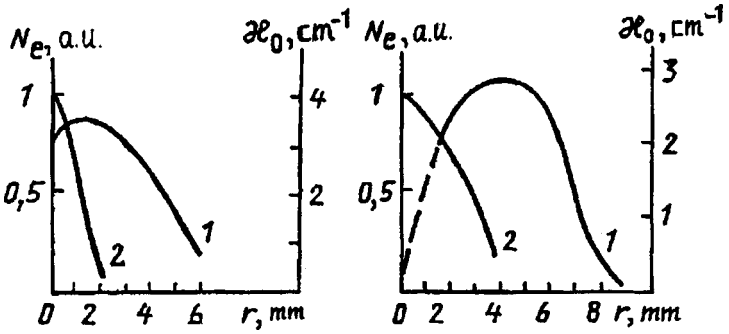

FIG. 1. Radial distributions of the absorption coefficient $\varkappa_0$ (curves *1*) and the relative electron density N_e (*2*) in the mid cross section of a free-burning arc between copper electrodes with current 30 A and interelectrode gaps of 2 (a) and 8 mm (b).

the calculations for various values of the parameters in Eq. (2) reveal extremes of the behavior of x_{Cu} only at the edge of the arc emitting zone (Fig. 2); no local maximum is observed, as in Refs. 2 and 3. Note that the substantial increase in the absolute values of $N_{\mathrm{Cu}}(r)$ observed in Fig. 2a with increasing distance from the axis is caused by the purely temperature-induced increase in the gas density at constant pressure. On the whole, Fig. 2 illustrates the freezing influence of the absorbing wall on the copper content in the arc itself and on the structure of its outer region. When the distance R_w between the wall and the axis is large (1 cm), the results agree with the measurements of the spatial profile of the absorption coefficient at the center of the 510.5 nm CuI spectral line (Fig. 1). The calculated profile $N_e(r)$ also shows satisfactory agreement with the experimental values.

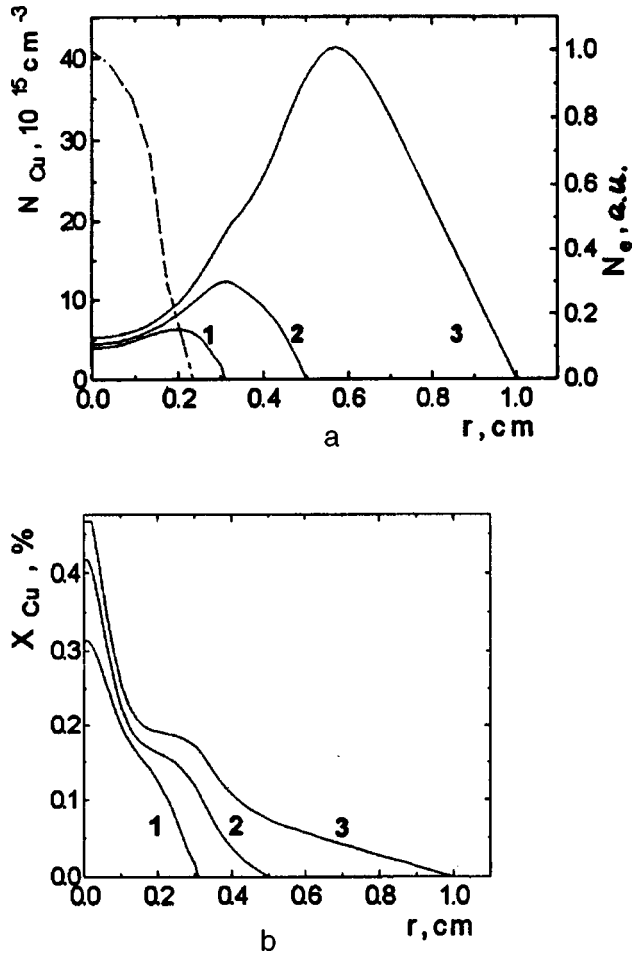

FIG. 2. Results of calculations of the radial profiles of the density N_{Cu} (a) and the content x_{Cu} (b) of copper vapor in a copper–nitrogen plasma allowing for diffusive processes for various distances between the absorbing wall and the discharge axis: $R_w = 0.3$ cm (curve *1*), 0.5 cm (*2*), and 1 cm (*3*). The dashed curve gives the profile of the relative electron density N_e. The following values of the parameters were used: $T_0 = 8400$ K, $R_T = 0.255$ cm; $S_0 = 9.5 \times 10^{16}$ cm$^{-3} \cdot$ s^{-1}, and $R_S = 0.06$ cm.

Thus, an unconventional approach to the study of a dense electric-arc plasma, combining spectroscopic measurements with the simulation of diffusive processes, has revealed that, contrary to the generally held opinion,[2,3] the diffusive separation of the mixture components is not a decisive factor in the establishment of the radial distribution of the metal vapor. The situation is broadly similar to the results obtained in Ref. 8 where Zhovtyanskiĭ *et al.* showed that under different physical conditions using different methods of investigation, diffusive processes play only a negligible role in the afterglow of a high-current pulsed discharge plasma in inert gases.

The problem of a catastrophic increase in the metal vapor content in the peripheral region of an arc arises because of the inadequacy of the assumption that local thermal equilibrium applies to the entire arc. Babich *et al.*[9] showed that resonant radiation from the hotter axial region of the discharge, undergoing absorption and reemission at the edge, ''imposes'' populations in excess of equilibrium for the local temperature on the resonant transition of the copper atoms. By systematically applying the model of partial local thermal equilibrium using the radiation transport equation, we can obtain physically substantiated distributions of electric-arc plasma components when making interpretations of the spectroscopic measurements.

[1] A. N. Veklich and V. A. Zhovtyanskiĭ, Zh. Prikl. Spektrosk. **50**, 565 (1989).
[2] A. M. Rahal, B. Rahhaoui, and S. Vacquie, J. Phys. D **17**, 1807 (1984).
[3] H. Ouajji, B. Cheminat, and P. Andanson, J. Phys. D **19**, 1903 (1986).
[4] C. W. Kimblin, Proc. IEEE **56**, 546 (1971).
[5] B. E. Paton, V. S. Gvozdetskiĭ, and D. A. Dudko, *Microplasma Welding* [in Russian], Naukova Dumka, Kiev (1979), 248 pp.
[6] Yu. V. Lapin and M. Kh. Strelets, *Internal Flows of Gas Mixtures* [in Russian], Nauka, Moscow (1989), 368 pp.
[7] V. S. Vladimirov, *Equations of Mathematical Physics*, M. Dekker, New York (1971); Nauka, Moscow (1981), 512 pp.
[8] V. A. Zhovtyanskiĭ and O. M. Novik, Zh. Tekh. Fiz. **59**(9), 186 (1989) [Sov. Phys. Tech. Phys. **34**, 1075 (1989)].
[9] I. L. Babich, A. N. Veklich, V. A. Golovkina, and V. A. Zhovtyanskiĭ, Zh. Prikl. Spektrosk. **56**, 323 (1992).

Translated by R. M. Durham

Investigation of strained $In_xGa_{1-x}As/InP$ quantum wells fabricated by metalorganic compound hydride epitaxy

A. D. Bondarev, D. A. Vinokurov, V. A. Kapitonov, O. V. Kovalenkov, Z. N. Sokolova, and I. S. Tarasov

A. F. Ioffe Physicotechnical Institute, Russian Academy of Sciences, St. Petersburg
(Submitted February 25, 1998)
Pis'ma Zh. Tekh. Fiz. **24**, 46–51 (November 26, 1998)

An investigation was made of the possibility of using reduced-pressure MOC hydride epitaxy to fabricate highly strained (compressive stress) $In_xGa_{1-x}As/In_{0.53}Ga_{0.47}As$ quantum wells on indium phosphide (100) substrates. The photoluminescence properties of these heterostructures were investigated. It was shown that these heterostructures are potentially useful for laser diodes emitting in the 1.5–2 μm range, which is important for environmental monitoring. © *1998 American Institute of Physics.* [S1063-7850(98)02211-3]

The development of strained-layer semiconducting heterostructures for use in laser diodes has recently been studied intensively. These structures have attracted interest because of the substantial improvement in the emitting characteristics compared with those using lattice-matched materials.[1]

When quantum wells compressively strained in the heterojunction plane are used in the active region of a laser structure, this leads to substantial rearrangement of its energy band structure. The heavy hole subband becomes higher then the light hole subband and the effective mass of the heavy holes also decreases appreciably.[2] This reduces the density of states in the valence band, which helps to establish carrier inversion conditions at lower levels of excitation, and thus the threshold laser current density can be attained at lower current densities.

Strained materials formed by quantum wells in In–Ga–As–P are widely used in lasers for fiber-optic communications at wavelengths 1.3 and 1.55 μm. It is known that the use of strained InGaAs quantum wells in the active region of a laser structure can extend the range of emitted wavelengths to around 2 μm. This range is of interest for molecular spectroscopy and for monitoring atmospheric pollution, since it includes the absorption spectra of gases such as CH_4, CO_2, CO, NH_3, HF, HBr, and HCl. However, strained heterostructures in In–Ga–As–P emitting at unconventional wavelengths between 1.6 and 2 μm have not yet been investigated in detail in the literature.

In order to extend the emission range of InGaAs/InGaAsP/InP lasers toward 2 μm, the active region must incorporate highly strained (compressive stress) layers of InGaAs ternary solid solution with a high indium content.

The present paper is concerned with the fabrication and investigation of $In_xGa_{1-x}As$ quantum wells with an indium content between 0.6 and 0.85. Although a set of quantum wells is generally required in the active region to obtain efficient laser structures, single-well structures are more convenient for studying the growth conditions and the quality of the heterostructure.

Here the samples were grown by vapor-phase epitaxy from metalorganic compounds and hydrides (MOC hydride epitaxy) at reduced pressure (100 mbar) using a horizontal reactor with an rf-heated graphite substrate holder. The growth temperature, determined from the readings of a platinum–platinum–rhodium thermocouple, was 600 °C. We know that a low growth temperature is preferable for growing strained indium-containing quantum wells in order to minimize the indium segregation from the heterojunction.[5] The substrates were $(100)\pm 30'$ oriented indium phosphide wafers. Before being loaded into the reactor, the substrates were degreased by boiling in toluene and acetone, and were treated with potassium bichromate–hydrogen bromide etchant to remove the damaged layer. The carrier gas was hydrogen purified by diffusion through a multistage palladium filter. The initial reagents were trimethylgallium, trimethylindium, arsine (AsH_3), and phosphine (PH_3) diluted in hydrogen. The molar concentration of trimethylindium in the carrier gas stream was maintained at 6.2×10^{-5} while the trimethylgallium concentration was varied in the range $(0.8–3)\times 10^{-5}$, depending on the composition of the $In_xGa_{1-x}As$ solid solution.

The grown samples were intentionally undoped heterostructures, formed by a 0.2 μm thick InP buffer layer, followed by a 0.2 μm thick $In_{0.53}Ga_{0.47}As$ lower barrier layer lattice-matched with the substrate, a 20–100 Å thick $In_xGa_{1-x}As$ quantum well with an indium content between 0.6 and 0.85, and a 0.2 μm thick $In_{0.53}Ga_{0.47}As$ upper layer. The stresses in the quantum well caused by the mismatch of the lattice parameters were between 0.5% and 2% depending on the indium content in the well. The ratio of group V and III elements in the reactor volume was 300 for growth of the InP layer and 60–85 for growth of the solid solution layer.

Although the height of the energy barriers was insufficient to achieve efficient photoluminescence, the barrier layers were formed by the substrate-matched ternary solid solution to avoid any indeterminacy of the composition at the barrier–quantum well interface caused by intensive substitution of arsenic and phosphorus atoms in the group V sublattice at each heterojunction.[3,4]

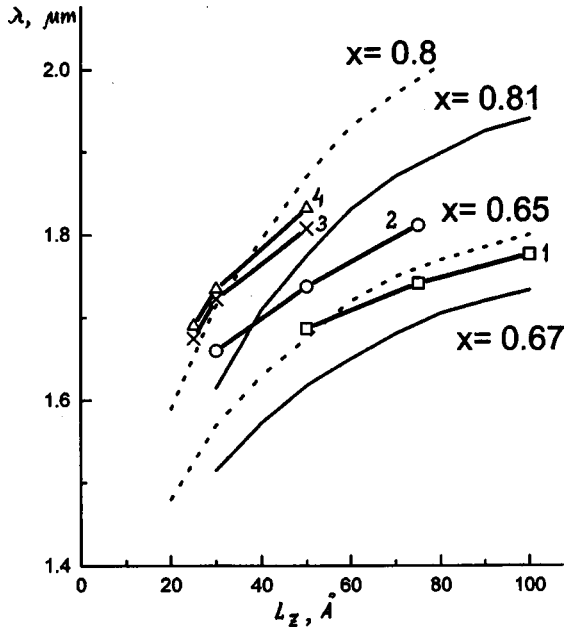

FIG. 1. Wavelength λ at the maximum of the photoluminescence spectrum (300 K) of $In_xGa_{1-x}As/In_{0.53}Ga_{0.47}As$ quantum wells as a function of the thickness (L_z): *1* — $x=0.69$, *2* — $x=0.73$, *3* — $x=0.76$, and *4* — $x=0.81$. Solid curves — calculated data from Ref. 1 and dashed curves — experimental data from Ref. 5.

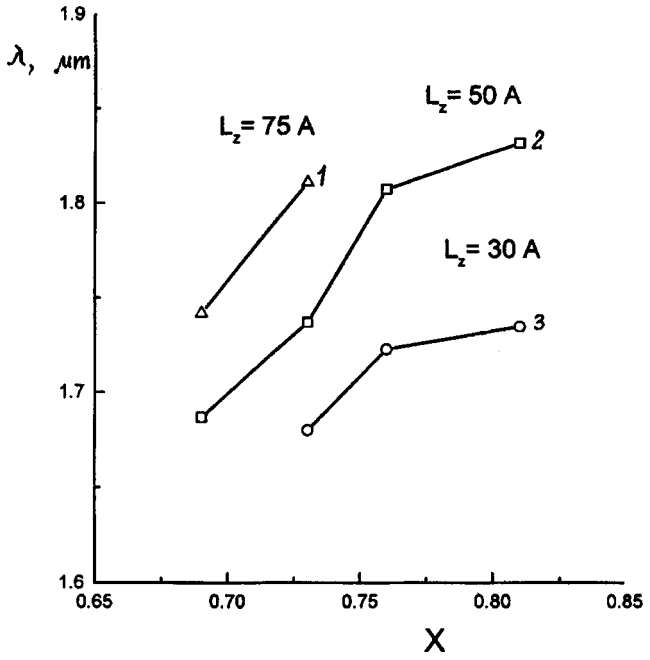

FIG. 2. Wavelength λ at the maximum of the photoluminescence spectrum (300 K) of $In_xGa_{1-x}As/In_{0.53}Ga_{0.47}As$ quantum wells as a function of the solid-solution composition x: triangles — $L_z=75$ Å, squares — $L_z=50$ Å, and circles — $L_z=30$ Å.

The samples were investigated by the photoluminescence method at room temperature (300 K) and liquid-nitrogen temperature (77 K). The source of exciting radiation was a $\lambda=0.488\,\mu$m argon laser. Figure 1 gives the maximum of the photoluminescence wavelength of $In_xGa_{1-x}As/In_{0.53}Ga_{0.47}As$ quantum wells as a function of their thickness. The dashed curves with indium contents $x=0.8$ and $x=0.65$ in the well show the theoretical calculations for $n=1$ electron–heavy hole transitions from Ref. 1. In their calculations Thijs *et al.*[1] used an InGaAsP quaternary solid solution with $\lambda=1.15\,\mu$m as the barrier layers. The solid curves show the experimental results from Ref. 5. The symbols represent our experimental data for indium contents in the quantum well $x=0.81$, 0.76, 0.73, and 0.69, respectively. The smaller slope of our curves can easily be explained if we bear in mind that when a substrate-matched $In_{0.53}Ga_{0.47}As$ ($\lambda=1.6\,\mu$m) solid solution is used as the barrier layers, we have a substantially shallower quantum well and for thin wells the first size-quantized level is fairly close to the energy position of the barrier. The appreciable difference between the results of Refs. 1 and 5 can be attributed to the nonideal nature of the heterojunctions caused by indium segregation. Figure 2 shows our experimental findings for the photoluminescence wavelength of quantum wells of different thickness obtained at 77 K as a function of the solid solution composition in the well. An analysis of Fig. 2 reveals that in order to obtain an emission wavelength of the order of 2 μm, the active region must contain highly strained quantum wells with a mismatch of around 2% ($x=0.82$) and thicknesses around 100 Å.

We have investigated highly strained (compressive stress) $In_xGa_{1-x}As/In_{0.53}Ga_{0.47}As$ quantum wells grown by reduced-pressure MOC hydride epitaxy. The results have shown that this heterostructure is potentially useful for laser diodes emitting in the range 1.5–2 μm.

This work was partially supported by Project No. 96-2005 under the Russian National Program ''Physics of Solid-State Nanostructures'' and by Grant No. 98–02–18266 from the Russian Fund for Fundamental Research.

[1] P. J. A. Thijs, L. F. Tiemeijer, J. J. M. Binsma *et al.*, IEEE J. Quantum Electron. **30**, 477 (1994).
[2] S. L. Chuang, Phys. Rev. B **43**, 9649 (1991).
[3] M. Mesrine, J. Massies, E. Vanelle *et al.*, Appl. Phys. Lett. **71**, 3552 (1997).
[4] M. Taskinen, M. Sopanen, H. Lipsanen *et al.*, Surf. Sci. **376**, 60 (1997).
[5] J. Dong, A. Ubukata, and K. Matsumoto, Jpn. J. Appl. Phys., Part 2 **36**, 5468 (1997).

Translated by R. M. Durham

Field ion microscope examination of the action of an intense ion flux from a laser plasma on tungsten

A. L. Suvorov, Yu. N. Cheblμkov, A. F. Bobkov, S. V. Zaĭtsev, S. V. Latyshev, E. N. Skorokhodov, and A. E. Stepanov

Institute of Theoretical and Experimental Physics, Moscow
(Submitted June 19, 1998)
Pis'ma Zh. Tekh. Fiz. **24**, 52–57 (November 26, 1998)

Results are presented of field ion microscope examinations of the structure of tungsten samples exposed to the action of a high-intensity ion flux ($\sim 10^{22}$ ions/cm$^2 \cdot$s) from a lead laser plasma. It was observed that the surface layer becomes amorphized and the defect spectrum was established. The limiting mechanical properties of irradiated tips were determined. Promising directions for further research are indicated.
[S1063-7850(98)02311-8]

Studies of the interaction between a laser plasma and a solid surface are of interest because this can simulate the degradation of materials in nuclear fusion facilities currently under construction. An important factor is that these experiments allow us to study the action of short, high-intensity ion current pulses on structural materials until they fail completely.

The aim of the present study was to use a field ion microscope[1] to examine the defect structure of tungsten samples exposed to the action of a lead plasma produced by a pulsed CO_2 laser. During the experiment the lead target was inclined at a small angle to the axis of the laser beam and the laser flare was directed onto standard field ion microscopy tips. The distance between the lead target and the irradiated surface of the tips was varied between 4 and 14 mm. All the samples were irradiated simultaneously. The lead ion fluence at the tips was $\sim 10^{16}$ ions/cm^2 per laser pulse at a distance of 4 mm and $\sim 10^{15}$ ions/cm^2 at 12 mm. Most of the ions had an energy of around 0.5 keV.

The irradiation parameters were calculated using a quasi-two-dimensional hydrodynamic model of an expanding laser plasma[2] for the CO_2 laser used in the experiments (laser beam energy ≈ 3 J, diameter of focusing spot ≈ 1 mm, pulse length ≈ 1 μs). This model has been successfully used to calculate the charge state of the ions in an expanding laser plasma,[3] the temperature of a laser plasma,[4] and various recombination effects.[5] Calculations for collector experiments[6] have shown that although the quasi-two-dimensional model simulates the lateral plasma flow only very roughly, it is suitable for calculating the ion current density in an expanding plasma to within a factor of 1.5–2.0.

When the distances between the samples and the lead target were short (4–8 mm), their external form in an optical microscope clearly reflected the mechanical and thermal action. The mechanical action showed up as plastic bending and fracture at the tip apexes with the fracture surface corresponding to brittle fracture. Increasing the distance between the tips and the lead target to 10–14 mm (i.e., reducing the power) had the result that the tips exhibited no fracture, but a thin fused surface layer appeared at the tips accompanied by the formation of a characteristic sphere as a result of capillary surface forces.

In all cases, the samples underwent additional electropolishing to taper the apex before their structures were analyzed using a field ion microscope. The field ion microscope investigations of the defect structure were carried out by a standard technique[7] using calculations and computer modeling.[8] The microscope images of many surface atomic layers near the initial apex of the tip revealed complete disorder, although they indicated the presence of some structure nuclei (Fig. 1). An analysis of these images suggests that an appreciable surface layer of the samples has become amorphized. This is evidently caused by the ultrafast cooling of part of the tip after the end of the ion pulse. Estimates showed that the apex of the tip was cooled mainly by radiation rather than by heat transfer through the solid part of the material, and this was aided by the high specific surface area of this region. We assume that the rate of cooling dT/dt is approximately

$$dT/dt = 2\sigma T^4/(3kn_0R_0),$$

where T is the sample temperature, σ is the Stefan–Boltzmann constant, k is the Boltzmann constant, n_0 is the number of tungsten atoms per unit volume, and R_0 is the radius of the tip. At the melting point of tungsten ($T_m \approx 3700$ K) and $R_0 \leqslant 0.5$ μm the cooling rate can exceed $dT/dt > 10^7$ deg/s, which is sufficient to prevent crystallization, even of pure metals.[9]

As many surface atomic layers are evaporated by the field, the images increasingly reveal a crystal structure beginning with layers approximately 0.5–1.0 μm from the initial irradiated surface. In this case, a broad spectrum of defects can be identified, beginning with isolated point defects (vacancies and interstitial atoms in complexes with impurity atoms[10]) and complexes of low multiplicity, and extending to dislocations, dislocation loops, and microcracks. The significant disorder of the sample structure decreased and ultimately, for most samples we obtained images demonstrating a high-quality crystal structure.

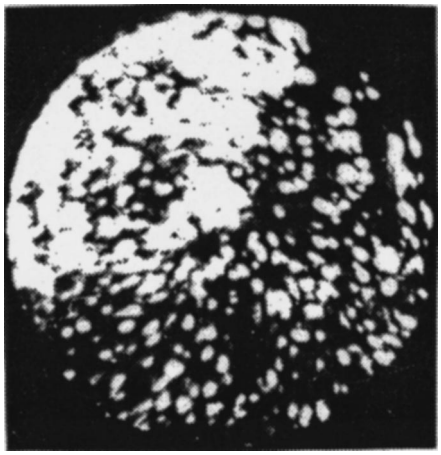

FIG. 1. Typical field-ion image of the surface of an irradiated sample showing amorphization of the structure near the irradiated surface.

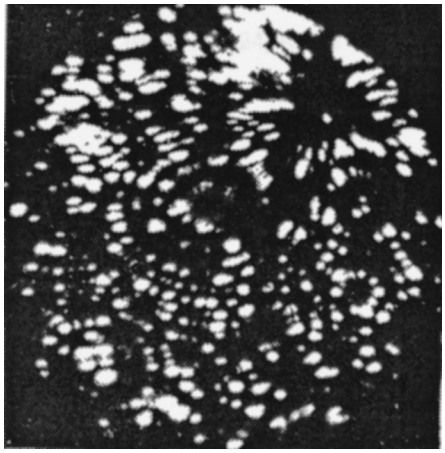

FIG. 3. Field-ion image of the structure of an irradiated sample at a depth of $\sim 0.3\ \mu$m from the irradiated surface.

Figure 2 shows a typical field-ion image of the transition region of an irradiated sample. Arrow *1* indicates a micropore, arrow *2* indicates a dislocation with the Burgers vector $\mathbf{b}=a[100]$ near the central pole (011), and the arrows *3* indicate a grain boundary. The average depth of the transition region was 1.0–3.0 μm. Figure 3 gives an example of a field ion image of a more perfect structure. Only the upper right section reveals a micropore with average linear dimensions of 2.0–6.0 nm, which is clearly elongated in the [110] crystallographic direction. We emphasize that most of the micropores observed exhibited similar elongation, possibly attributable to the initial texture of the samples (wire blanks).

In some cases the field ion images of the irradiated samples revealed some ''rotation'' of various sections of atomic planes. This may well be caused by the formation of vacancy-type dislocation loop nuclei in {101} planes.[11] The mechanism for their formation as a result of the condensation of point defects was examined in detail in Ref. 12.

A method described by Suvorov[13] (rupture of tips by ponderomotive electric field forces) was used to determine the tensile strength for some of the irradiated samples. The average was $\sigma_T \geqslant 2100\ \mathrm{kg/mm^2}$, which clearly exceeds that for unirradiated samples[14] ($\sim 1950\ \mathrm{kg/mm^2}$).

To sum up, plasma treatment of tungsten tips can seriously degrade their structure to depths of $\sim 3.0\ \mu$m but may also have a positive influence on some properties of the material. Irradiation of tips will clearly be useful for studying possible nonlinear processes in solids by field ion microscopy. In addition, a laser plasma can be used to simulate the interaction between the bow section of spacecraft and planetary atmospheres. This is because the characteristic velocity ($\sim 10^6$ cm/s) of the ions in a laser plasma is the same as the escape velocity. By varying the distance between the target and the objects being studied, it is possible to create an ion flux density in the laser plasma equivalent to the gas flux density on the bow section of a spacecraft traveling at escape velocity at an altitude of 30–100 km above the surface of planets similar to Earth.

In conclusion, the authors are extremely grateful to A. N. Balabaev and A. N. Shumshurov for assistance with irradiating the samples.

This work was financed by the International Scientific and Technical Center as part of Project No. 467.

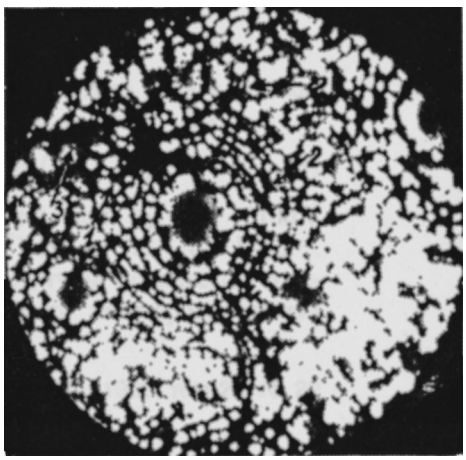

FIG. 2. Field-ion image of the structure of an irradiated sample at a depth of $\sim 0.5\ \mu$m from the irradiated surface (for description of arrows see text).

[1] E. W. Muller and T. T. Tsong, *Field Ion Microscopy. Principles and Applications* (Elsevier, New York, 1969).
[2] S. V. Latyshev, Preprint No. 66 [in Russian], Institute of Theoretical and Experimental Physics, Moscow (1983).
[3] A. A. Golubeva, S. V. Latyshev, and B. Yu. Sharkov, Kvantovaya Élektron. (Moscow) **11**, 1854 (1984) [Sov. J. Quantum Electron. **14**, 1242 (1984)].
[4] S. V. Latyshev and I. V. Rudskoĭ, Preprint No. 2 [in Russian], Institute of Theoretical and Experimental Physics, Moscow (1986).
[5] S. V. Bobashev, S. V. Latyshev, I. V. Rudskoĭ *et al.*, Fiz. Plazmy **13**, 1383 (1987) [Sov. J. Plasma Phys. **13**, 801 (1987)].
[6] S. V. Latyshev and Yu. N. Cheblukov, Zh. Tekh. Fiz. **68**, 28 (1998) [Tech. Phys. **43**, (1998)].
[7] A. L. Suvorov, *Field Ion Microscopy of Radiation Defects in Metals* [in Russian], Énergoizdat, Moscow (1982).
[8] A. L. Suvorov, T. L. Razinkova, and A. G. Sokolov, Phys. Status Solidi A **61**, 11 (1980).
[9] I. V. Zolotukhin and Yu. V. Barmin, *Stability and Relaxation Processes in Metallic Glasses* [in Russian], Metallurgiya, Moscow (1991).

[10] A. L. Suvorov and D. E. Dolin, Appl. Surf. Sci. **94/95**, 384 (1996).
[11] S. V. Zaĭtsev, and A. L. Suvorov, Poverkhnost' No. 9, 104 (1985).
[12] J. P. Hirth and J. Lothe, *Theory of Dislocations* (McGraw-Hill, New York, 1967; Atomizdat, Moscow, 1972).
[13] A. L. Suvorov, *Structure and Properties of Surface Atomic Layers of Metals* [in Russian], Energoatomizdat, Moscow (1990).
[14] A. L. Suvorov *et al.*, At. Energ. **38**, 412 (1975).

Translated by R. M. Durham

Shear viscosity in a binary system with a spinodal

E. V. Kalashnikov and A. G. Ambrok

Institute of Problems in Mechanical Engineering, Russian Academy of Sciences, St. Petersburg
(Submitted June 15, 1998)
Pis'ma Zh. Tekh. Fiz. **24**, 58–63 (November 26, 1998)

An analysis is made of the temperature–concentration dependence of the viscosity of a binary liquid in contact with a solid wall. The region of liquid–wall contact is analyzed using the multilayer Ono–Kondo model. It is shown that in the temperature–concentration range bounded by a spinodal, the viscosity increases abruptly. © *1998 American Institute of Physics.* [S1063-7850(98)02411-2]

1. One quantity associated with irreversible effects and especially with energy dissipation effects, is the viscosity. Dissipation of energy accompanies various types of internal motion in a system and also processes involving the formation and evolution of structures in the system. In this respect, the viscosity cannot be considered independently of the internal structure of the system. The structure determines the viscosity of the system and the viscosity determines the evolution of the structure in the system. This interrelationship shows up particularly clearly in strongly correlated systems. To be specific we shall talk of a binary liquid consisting of two types of atoms A and B. In critical effects we know that the correlation length increases as a certain critical ''upper'' temperature is approached. In this case, the viscosity also increases.[1,2] However, calculations of the viscosity in systems near the critical temperatures are based on fluctuation theory whose validity is controlled by the Ginzburg relation[3]

$$\langle (x-x_0)^2 \rangle \ll x_0^2, \tag{1}$$

where x is the order parameter, i.e., the concentration of component B in a binary system A–B. This condition states that the deviation of a fluctuating quantity x should be small compared with the average x of this quantity. In this case, the expression for the viscosity η reduces to the well-known Einstein–Stokes relation:[1,2]

$$\eta = T/(6RD\pi), \tag{2}$$

which links the viscosity and the diffusion, where T is the absolute temperature, R is the correlation length, and D is the interdiffusion coefficient. In many cases however, condition (1) is violated and relation (2) is not satisfied.[4] These conditions are violated when the system contains a spinodal[5] at whose boundaries the system is unstable. In general, the diffusion coefficient D can be expressed in terms of the second derivative of the thermodynamic potential G with respect to concentration:[6,7]

$$D \sim \partial^2 G/\partial x^2. \tag{3}$$

Below the spinodal we find $D<0$. This yields negative values of the viscosity, as given by Eq. (2), which are physically meaningless.[8] Condition (1) does not determine the temperature–concentration bounds within which the condition for smallness of the fluctuations is satisfied. Analyses of viscosity under conditions of strong instability such as conditions where the system moves below the spinodal require different approaches, which allow the viscosity behavior to be analyzed independently of the diffusion.

In our view, an approach based on Newton's law is a possibility.[8] In this approach, viscous friction forces ΔF are created between layers of liquid moving at different velocities. These forces are proportional to the velocity difference $V_2 - V_1$ and are inversely proportional to the distance between the layers, $n_2 - n_1$. In this case, the viscosity η may be regarded as the reaction of the system to an external perturbation ΔF:

$$\eta = \Delta(n_2 - n_1)/(V_2 - V_1)\Delta f, \tag{4}$$

where Δf is the contact area of the layers.

2. The form of relation (4) suggests a model (Fig. 1) that can be used to analyze the viscosity η as a function of temperature and composition. This is the Ono–Kondo model of monatomic layers[9] used to analyze the characteristics of the formation of an interface.[5] Let us assume that a binary liquid at rest is bounded by a planar solid wall. Let us then divide the region of liquid adjacent to the wall into layers such that in each monatomic layer the atoms of components A and B are distributed randomly. Depending on the interatomic interaction energy and its ratio to the temperature, the number of monatomic layers filling the region of liquid forms a transition zone.[5] This zone is described by the dependence of the concentration of atoms of component B in the t th layer on the concentration of atoms of the same component in the bulk (or average concentration).[5] In the $(t+1)$th layer, the concentration is the same as the bulk value. Figures 2a and 2b show isotherms of the number of layers forming the transition zone and the γ energy of ''interphase'' attraction between the liquid and the solid wall as a function of the average concentration x. The spinodal and binodal are plotted in terms of the isotherms γ. These curves demarcate the thermodynamic states of a homogeneous liquid solution into stable, metastable, and unstable (labile). We shall shift the liquid (Fig. 1) with the same momentum $p = \Delta F/(V\Delta f)$ for each average composition and temperature. Then, assuming that the velocity V_1 of the first layer $(t=1)$ adjacent to the wall is zero, we can write an expression to calculate the viscosity of the system in the form

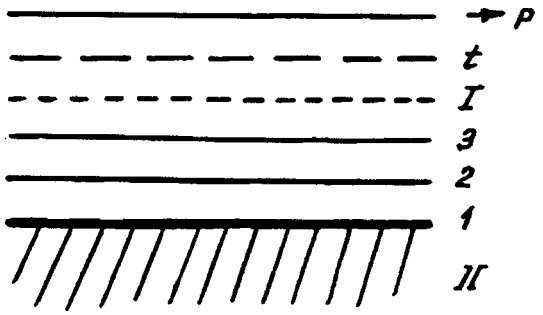

FIG. 1. Model of contact between liquid solution and wall: *I* — liquid, *II* — wall. The liquid boundary layer is divided into t monatomic layers; layer $t=1$ is in contact with the wall.

$$\eta=(n_t-n_1)p. \tag{5}$$

Figure 2d gives the temperature–concentration dependences of the viscosity (3) calculated using the temperature–concentration dependences of the numbers of monatomic layers forming the transition zone (Figs. 2a and 2b). A comparison of the curves plotted in Fig. 2 reveals that in the temperature–concentration range enclosed by the spinodal, the viscosity increases abruptly, approximately by an order of magnitude. In this region the system is strongly correlated.[10] The ensuing concentration inhomogeneity embraces the entire system immediately, forming no interfaces. Not only are no interfaces formed, which would correspond to the equilibrium coexistence of the solutions described by the binodal, but also the interface between the wall and the liquid is destroyed. The formation of interfaces is forbidden because of the characteristic form of the van der Waals dependence of γ (Fig. 2) at temperatures below the critical value T_c (below the spinodal $\partial\gamma/\partial x>0$). The increased viscosity prevents the system from leaving the spinodal, leaving it strongly correlated, without any interfaces, and inhomogeneous. If the system lies in the region of metastable or stable states, the correlation length is small.[10] In this case, the viscosity completely obeys the Einstein–Stokes relation.[4,6] Under these conditions a ''good'' interface exists between the binary liquid and the wall. This implies that $\partial\gamma/\partial x<0$ and for each composition x the first layer $(t=1)$ is anchored to the wall and $V_1=0$. In the region of metastable states, this interface may also be supplemented by other interfaces formed between solutions between which equilibrium is described by the binodal.

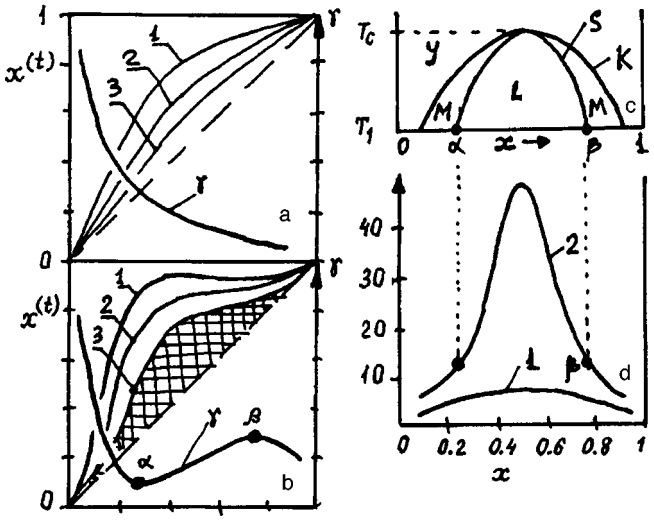

FIG. 2. Distribution of the concentration $x^{(t)}$ of component *B* in terms of monatomic layers t, surface tension γ, and viscosity η as a function of the concentration x of the same component in the bulk of the system for different temperatures (γ and η are given in arbitrary units): a — for $T>T_c$; b — for $T<T_c$. The concentrations are given in atomic fractions; the numbers of monatomic layers t are denoted by the numbers: $t=1,2,3,\ldots$; the shaded area corresponds to a sharp increase in the number of monatomic layers forming the transition zone, which for $T<T_c$ embraces the entire system. c — boundaries of different thermodynamic stability of the system; *C* — decay cupola (binodal); *S* — spinodal; St, M, L — stable, metastable, and labile states of uniform distribution of the components; d — concentration dependence of the viscosity η: curve *1* — for $T>T_c$, curve *2* — for $T<T_c$. Points α and β correspond to the spinodal at $T<T_c$.

3. The existence of temperature–concentration regions of different thermodynamic stability in a system is extremely important in structure formation effects. In particular, a substantial increase in viscosity within the limits bounded by the spinodal is an important criterion for glass-forming systems.[11] The existence of a spinodal leads to strong concentration inhomogeneity but the increase in viscosity prevents the formation of interfaces associated with separation and crystallization. This analysis of viscosity is not confined to a binary liquid solution–wall system. The model can also be applied to multicomponent and single-component systems considered in the ''hole'' approximation.[9] The latter presupposes that the model can be applied to a saturated vapor–substrate system.

The first author was partially supported by the Russian Fund for Fundamental Research (code 96–03–32396) and an Integration Grant (No. 589, Lead Organization, Institute of Problems in Mechanical Engineering, Russian Academy of Sciences) and the second was supported by the Russian Fund for Fundamental Research (Code 98–03–32791).

[1] M. Fixman, J. Chem. Phys. **36**, 310 (1962).
[2] K. Kawasaki and M. Tanaka, Proc. Phys. Soc. **90**, 791 (1967).
[3] K. Binder, Phys. Rev. A **29**, 341 (1984).
[4] Yu. S. Tver'yanovich, E. V. Kalashnikov, O. V. Il'chenko, and A. G. Ambrok, Fiz. Khim. Stekla **22**, 291 (1996).
[5] A. G. Ambrok and E. V. Kalashnikov, Rasplavy No. 4, 41 (1997).
[6] E. V. Kalashnikov and A. G. Ambrok, Rasplavy No 5, 13 (1996).
[7] N. March and M. Tosi, *Atomic Dynamics in Liquids* (Halsted Press, New York, 1977; Metallurgiya, Moscow, 1980, 296 pp.).
[8] L. D. Landau and E. M. Lifshitz, *Fluid Mechanics*, 2nd ed. (Pergamon Press, Oxford, 1987) [Russ. original, 3rd. ed, Nauka, Moscow 1986, 736 pp.].
[9] S. Ono and S. Kondo, *Molecular Theory of Surface Tension in Liquids* (Springer-Verlag, Berlin, 1960; IL, Moscow, 1963, 291 pp.].
[10] E. V. Kalashnikov and A. G. Ambrok, Pis'ma Zh. Tekh. Fiz. **23**(3), 84 (1997) [Tech. Phys. Lett. **23**, 124 (1997)].
[11] E. V. Kalashnikov, Yu. S. Tver'yanovich, and O. V. Il'chenko, Rasplavy No. 5, 80 (1996).

Translated by R. M. Durham

Dosimeter for real-time monitoring of nuclear radiation energy (dose) using a metal–gas-insulator–semiconductor structure

P. G. Kasherininov and A. N. Lodygin

A. F. Ioffe Physicotechnical Institute, Russian Academy of Sciences, St. Petersburg
(Submitted January 15, 1998)
Pis'ma Zh. Tekh. Fiz. **24**, 64–69 (November 26, 1998)

A new type of semiconducting dosimeter is proposed for real-time monitoring of nuclear radiation energy (dose). This dosimeter produces an electrical output signal directly proportional to the incident radiation dose (and not its intensity) and its sensitivity to this radiation dose can be controlled. © *1998 American Institute of Physics.* [S1063-7850(98)02511-7]

In Ref. 1 we described a new type of photodetector using metal–gas-insulator–semiconductor (MGIS) structures which produces an output signal proportional to the energy (dose) of the illumination incident on its working surface. Here we examine the possibility of using this type of structure to fabricate a dosimeter for real-time measurements of nuclear radiation energy (dose).

We investigated MGIS structures with a layer of air as the gas insulator using insulating bismuth silicate $Bi_{12}SiO_{20}$ (BSO) crystals having dark resistivity $\rho = 10^{12}$–$10^{14}\,\Omega\cdot$cm ($\Delta E = 3.28$ eV), free carrier mobility $\mu_m = 2\times10^{-2}$ cm$^2\cdot$V$^{-1}\cdot$s^{-1}, and lifetime $\tau_n = 10^{-4}$ s. The MGIS structures were fabricated using plane-parallel wafers measuring $10\times10\times2$ mm. On one of the 10×10 mm crystal surfaces we attached a 10×10 mm mica plate of thickness $l = 30$–100 μm with a 5–7 mm diameter aperture. The structure was sandwiched between glass plates on which transparent In_2O_3 electrodes were deposited. A dc voltage source $V_{00} = 0.6$–3 kV was connected to the electrodes of the MGIS structure (Fig. 1a). In the absence of illumination, the applied voltage is distributed between the structure layers according to their capacitances:

$$\frac{V_1}{V_0} = \frac{C_0}{C_1} = \frac{\varepsilon_0}{d_0}\frac{d_1}{\varepsilon_1}, \tag{1}$$

where V_0, C_0, ε_0, and d_0 are the voltage applied to the gas layer, and the capacitance, permittivity, and thickness of the gas layer, respectively, and V_1, C_1, ε_1, and d_1 are the voltage applied to the semiconducting layer, and the capacitance, permittivity, and thickness of this layer, respectively, where $V_0 + V_1 = V_{00}$. The electric field strengths in the gas layer E_0 and in the crystal E_1 are described by expressions (2) and (3), respectively:

$$E_0 = V_{00}/d_0(1/(1+\varepsilon_0 d_1/\varepsilon_1 d_0)), \tag{2}$$

$$E_1 = V_{00}/d_1(1/(1+\varepsilon_1 d_0/\varepsilon_0 d_1)). \tag{3}$$

Figures 1a and 1b show the distribution of the electric field in the BSO crystal E_1 and in the gas layer E_0 of this MGIS structure for parameters of the semiconducting layer $\varepsilon_1 = 40$, $d_1 = 2\times10^{-3}$ m and the gas insulator (air) $\varepsilon_0 = 1$, $d_0 = 8\times10^{-5}$ m, in the absence of illumination at $V_{00} = 2100$ V, as given by expressions (2) and (3). It can be seen from Fig. 1 that in this structure the electric field E_0 in the gas gap is an order of magnitude greater than that in the crystal E_1 ($E_0 = 1.6\times10^7$ V/m, $E_1 = 0.9\times10^6$ V/m) and is close to the critical value E_{cr} (for a gas gap of thickness $d_0 = 8\times10^{-5}$ m, Bogoroditskiĭ *et al.*[2] give $E_{cr} = 2.7\times10^7$ V/m). When the detector is irradiated, free carriers of the appropriate sign generated by the radiation in the crystal collect at the crystal–gas-layer interface under the action of the electric field. This reduces the electric field E_1^1 in the crystal and causes a corresponding increase in the field in the gas layer from the dark value E_0 to the critical level $E_0^1 = E_{cr}$. This is accompanied by an increase in the voltage drop in the gas layer and a reduction in the crystal by $\Delta V = (E_{cr} - E_0)d_0$. The electric field in the crystal E_1^1 is then given by (Fig. 2b)

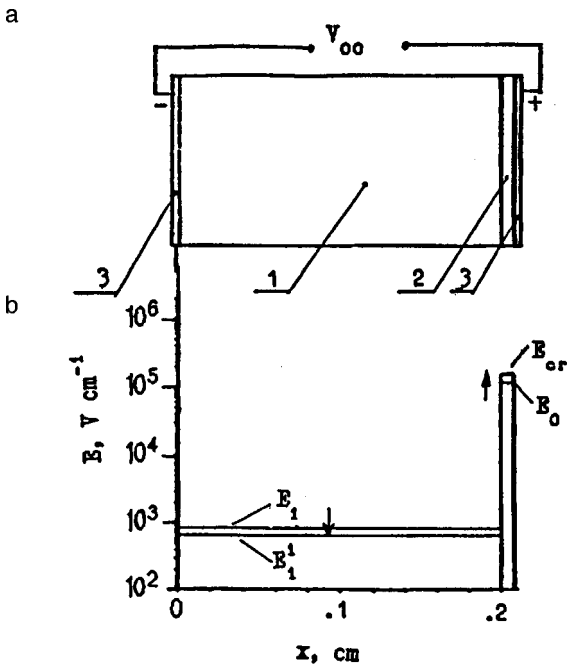

FIG. 1. Distribution of electric field strength in irradiated MGIS structure: a — diagram of structure: *1* — BSO crystal, *2* — layer of air insulator, *3* — optically transparent electrodes; b — distribution of electric field strength in structure in the dark (in the crystal E_1 and in the air gap E_0, respectively) and under irradiation just before the onset of gas breakdown (in the crystal $E_1 = E_1^1$) and in the air gap $E_0 = E_{cr}$, respectively.

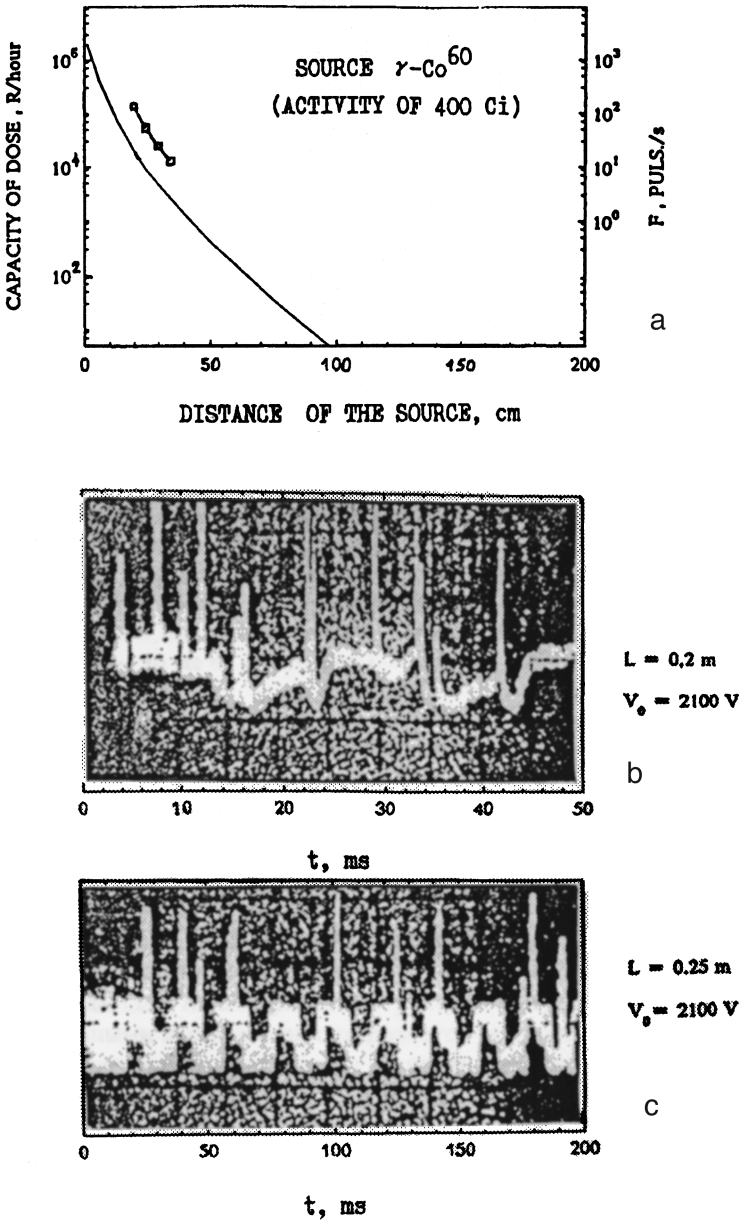

FIG. 2. Recording of γ radiation energy (dose) from Co^{60} γ source using dosimeter formed by BSO crystal MGIS structure: a — experimental dependence of current pulse frequency in dosimeter circuit as a function of distance from radioactive source (crosses); solid curve — calibration curve of γ radiation dose rate as a function of distance from Co^{60} γ source; b — photographs from oscilloscope screen showing profile of current pulses in dosimeter circuit at distance $L=0.2$ m from the source ($V_{00}=2100$ V); c — the same at distance $L=0.25$ m.

$$E_1^1=E_1-(E_{cr}-E_0)d_0/d_1 \tag{4}$$

and is $E_1^1=0.75\times10^6$ V/m.

When the structure is illuminated, the energy of the electric field in the gas gap (gas condenser) increases by ΔA:

$$\Delta A=0.5Cd_0^2(E_{cr}-E_0)^2=0.5\varepsilon_0 d_0(E_{cr}-E_0)^2. \tag{5}$$

For the structure geometry described above with $V_{00}=2100$ V ($E_0=1.6\times10^7$ V/m, $E_{cr}=2\times10^7$ V/m) we obtain $\Delta A=5.7\times10^{-3}$ J/m^2. For $E_0^1=E_{cr}$ a current pulse appears in the electric circuit of the structure caused by the capacitance of a section of the surface of the gas layer (an area around $(1–2)\times10^{-6}$ m^2) being discharged through the resistance of the illuminated part of the crystal. After this the electric field in the gas layer drops below the critical value, the discharge ceases, the field distribution in the structure returns to the initial state, and the process is repeated.

We showed[1] that cw irradiation of the structure is accompanied by a periodic flow of current pulses in the circuit. The radiation energy incident on the surface of the structure during the time between two successive pulses is determined by the voltage applied to the structure and does not depend on the radiation intensity.

These structures were tested as dosimeters irradiated by a 400 Ci Co^{60} source of γ activity positioned at the bottom of a water-filled tank. The dosimeter in a sealed capsule was moved closer to the source at various distances L.

Figure 2 gives results of investigating the frequency F of the current pulses in the dosimeter circuit as a function of the dose rate. The solid curve in Fig. 2a gives the calibration characteristic of the source and the crosses give the experimental points corresponding to the frequency F of the dosimeter current pulses at $V_0=2100$ V for various distances L from the radioactive source. It can be seen from Fig. 2a that the experimental dependence $F(L)$ is parallel to the calibration curve, which indicates that the pulse frequency depends linearly on the dose rate $F(B)$ in this range of L. Figures 2b

and 2c show photographs from the screen of an oscilloscope which illustrate the profile of the current pulses at distances $L=0.2$ m (b) and $L=0.25$ m (c) from the source. We confirmed that this BSO crystal dosimeter could record radiation at dose rates $B=(3\times10^{-2})$–(3×10^{3}) R/s. The radiation dose recorded by the dosimeter over the interval between pulses at this voltage is $C=(3–4)\times10^{-2}$ R according to these photographs.

Thus, MGIS structures using wide-gap insulating crystals can be used to fabricate a new type of dosimeter for radiation from radioactive sources, which is capable of making real-time measurements of the radiation energy (dose) incident on objects with a high radiation background.

The proposed type of dosimeter has the following features:

1) It can directly record the energy (dose) of the incident radiation;

2) The sensitivity to radiation energy (dose) can be varied widely by varying the applied voltage;

3) It can be used to record the energy (dose) of radioactive radiation at high dose rates $B=10^{-2}$–10^{3} R/s;

4) It has a high radiation resistance because it uses highly compensated crystals with an impurity level concentration $N>10^{17}\,\mathrm{cm}^{-3}$;

5) It has a high signal-to-noise ratio obviating the need for radiation-sensitive electronics at the dosimeter site;

6) Crystals with low values of the parameter $\mu\tau>10^{-7}\,\mathrm{cm}^{2}/\mathrm{V}$ can be used (new wide-gap materials, low-quality crystals);

7) The dosimeter is universal and can be used to record a broad spectrum of radiation energy from hard γ rays to light;

8) It can be used as a sensor in automatic dose switches which transmit fixed doses of recorded radiation energy regardless of intensity;

9) The dosimeter has a simple design and is convenient to operate because information on the radiation conditions is delivered by a series of pules.

[1] P. G. Kasherininov and A. N. Lodygin, Pis'ma Zh. Tekh. Fiz. **23**(3), 23 (1997) [Tech. Phys. Lett. **23**, 137 (1997)].
[2] N. P. Bogoroditskiĭ and V. V. Pasynkov, *Materials in Radio Electronics* [in Russian], Gosénergoizdat, Moscow (1961), 352 pp.

Translated by R. M. Durham

Enhancement of the quantum efficiency of radiative recombination of the fullerene C_{70} in a toluene solution

Yu. F. Biryulin, L. V. Vinogradova, and V. N. Zgonnik

A. F. Ioffe Physicotechnical Institute, Russian Academy of Sciences, St. Petersburg
(Submitted May 15, 1998)
Pis'ma Zh. Tekh. Fiz. **24**, 70–75 (November 26, 1998)

An investigation of the spectra and quantum efficiency of photoluminescence provided direct evidence of the presence of C_{70} aggregates in a toluene solution. Toluene solutions of C_{60} and C_{70} in the proportion 1 g/l and artificial mixtures of these were studied. The hypothesis is put forward that mixed aggregates of C_{60} and C_{70} exist. © *1998 American Institute of Physics.* [S1063-7850(98)02611-1]

The unique physical and physicochemical properties of new carbon clusters, the fullerenes C_{60} and C_{70}, have been noted by many researchers.[1,2] One characteristic feature of their behavior is the anomalous temperature dependence of the solubility of C_{60} in toluene[3] and also the capacity of C_{70} molecules to organize themselves into aggregates in various organic solvents.[4]

In studies of the photoluminescence of toluene solutions of C_{60}, C_{70}, and mixtures of these, we observed some specific features in various photoluminescence characteristics which indicate that these solutions deviate from the criteria characteristic of true solutions.[5] These specific features are discussed here.

Chemically pure toluene which had undergone special additional dehydration, was used to prepare solutions of C_{60}, C_{70}, and artificial mixtures of these. Since C_{60} and C_{70} possess different solubility in toluene, it was decided to prepare the initial solutions in the ratio 1 mg per 1 ml. This also simplified the process of obtaining artificial mixtures.

These initial toluene solutions of C_{60} and C_{70} were then used to prepare artificial mixtures in the following ratios by weight: C_{60}:C_{70}=25:75, 50:50, 75:25, 90:10, 95:5, 98:2, and 99:1. In addition, toluene-diluted C_{60}:toluene and C_{70}:toluene mixtures in the ratios 75:25, 50:50, and 25:75 by weight were also prepared from the initial toluene solutions of C_{60} and C_{70} for analysis and comparison of the results.

All the prepared solutions were placed in molybdenum glass ampoules and sealed.

Photoluminescence from the solutions was excited by argon laser radiation at 488 nm and at 514 nm. During the experiments the specific power of the optical excitation could be varied by two orders of magnitude. All the photoluminescence measurements were made at room temperature.

The photoluminescence spectra of solutions of C_{60}, C_{70}, and their mixtures, obtained under identical conditions, are shown in Fig. 1.

The initial points for comparison of the photoluminescence parameters involved comparing the shape of the photoluminescence spectra, their intensities at 721 and 693 nm, and the relative quantum yield (i.e., the area bounded by photoluminescence curve). For comparison we used C_{60} and C_{70} films on silicon deposited by sublimation.[6] We established that the photoluminescence intensity and its quantum yield for the solid C_{60} films is an order of magnitude lower than the corresponding parameters of the initial C_{60} solution, and for C_{70} this difference exceeds two orders of magnitude.

In order to compare the effective masses of the fullerenes participating in the radiative recombination process, we made suitable estimates for the films and the solutions. These took into account the diameter of the optical radiation spot: its depth of absorption ($0.1\,\mu$m for the film[7] and around 0.5 mm for the solution); the density of the film was taken to be $1.67\,g/cm^3$ (Ref. 8) and the density of the fullerenes in the initial solution was $0.001\,g/cm^3$. The calculations showed that around 10^{-9} g of fullerenes participate in the radiative recombination process in the film, compared with approximately 10^{-8} g for the solution. These calculations show good agreement when the photoluminescence parameters of the films and the initial C_{60} solutions are compared, and differ by approximately 1.5 orders of magnitude for C_{70} on account of the higher photoluminescence efficiency in the initial solution.

Figure 2a gives the relative intensity of the photoluminescence band at 693 nm and the relative quantum yield of the photoluminescence spectra for the initial C_{60} and C_{70} solutions and their mixtures as a function of the composition of the fullerene solution in toluene. The measurements are plotted in units of the intensity of this photoluminescence band and the area below the photoluminescence curve of the initial C_{70} solution in toluene. A sharp kink is clearly visible near 10% C_{70} and 90% C_{60} (1 mol C_{70} per 10.5 mol C_{60}). If the behavior of this system was consistent with that of true solutions,[5] this dependence would be linear without any kinks between 100% C_{60} and 100% C_{70}. This behavior therefore suggests that in the mixture solution interactions took place between molecules of two or three of the initial components: C_{60}, C_{70}, and toluene.

In order to check out this hypothesis and eliminate one of the components from the analysis, we took toluene-diluted initial solutions of C_{60} and of C_{70}. The dependences of the

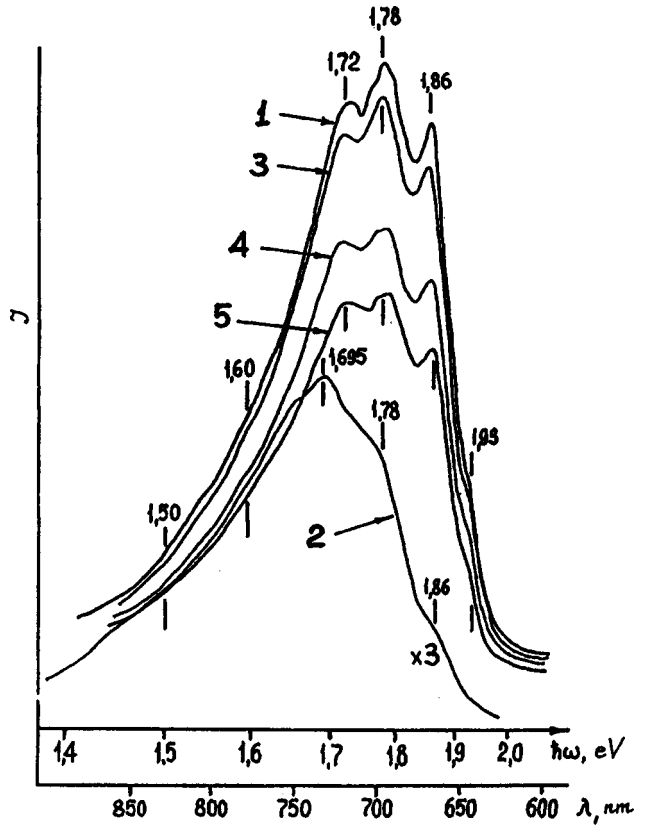

FIG. 1. Photoluminescence spectra of toluene solutions of C_{70} (*1*), C_{60} (*2*), and their artificial mixtures at 300 K. The $C_{70}:C_{60}$ ratio in the solutions of the mixtures was 75 : 25 (*3*), 50 : 50 (*4*) and 25 : 75 (*5*) wt.%.

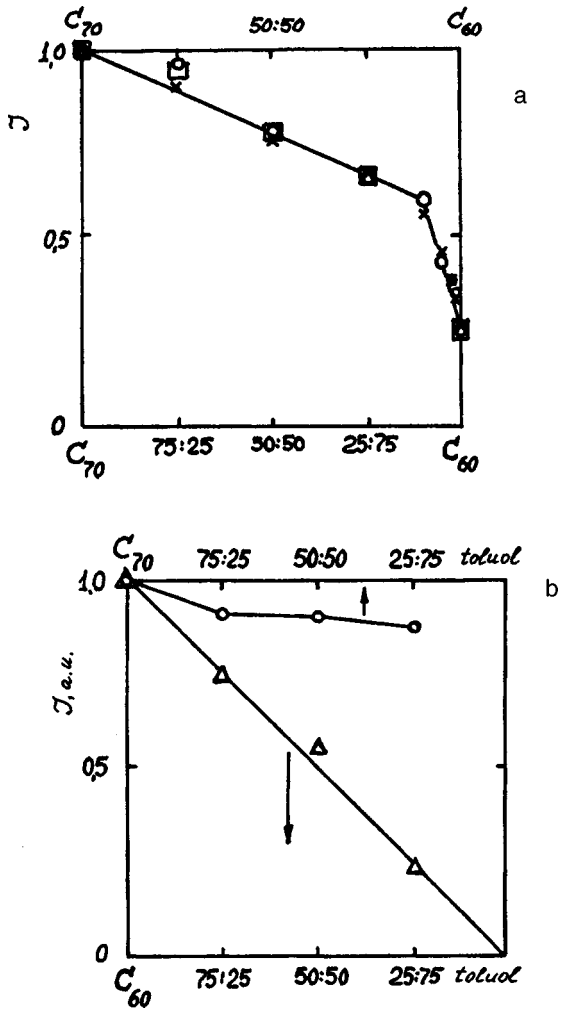

FIG. 2. a — Relative intensity of the 693 nm photoluminescence band (crosses and circles) and relative photoluminescence quantum yield (squares) for initial solutions of C_{70} and C_{60}, and their mixtures; b — relative photoluminescence intensity of the initial C_{70} and C_{60} solutions when diluted with toluene.

same photoluminescence parameters of these diluted solutions are plotted in Fig. 2b. It can be seen that the photoluminescence parameters of the initial C_{60} solution obey a linear dependence with increasing toluene dilution, i.e., they satisfy the criteria for true solutions.[5] The photoluminescence intensity of the diluted C_{70} solutions departs from linear. Thus, in this case the toluene molecules and C_{70} interact, causing disaggregation of the C_{70} aggregates.[4]

The difference in the behavior of C_{60} and C_{70} in solutions may be considered in terms of changes in the electron affinity which characterizes the activity of molecules and atoms, in the order C, C_{60}, and C_{70}. Data given by Boltalina *et al.*[9] indicate that the electron affinity in these increases in the order 2.5, 2.65, and 2.70 eV. Thus, in this series C_{70} must be acknowledged to be the most active in terms of acceptor properties. We can postulate from the data plotted in Fig. 2a that this interaction between C_{70} molecules and toluene extends to the range of concentrations between 100% and 10% C_{70}. In this last case, the solution contains 90% C_{60} but the photoluminescence spectrum as before only exhibits bands assigned to radiative recombination of C_{70} (Ref. 10). This is probably because as a result of the lower symmetry of C_{70} compared with C_{60} and also as a result of the interaction between the solvent molecules and C_{70}, the degeneracy in the C_{70} electronic levels is lifted, which helps to increase the quantum efficiency of the photoluminescence. This may be caused by an increase in the equilibrium fraction of the solvated form of C_{70}. Starukhin *et al.*[10] neglected the interaction between C_{70} molecules and the solvent when analyzing their results, or they assumed that it was fairly weak (van der Waals interaction).[11]

Tomiyama *et al.*[12] also examined the solubility of C_{60} and C_{70} in toluene. They detected no characteristic features in the solubility and partial volumes of C_{60} (up to 1.5 mg/ ml) and C_{70} molecules (up to 0.5 mg/ ml). This does not contradict our results, since we are concerned with C_{70} concentrations of 1 mg/ml or less and we also considered mixed solutions where the C_{60} and C_{70} molecules may interact.

Since interaction between C_{70} molecules has been indirectly demonstrated by Mel'nikov *et al.*[4] we shall attempt to understand the essential features of this effect. First, it occurs for certain C_{70} concentrations, i.e., interaction between them alone cannot be excluded. Second, the presence of toluene molecules helps to enhance the photoluminescence quantum efficiency of C_{70} (taking into account the reduction in the C_{70} concentration when diluted with toluene). Third, interaction between C_{60} and C_{70} cannot be excluded from an analysis of our results.

Thus, we can conclude that an increase in the quantum

yield of C_{70} molecules in a toluene solution and also in a solution of mixed C_{60} and C_{70} may be caused by interaction of the C_{70} molecules and also by the presence of solvent molecules and C_{60}. That is to say, aggregates may exist, including mixed ones. The energies of these interactions are fairly low and are not reflected in the form and shape of the C_{70} photoluminescence spectra. From this we can infer that if the C_{60}:C_{70} molecular ratio is of the order of 10:1, the composition of the mixed aggregates changes, leading to a substantial reduction in the quantum efficiency of the C_{70} photoluminescence.

This work was carried out under the Russian Interbranch Scientific and Technical Program ''Fullerenes and Atomic Clusters'' as part of the ''Polymer'' Project.

[1] A. V. Eletskiĭ and B. M. Smirnov, Usp. Fiz. Nauk **163**(2), 33 (1993).
[2] V. P. Belousov, I. M. Belousova, V. P. Budtov *et al.*, Opt. Zh. **64**(12), 3 (1997).
[3] R. S. Ruoff, R. Malhota, and D. L. Huestis *et al.*, Nature (London) **362**, 140 (1993).
[4] A. B. Mel'nikov, A. V. Lezov, and E. I. Ryumtsev, Zh. Fiz. Khim. **71**, 946 (1997).
[5] C. A. Parker, *Photoluminescence of Solutions. With Applications to Photochemistry and Analytical Chemistry*. (Elsevier, New York, 1968; Mir, Moscow, 1972, 510 pp.).
[6] Yu. F. Biryulin, A. Ya. Vul', I. K. Ionova *et al.*, Fiz. Tverd. Tela (St. Petersburg) **37**, 3124 (1995) [Phys. Solid State **37**, 1722 (1995)].
[7] R. W. Pohl, *Optik und Atomphysik* (Springer-Verlag, Berlin, 1963; Nauka, Moscow, 1966, 552 pp.).
[8] A. F. Hebard, Annu. Rev. Mater. Sci. No. 23, 159 (1993).
[9] O. V. Boltalina, L. N. Sidorov, A. Ya. Borschevskii *et al.*, Rapid Commun. Mass Spectrom. **7**, 1009 (1993).
[10] A. N. Starukhin, B. S. Razbirin, A. V. Chugreev *et al.*, Fiz. Tverd. Tela (St. Petersburg) **37**, 1050 (1995) [Phys. Solid State **37**, 570 (1995)].
[11] B. S. Razbirin, A. N. Starukhin, A. V. Chugreev *et al.*, JETP Lett. **60**, 451 (1994).
[12] T. Tomiyama, S. Uchiyama, and H. Shinohara, Chem. Phys. Lett. **264**, 143 (1997).

Translated by R. M. Durham

Critical perturbations in a monostable active medium

A. A. Pukhov

Joint Institute of High Temperatures, Research Center for Applied Problems of Electrodynamics, Russian Academy of Sciences, Moscow

(Submitted May 19, 1998)
Pis'ma Zh. Tekh. Fiz. **24**, 76–80 (November 26, 1998)

An analysis is made of critical perturbations which initiate the evolution of instability in a monostable active medium described by a reaction–diffusion equation. A group-theoretical analysis of the problem yields an analytic expression for the energy of the critical perturbations. The results may be important for analyses of stability with respect to external perturbations of a wide range of active media. © *1998 American Institute of Physics.*
[S1063-7850(98)02711-6]

The initiation of instability buildup in strongly nonequilibrium physical systems (active media) by external perturbations is a threshold process.[1] Perturbations of sufficiently high energy $e>e_c$ excite the buildup of instability in a medium, but the critical energy e_c depends on the spatial and temporal extent of the perturbation.[2] The most ''dangerous'' for active media are local and pulsed perturbations having the minimum critical energy.[3] The action of a local pulsed critical perturbation in a whole range of active media is described by the nonlinear reaction–diffusion equation

$$\frac{\partial\theta}{\partial t}=\Delta\theta+f(\theta)+e_c\delta^D(r)\delta(t), \tag{1}$$

where $\Delta=r^{-(D-1)}(\partial/\partial r)r^{D-1}(\partial/\partial r)$ is the radial part of the Laplacian, r and t are the dimensionless coordinate and time, $D=1,2,3$ is the spatial dimension of the problem, $\delta^D(r)=(k_d r^{D-1})^{-1}\delta(r)$, k_D is a geometric factor ($k_1=1$, $k_2=2\pi$, $k_3=4\pi$), $\delta(r)$ is a delta function, and θ can be the temperature of the medium, the reagent concentration, the electric field, and so on, depending on the nature of the dissipative process (see Ref. 1 and the literature cited). To be specific, we shall subsequently take θ to be the temperature. The critical energy e_c and the nature of the nonlinear stage of instability evolution in these systems are completely determined by the form of the source function $f(\theta)$. For example, for bistable systems (see Fig. 1, curve *1*) a perturbation with $e>e_c$ can destroy the stable state of the medium $\theta=\theta_1$ and transfer it to the metastable state $\theta=\theta_3$ (Ref. 2). Methods of approximately calculating e_c and its dependence on the parameters of the problem for this case have now been studied in fairly great detail.[2,3]

However, in many situations the system loses bistability (the dissipation depends strongly on temperature, the differential conductivity increases abruptly, and so on[1,2]). The qualitative form of the dependence $f(\theta)$ for this case is given by curve *2* in Fig. 1. In fairly general form the nonlinear source function $f(\theta)$ may be written as[4]

$$f(\theta)=a\theta^m(\theta^n-b), \tag{2}$$

where m, n, a, and b are arbitrary positive quantities and $b=\theta_2^n$. Such a medium is monostable (with a single stable state $\theta=\theta_1=0$), and when the temperature θ exceeds the threshold θ_2 in a fairly large part of the medium, it undergoes runaway self-heating. This factor is responsible for the particular nature of the nonlinear stage of instability buildup in a monostable medium.[5] Group-theoretical concepts can be applied to find e_c in this case.[6,7] We shall assume that the exponents m and n are fixed and a and b are the controlling parameters of the problem. Equations (1) and (2) are then invariant with respect to the variable transformation group

$$\begin{aligned} t&=L^{2p}t',\\ r&=L^{p}r',\\ \theta&=L^{q}\theta',\\ e_c&=L^{q+Dp}e_c',\\ a&=L^{(1-m-n)q-2p}a',\\ b&=L^{nq}b', \end{aligned} \tag{3}$$

which comprise a group of expansions with the scale factor L. The exponents of the scale factors of the expansion are determined by the invariance of Eqs. (1) and (2) under the transformation (3) so that the new (primed) variables satisfy the same equations (1) and (2). This has the result that the group of transformations (3) contains the free parameters L, p, and q, which can have arbitrary values.

Physical reasoning indicates that the critical energy e_c in Eqs. (1) and (2) is only a function of a and b: $e_c=F(a,b)$. This relation should be invariant relative to the group transformation (3), i.e., $e_c'=F(d',b')$ (Ref. 8). We shall seek a solution in the form $e_c\propto a^r b^s$ (Ref. 9), where the exponents r and s need to be determined. We then have

$$e_c/a^r b^s=L^{p(2r+D)+q[(m+n-1)r+1-ns]}e_c'/a'^r b'^s \tag{4}$$

and from the condition of invariance $e_c/a^r b^s=e_c'/a'^r b'^s$ we obtain $p(2r+D)+q[1+(m+n-1)r-ns]=0$. Since p and q in Eq. (3) are arbitrary, we obtain single-valued expressions for the exponents: $r=-D/2$, $s=[1-D(m+n-1)/2]/n$. Thus, for the critical energy e_c we have

$$e_c\propto a^{-D/2}b^{[1-D(m+n-1)/2]/n}. \tag{5}$$

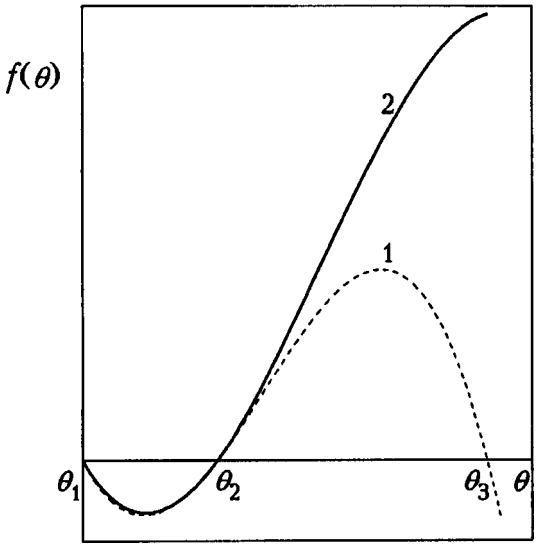

FIG. 1. Typical dependence of the nonlinear source function $f(\theta)$ on θ in bistable (curve *1*) and monostable (curve *2*) cases.

A coefficient of proportionality of order unity cannot be obtained for formula (5) using group concepts. This must be determined either by numerical calculations[4] or by applying additional reasoning.[9,10] Thus, a group-theoretical analysis of Eqs. (1) and (2) can yield a functional dependence of e_c on the controlling parameters for any dimensions of the problem.

It follows from formula (5) that as the threshold temperature $\theta_2 = b^{1/n}$ increases, the stability of a monostable medium with respect to external perturbations increases—for moderate values of m and n the critical energy e_c increases exponentially. We shall discuss this condition in greater detail. This method of calculating the critical energy e_c can be applied to active media whose specific heat and thermal conductivity depend strongly on temperature and which are described by

$$\theta^k \frac{\partial \theta}{\partial t} = \nabla(\theta^l \nabla \theta) + f(\theta) + e_c \delta^D(r)\,\delta(t). \tag{6}$$

Here we have $\nabla(\theta^l \nabla \theta) = r^{-(D-1)}(\partial/\partial r) r^{D-1} \theta^l (\partial \theta/\partial r)$. By applying the procedure described above to Eqs. (2) and (6), we obtain for the critical energy e_c

$$e_c \propto a^{-D/2} b^{[k+1-D(m+n-l-1)/2]/n}. \tag{7}$$

These media typically exhibit so-called ''peaking regimes.''[11] In particular, when the condition

$$m+n-k>1 \tag{8}$$

is satisfied, a ''thermal explosion'' occurs: the temperature of a fairly large, uniformly heated region of the medium (diffusion of heat from the boundaries is small compared with dissipation inside the region) goes to infinity within a finite time.[11] It can be seen from formula (7) that in this case, the dependence of the critical energy e_c on the threshold temperature $\theta_2 = b^{1/n}$ changes substantially. For example, for

$$m+n-k>1+2/D+l+k(2/D-1) \tag{9}$$

the energy e_c decreases exponentially with increasing θ_2, i.e., the stability of the medium deteriorates with increasing threshold temperature. Note that condition (9) may be more stringent than condition (8). The physical meaning of the correction in condition (9) is related to the local nature of the heating of the medium by the external perturbation. The perturbation energy is dissipated not only in heating and expanding the hot-phase region ($\theta \gtrsim \theta_2$) but also in the diffusion of heat from its boundaries. The rapid increase in the specific heat ($\sim \theta^k$) and the thermal conductivity ($\sim \theta^l$) impede the formation of a region of hot phase sufficient to initiate the buildup of instability.

The author is grateful to N. A. Buznikov for useful discussions of the results.

This work was supported by the State Scientific and Technical Program ''Topical Directions in the Physics of Condensed Media''(Project No. 96083) and the Russian Fund for Fundamental Research (Projects Nos. 96–02–18949 and 98–02–16046).

[1] V. A. Vasil'ev, Yu. M. Romanovskiĭ, and V. G. Yakhno, *Autowave Processes* [in Russian], Nauka, Moscow (1987), 240 pp.
[2] A. Vl. Gurevich and R. G. Mints, *Thermal Autowaves in Normal Metals and Superconductors* [in Russian], IVTAN, Moscow (1987), 168 pp.
[3] A. Vl. Gurevich, R. G. Mints, and A. A. Pukhov, Dokl. Akad. Nauk SSSR Ser. Fiz. **301**, 1104 (1988) [Sov. Phys. Dokl. **33**, 611 (1988)].
[4] S. V. Petrovskiĭ, Zh. Tekh. Fiz. **64**(8), 1 (1994) [Tech. Phys. **39**, 747 (1994)].
[5] A. A. Pukhov, Pis'ma Zh. Tekh. Fiz. **24**(11), 12 (1998) [Tech. Phys. Lett. **24**, 417 (1998)].
[6] N. H. Ibragimov, *Transformation Groups Applied to Mathematical Physics* (Reidel, Dordrecht, 1985) [Russ. original, Nauka, Moscow, 1983, 280 pp.].
[7] G. W. Bluman and S. Kumei, *Symmetries and Differential Equations* (Springer-Verlag, New York, 1989, 412 pp.).
[8] L. Dresner, *Similarity Solutions of Nonlinear Partial Differential Equations* (Pitman, London 1983, 60 pp.).
[9] L. Dresner, IEEE Trans. Magn. **21**, 392 (1985).
[10] N. A. Buznikov and A. A. Pukhov, Cryogenics **36**, 547 (1996).
[11] A. A. Samarskiĭ, V. A. Galaktionov, S. P. Kurdyumov, and A. P. Mikhaĭlov, *Peaking Regimes in Problems for Quasilinear Parabolic Equations* [in Russian], Nauka, Moscow (1987), 477 pp.

Translated by R. M. Durham

Influence of reduction on the behavior kinetics of optical inhomogeneities in $LiNbO_3$ single crystals

B. B. Ped'ko, É. V. Lebedev, and N. Yu. Franko

Tver State University, Department of Ferroelectric and Piezoelectric Physics
(Submitted March 26, 1998)
Pis'ma Zh. Tekh. Fiz. **24**, 81–85 (November 26, 1998)

An investigation was made of the influence of high-temperature annealing in vacuum on the optical homogeneity of $LiNbO_3$ single crystals. It was observed that the residual light transmission decreased appreciably and the temperature dependence of this parameter almost completely disappeared. © *1998 American Institute of Physics.* [S1063-7850(98)02811-0]

Lithium niobate crystals are widely used in optoelectronics. It is therefore of particular interest to study the properties of this crystal exposed to various types of treatment in order to improve its optical properties. The conventional measure of the optical quality of lithium niobate crystals is taken to be the residual light transmission in crossed polaroids when light propagates along the polar axis.[1] In general, the presence of a residual light flux and its variation with temperature are a negative factor in the operation and fabrication of lithium-niobate optoelectronic elements. We reported earlier[2] that changes in the composition of lithium niobate, especially from congruent to stoichiometric, lead to changes in the activation energy of the process responsible for the variation of the residual light flux with temperature. In stoichiometric crystals the main process responsible for the behavior dynamics of the optical inhomogeneity is the conductivity caused by the presence of oxygen vacancies.[3]

In view of this, it is meaningful to investigate the influence of reduction and subsequent recovery on the temperature dependence of the residual light flux in lithium niobate crystals using the technique described in Ref. 4, since this treatment should alter the concentration of oxygen vacancies in the bulk of the crystals.

The ideas put forward by Blistanov *et al.*[1] and developed by us in Ref. 2 form the theoretical basis of this work.

The samples were congruent crystals and crystals which had undergone vapor transport equilibration (VTE) treatment to change their composition from congruent to stoichiometric.[4] The samples were reduced in vacuum at 600 °C for 40 min and turned a faint gray color. Recovery took place at the same temperature for 2 h until the color disappeared.

The residual light transmission as a function of temperature for nominally pure congruent $LiNbO_3$ contains peaks (Fig. 1), which is consistent with earlier results. This is a consequence of at least two processes which influence the screening of the fields of charge defects in the bulk of the crystal: screening of internal electric fields by thermally activated charge and migration of these charges in the direction of the polar axis as a result of the incipient pyrofield. In this case, the top of the peak can be treated as the equilibrium point between these processes. The increase in the residual light transmission involves descreening of defects when charges are attracted by the pyrofield, while an increase in the concentration of thermally activated charge on scales required to screen both the charged defects and the influence of the pyrofield causes a reduction. The residual light transmission decreases exponentially with temperature, as follows from the proposed model, which confirms the assumptions made. The activation energy for screening of the internal electric fields by the thermally activated charge can be calculated from the descending section.

As we know, electron motion via oxygen vacancies with activation energies up to 0.5 eV plays an important role in the screening of the internal electric fields.[7,8] According to our measurements,[9] an increase in the concentration of oxygen vacancies during reduction may enhance the role of this mechanism and increase the screening of the internal electric fields.

We have established that the temperature dependence of the residual light transmission for VTE samples has two peaks (Fig. 2). In our view, this suggests that in these crystals there are two main thermal activation processes for the screening of the internal electric fields, having different activation energies. For congruent crystals the temperature dependence of the residual light transmission has a single peak but after reduction and recovery, two extrema can be identified. For both the VTE and the congruent reduced crystals the residual light transmission has almost no temperature dependence within experimental error and the values are considerably lower.

We estimated the activation energy of the processes responsible for the disappearance of the residual light transmission from the descending sections of its temperature dependence using a technique described in Ref. 2. These energies are 0.62 and 0.7 eV at heating rates of 3 deg/min for the congruent crystal and 0.51, 0.21, and 0.3 eV for the VTE sample at a heating rate of 3 deg/min. The activation energy corresponding to the descending section after the first peak on the temperature dependence of the residual light transmission for a congruent crystal after reduction and recovery is 0.91 eV.

In order to identify the carriers involved in these processes, we used the cation substitution model put forward by

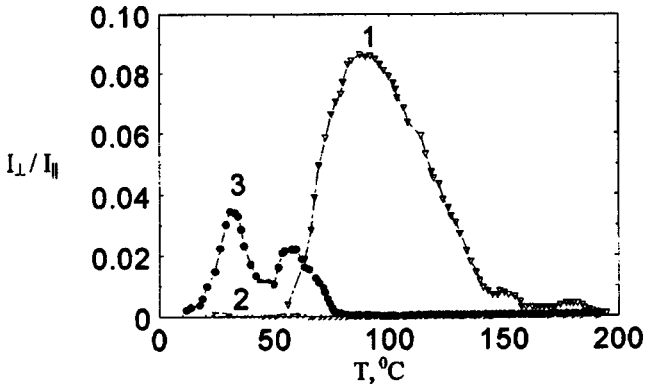

FIG. 1. Residual light transmission versus temperature for congruent $LiNbO_3$ crystals: nominally pure (1), reduced (2), and recovered (3).

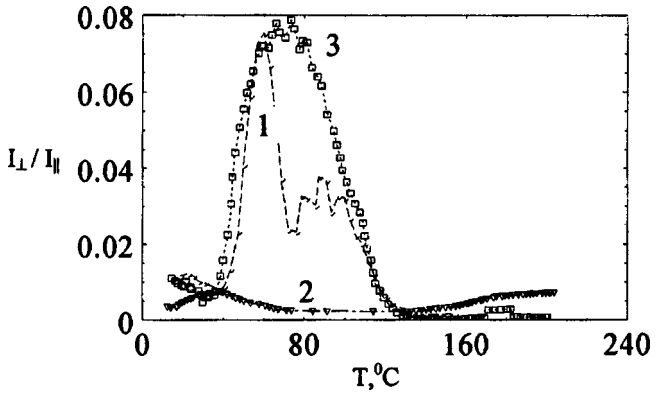

FIG. 2. Residual light transmission versus temperature for VTE-treated $LiNbO_3$ crystals: nominally pure (1), reduced (2), and recovered (3).

Nassau and Lines,[5] according to which the main type of defects for congruent lithium niobate crystals are lithium vacancies. As the crystal composition approaches stoichiometric, some oxygen vacancies may appear. Naturally, the crystal also contains other types of defects, which explains the appearance of two (rarely three) rectilinear sections on the descending section of the curves $\ln[I_\perp / I_\parallel](1/T)$. Volk *et al.*[6] discuss the participation of these defects as electron trapping centers in charge transport in $LiNbO_3$. Screening of the internal electric fields by means of electron motion via deep trapped levels associated with oxygen vacancies is most likely responsible for the appearance of the second peak on the temperature dependence of the residual light transmission.

These conclusions were confirmed in the experiments using reduced samples. Reduction leads to the appearance of a large number of oxygen vacancies, which results in almost complete screening of the internal electric fields by these oxygen vacancies. When reduced congruent samples are annealed in open air, the initial properties recover but some of the oxygen vacancies produced during reduction are retained, which gives rise to the second peak on the temperature dependence of the residual light transmission for the reduced samples. Only a single peak was identified for the recovered VTE samples.

We have established that for both congruent and VTE-treated crystals thermal treatment in vacuum causes the temperature dependence of the residual light flux to disappear almost completely in the range 20–200 °C and reduces the residual light transmission by more than an order of magnitude. This confirms that the presence of oxygen vacancies in the bulk of lithium niobate has a substantial influence on the behavior kinetics of the optical inhomogeneity of $LiNbO_3$ crystals.

Annealing reduced crystals in open air almost completely restores the initial properties of the crystals. The temperature dependence of the residual light transmission for the congruent crystals has two peaks whereas that for the VTE samples has only one.

This work was carried out under Project No. 97–02–16600 of the Russian Fund for Fundamental Research.

[1] A. A. Blistanov, E. V. Makarevskaya, V. V. Geras'kin, O. K. Komalov, and M. M. Koblova, Fiz. Tverd. Tela (Leningrad) **20**, 2575 (1978) [Sov. Phys. Solid State **20**, 1489 (1978)].
[2] B. B. Ped'ko and É. V. Lebedev, Izv. Akad. Nauk SSSR, Ser. Fiz. **61**, No. 2, (1997).
[3] Yu. S. Kuz'minov, *Electrooptic and Nonlinear Optical Lithium Niobate Crystal* [in Russian], Nauka, Moscow (1987).
[4] C. Fischer, S. Kapphan, Feng Xi-Qi, and N. Cheng, in *Proceedings of European Conference*, Lyon, 1984.
[5] K. Nassau and M. E. Lines, J. Appl. Phys. **41**, 533 (1970).
[6] T. R. Volk, S. B. Astaf'ev, and N. V. Razumovskiĭ, Fiz. Tverd. Tela (Leningrad) **37**, 1073 (1995) [Sov. Phys. Solid State **37**, 583 (1995)].
[7] F. S. Chen, Y. T. Macchia, and D. V. Fraser, Appl. Phys. Lett. **13**(7), 223 (1968).
[8] F. S. Chen, Appl. Phys. **40**, 3389 (1969).
[9] É. V. Lebedev, N. Yu. Franko, and B. B. Ped'ko, in *Abstracts of papers presented at International Scientific and Practical Conference ''Dielectric 97''*, St. Petersburg [in Russian], St. Petersburg State Technical University Press, (1997), p. 171.

Translated by R. M. Durham

Spectrum of phase noise in the Dulkyn pentagonal ring interferometer and test experiments to detect a weak periodic signal

A. R. Agachev, A. B. Balakin, G. V. Kisun'ko, S. V. Mavrin, Z. G. Murzakhanov, A. F. Skochilov, and Yu. P. Chugunov

Scientific Center of Gravitational Wave Research, Institute of the Academy of Sciences of Tatarstan, Kazan
(Submitted May 15, 1998)
Pis'ma Zh. Tekh. Fiz. **24**, 86–92 (November 26, 1998)

Results of the first long-term experiments using a pentagonal interferometer are described. These experiments were used to refine the detection of a given simulated signal against a noise background. © *1998 American Institute of Physics.* [S1063-7850(98)02911-5]

As part of work on the Dulkyn project to detect periodic gravitational radiation,[1,2] a group at the Joint Experimental Laboratory of Gravitational-Optical Research built, set up, and successfully tested a pentagonal two-loop ring laser interferometer operated in a passive mode.[3]

Since December 1997, the pentagonal interferometer has been used to carry out several series of continuous long-term experiments (up to eight days each) which allowed us to study its phase noise spectrum in the pentagonal interferometer at frequencies between 10^{-5} and 10^{-1} Hz. These experiments were also used to refine the detection of a given periodic (simulated) signal against the background of real phase noise, while the phase difference of the interfering beams was stabilized by a servosystem.[4]

This extremely low-frequency range, not normally used for interferometer research, was selected because the Dulkyn project is aimed at the detection of periodic gravitational radiation from double relativistic astrophysical objects, which emit gravitational waves in this frequency range. For this reason, a phase modulator, used to simulate the detected signal, was inserted in the signal loop of the pentagonal interferometer.

1. SPECTRAL DENSITY OF THE NOISE

The stabilizing servosystem was an analog-digital device using a computer which controlled the stabilization process according to a specially developed universal program. The main component of the servosystem was a special phase modulator[4] consisting of a combination of thin dielectric plates which could be turned through small angles about the vertical axis under computer control. The phase modulator could minimize the amplitude of the phase difference fluctuations $\Phi(t)$ in the interference pattern to better than $\Phi_0 = 10^{-2}$ rad (the ''stabilization threshold'').

From the theoretical point of view, the change in the phase difference in the interference field may be given by

$$\Phi(t) = \varphi(t) + \varphi_s \sin(\Omega_s t) + \Psi(t), \tag{1}$$

where the first term in the sum is the unreduced phase noise $\varphi(t)$ of the interferometer which can be observed when the stabilizing servosystem is disconnected. The second term is a given periodic change in phase, which simulates the useful signal of amplitude φ_s and frequency Ω_s. The third term describes the controlled phase changes introduced by the phase modulator of the servosystem for the error signal. Let us assume that $\max|\varphi(t)|$ is the upper threshold of the unreduced noise in the interferometer. The stabilizing system can fix the sum $\xi(t) = \varphi(t) + \Psi_{\rm PM}(t)$ at the level $|\xi(t)| \leqslant \Phi_0$, where the upper threshold for the reduced noise $\xi(t)$ is several orders of magnitude lower than $\max|\varphi(t)|$.

The spectral density of the fluctuations of the unreduced phase noise $S_\varphi(\nu) = F[\langle \varphi(t)\varphi(t+\tau)\rangle]$, where $\langle \varphi(t)\varphi(t+\tau)\rangle$ is the autocorrelation function and $F[\dots]$ is the Fourier transformation operator, is related to the similar function $S_\xi(\nu)$ for the reduced noise by

$$S_\xi(\nu) = \frac{S_\varphi(\nu)}{(1+K(\nu))^2},$$

where $K(\nu)$ is the gain in the feedback circuit.

Figure 1 gives the spectral densities of the amplitude of the unreduced noise $\tilde{\varphi}(\nu) = \sqrt{S_\varphi(\nu)}$ (curve *1*) and the reduced noise $\tilde{\xi}(\nu) = \sqrt{S_\xi(\nu)}$ (curve *2*) plotted against the frequency ν, calculated using the experimental data.

It can be seen that the unreduced interferometer noise has a spectrum characteristic of flicker noise and may be approximated by the function $\tilde{\varphi}(\nu) \simeq \tilde{\varphi}_0 \nu_0/\nu$ with the parameters $\nu_0 = 10^{-5}$ Hz and $\tilde{\varphi}_0 = 5\times 10^2$ rad/$\sqrt{\rm Hz}$. The reduced noise in the frequency range between 10^{-5} and 10^{-1} Hz is fairly accurately approximated by white noise: $\xi(\nu) \simeq \xi_0 = 5\times 10^{-3}$ rad/$\sqrt{\rm Hz}$. The gain $K(\nu)$ for this frequency range can be given as $K(\nu) \simeq \tilde{\varphi}_0 \nu_0/\xi_0 \nu - 1$.

2. SEPARATION OF THE SIGNAL FROM THE NOISE

Since the frequency of the gravitational waves emitted by double relativistic astrophysical objects such as PSR J1537+1155 is known with a high degree of accuracy, the very familiar cumulative adaptive comb filter can be used to separate the signal from the noise in the Dulkyn detector.[1,2]

The operating principle of the filter, which is in many respects similar to the well-known multichannel multiplexing method, is as follows. The period of the required signal $T_s = 2\pi/\Omega_s$ is divided into M time intervals of duration $\Delta t = T_s/M$. Then, during a single period T_s of the signal at

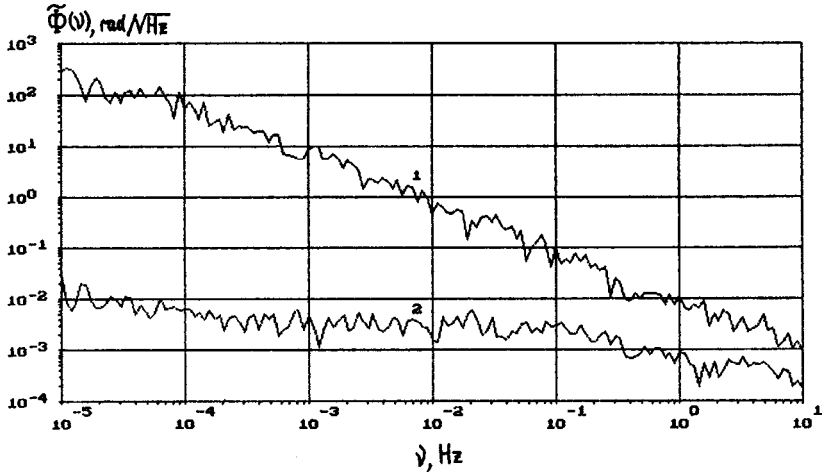

FIG. 1. Spectral density of the amplitude of the phase noise (stabilizing system: *1* — switched off, *2* — switched on.)

times $t_m = m\Delta t$ $(m = 0,1,\ldots,M)$ measurements are made of the phases $\Phi_m = \Phi(t_m)$ which are numbered and entered into specific computer memory locations. During the next signal period the procedure is repeated and the results of the measurements are added to the appropriate locations. Ultimately, after N acquisition periods we will have

$$\Phi_m = \sum_{j=1}^{N} \Phi(t_{mj}), \quad t_{mj} = \left(\frac{m}{M} + j - 1\right) T_s . \tag{2}$$

Substituting Eq. (1) into Eq. (2), we formally obtain at the filter output

$$\Phi_m = N\varphi_s \sin\left(2\pi \frac{m}{M}\right) + \sum_{j=1}^{N} \xi(t_{mj}). \tag{3}$$

The first term of the sum in Eq. (3) is the coherently acquired signal whose amplitude is N times larger than that of the initial signal φ_s. Sufficient caution must be exercised when estimating the second term of the sum.

In the absence $(\varphi_s = 0)$ of any useful signal in Eq. (1) the quantity $\xi(t)$ is a random stochastic function, since the stabilizing system ''works on'' the random intrinsic interferometer noise $\varphi(t)$ and thus the second term of the sum in Eq. (3) will increase as $\sqrt{N}$.

In the presence of a periodic signal $(\varphi_s \neq 0)$, two variants are possible: either the signal amplitude φ_s is so small that the stabilizing servosystem does not sense its presence and then $\xi(t)$ is a random quantity as before or, if the signal amplitude is fairly large, the stabilizing servosystem begins to ''work'' and a regular component appears in $\xi(t)$ which is responsible for compensating for the signal. In the first case, the second term of the sum in Eq. (3) will increase as $\sqrt{N}$, and after a sufficient number of signal periods the first term of the sum exceeds the second, i.e., the useful signal will be detected. In the second case the useful signal cannot be separated from the noise.

These experimental investigations have shown that in the Dulkyn two-loop pentagonal interferometer the stabilizing system does not destroy the useful periodic signal if its amplitude is at least two orders of magnitude below the stabilization threshold Φ_0. Figure 2 shows typical results for the operation of the filter for a signal of amplitude $\varphi_s = 10^{-4}$ rad and frequency $\omega_s = 1.460 \times 0^{-2}$ Hz. In the three diagrams in Fig. 2 the points indicate the values of Φ_m $(M = 3185)$ and the solid curve characterizes the given signal. In the upper and middle diagrams the acquisition period was exactly the same as the signal period, whereas in the lower diagram it

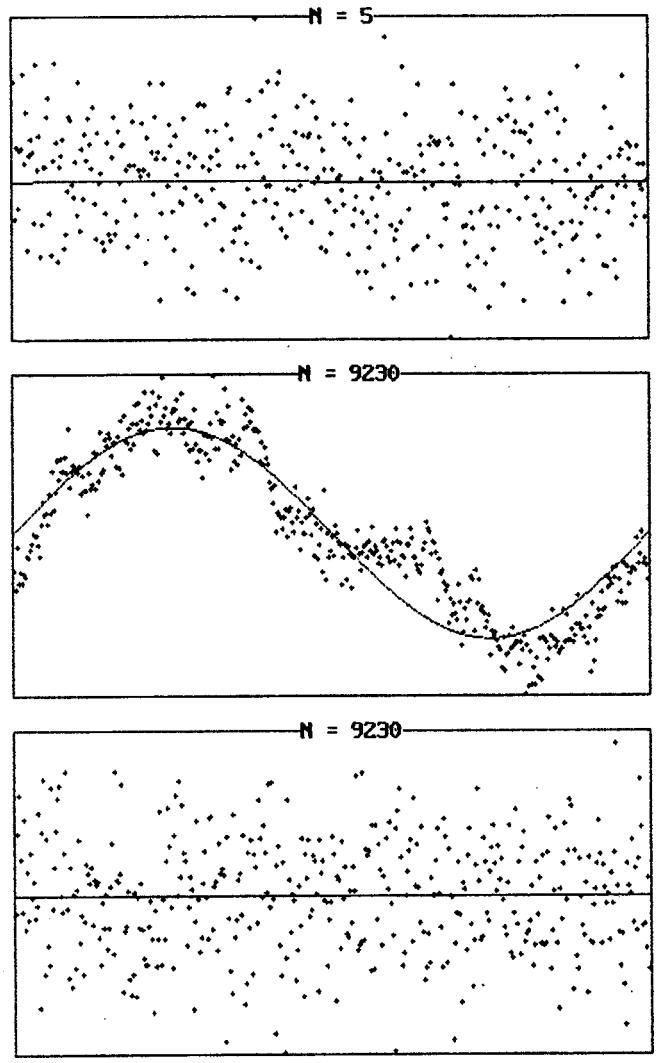

FIG. 2. Experimental results using the cumulative adaptive comb filter.

corresponded to the frequency $\Omega = 1.461 \times 10^{-2}$ Hz. It can be seen from Fig. 2 that when the number of signal periods was $N = 9230$ and the frequency corresponded to that of the detected signal, it could be reliably separated (see middle digram) from noise whose maximum amplitude is two orders of magnitude greater than the signal amplitude (see upper diagram). When the signal amplitude φ_s approaches the stabilization threshold Φ_0, the useful signal was destroyed and the result of its acquisition was similar to the lower diagram in Fig. 2.

3. CONCLUSIONS

1. The curve giving the spectral density of the phase noise reduced by the stabilizing servosystem of the Dulkyn pentagonal interferometer shows no anomalous increase at frequencies close to zero; the behavior of the curve at frequencies below 1 Hz is typical of white noise and in this sense differs fundamentally from the unboundedly increasing spectral curves typical of long-base laser-interferometer gravitational wave detectors.

2. The servosystem for stabilizing the phase difference of the interfering beams in the Dulkyn pentagonal interferometer does not destroy the periodic useful signal until the stabilization threshold is two (or more) orders of magnitude higher than the amplitude of the useful signal. In this case, the cumulative adaptive comb filter filter can reliably separate the periodic useful signal from the noise.

[1] A. B. Balakin, G. V. Kisun'ko, Z. G. Murzakhanov, and A. F. Skochilov, Dokl. Akad. Nauk **346**(1), 39 (1996) [Sov. Phys. Dokl. **41**, 19 (1996)].
[2] A. V. Balakin, Z. G. Murzakhanov, and A. F. Skochilov, Gravitation Cosmology **3**, No. 1 (9), 71 (1997).
[3] A. R. Agachev, A. B. Balakin, G. N. Buĭnov *et al.*, Zh. Tekh. Fiz. **68**(5), 121 (1998) [Tech. Phys. **43**, 591 (1998)].
[4] I. B. Konstantinov, Z. G. Murzakhanov, and A. F. Skochilov, Izv. Vyssh. Uchebn. Zaved. Fiz. No. 2, 22 (1998).

Translated by R. M. Durham